Understanding Size Effects in Small Scale Deformation: A Statistical Perspective

A Dissertation Presented for
the Doctor of Philosophy
Degree
The University of Tennessee, Knoxville

Sudharshan Phani Pardhasaradhi
December 2012

DEDICATION

To the lotus feet of my spiritual master H.H. Ranga Ramanuja Maha Desikan.

ACKNOWLEDGEMENTS

At the outset, I would like to thank Dr. George Pharr for giving me an opportunity to work on my PhD under his guidance. But for him, I would not have pursued my PhD in USA. Apart from being a great teacher and advisor, he has been of immense help on several fronts throughout my PhD. The person who has been instrumental in making my stay in Knoxville, a pleasurable and rewarding experience is Kurt Johanns. I cannot describe the amount of academic and personal help I received from Kurt and thank him for all the help. On a similar note, I would like to specially thank Dr. Erik Herbert not only for the technical help but also for the valuable advice on several occasions. I would also like to thank my other committee members (Dr. Easo George, Dr Dayakar Penumadu and Dr. Warren Oliver) for their time and inputs. I would also like to thank all the members of Dr. Pharr's group for creating a great work environment. Finally, I would like to thank the staff and faculty of the department of Materials Science and Engineering for their help over the years. My sincere regards to all my friends who have made my stay in Knoxville memorable.

This work was supported by the US Department of Energy, Office of Basic Energy Sciences, Materials Sciences and Engineering Division.

ABSTRACT

Recent experimental observations of micro-compression / tension tests indicate that as the size of test specimen decreases the yield strength increases. This raises a fundamental question: Why is smaller stronger? Is there a fundamental relationship between the size of a specimen and its intrinsic strength? This simple question pushes the limit of the current understanding of the physical mechanisms underlying material deformation, especially at small scales. In order to explain the experimental observations of the strength of small specimens containing a limited number of dislocations, a simple statistical model is developed. Two different types of randomness are introduced, viz., randomness in the spatial location of dislocations and randomness in the stress needed to activate them. For convenience, the randomness in the activation stress is modeled by assigning a random Schmid factor to the dislocations. In contrast to the previous stochastic models, the current model not only predicts the yield strength in the presence of dislocations but also in their absence. Furthermore, the model has the capability to predict the scatter in the yield strength in addition to the mean. Monte Carlo simulations are also performed for comparison. Interestingly, the model adds credence to the notion that "smaller is stronger" from a purely statistical point of view. The model is found to quantitatively explain the yield strength and scatter in micro-compression / tension tests of Mo-alloy fibers using dislocation densities and arrangements measured by TEM. Furthermore, the model is extended to spherical indentation pop-in which is an analogous size dependent problem in small scale mechanics. In this case, the model predicts the load and maximum shear stress at pop-in as a function of indenter radius and is found to closely match the experimental results on single crystal molybdenum using a dislocation density estimated by micro-focus x-ray techniques. In summary, the current work provides possible explanations for the strength and scatter in strength of small specimens from a purely statistical perspective.

TABLE OF CONTENTS

LIST OF FIGURES

INTRODUCTION

This dissertation is a combination of three journal articles: 1) "Scanning transmission electron microscope observations of defects in as-grown and pre-strained Mo-alloy fibers"; 2) "A simple stochastic model for yielding in specimens with limited number of dislocations"; and 3) "A stochastic model for the size dependence of spherical indentation pop-in". The overall focus of these articles is to explain recent experimental observations of strength in micro-pillar compression / tension tests and indentation pop-in tests using a simple statistical model in conjunction with microstructural studies. The first article was published in *Acta Materialia* in 2011, while the second will be submitted to the same journal. The third article will be submitted to the *Journal of Materials Research*. Following the guidelines set forth for multi-part dissertation by the Graduate School of the University of Tennessee, each article is presented as an individual chapter in the dissertation. The figures for each article are listed in an appendix at the end of the corresponding chapter.

The concept of "Smaller is stronger" has attracted the attention of numerous investigators in the recent past largely due to the miniaturization of several engineering components and the associated need to understand mechanical behavior at small length scales. The size dependent behavior is observed in several different forms in the area of mechanical behavior of materials, viz., the indentation size effect, wherein the hardness is found to vary with indentation depth; film thickness effects, wherein the properties of thin films are found to be dependent on film thickness, size effects on yield strength, wherein the yield / flow strength of materials is found to vary with specimen size, etc.. These size effects are observed at length scales where the specimen dimensions are comparable to the defect spacing, which is usually in the micrometer and sub-micrometer regimes. Recent advances in characterization techniques have provided unique opportunities to probe the mechanical behavior at these small length scales. One such example where the scientific community has benefitted from advanced characterization facilities is the micro-pillar compression testing (Uchic *et al.*, 2009). The ability to prepare specimens with controlled geometry at the micrometer and the sub-micrometer scale via focused ion beam (FIB) milling and the subsequent compression testing using a nanoindenter has provided the opportunity to study the yield / flow strength of materials as a function of specimen size at small length scales.

There has been much interest in studying small scale plasticity by micro-pillar compression testing. The pioneering work on micro-pillar compression testing by Uchic et al. (Uchic *et al.*, 2009) sparked several others groups (Dimiduk *et al.*, 2005; Frick *et al.*, 2008; Greer and Nix, 2008; Greer *et al.*, 2005; Kiener *et al.*, 2006; Ng and Ngan, 2008b; Richter *et al.*, 2009; Volkert and Lilleodden, 2006) to study the effect of specimen size on yield / flow strength. Most of the initial work was on face centered cubic (fcc) pillars prepared by FIB milling. A general trend observed in all these studies is the power law dependence of strength with specimen size, wherein the strength is found to increase with decreasing specimen size. However, the observations could be potentially tainted due to several experimental difficulties in pillar testing and sample preparation (Uchic *et al.*, 2009).

One of the major concerns in sample preparation is the damage induced by FIB milling. This concern was addressed by a novel sample preparation technique (Bei *et al.*, 2007), wherein sub-micrometer single crystal molybdenum alloy pillar-like structures were prepared by directional solidification of a eutectic alloy of NiAlMo. Unlike FIB milled pillars, the directionally solidified pillars exhibited high yield strengths (~ 9.2 GPa) close to the theoretical strength (~shear modulus / 26), independent of the sample size. These pillars were pre-strained in the matrix to different levels of strain (4-11%) to induce different dislocation densities prior to compression testing (Bei *et al.*, 2008). In contrast to the as-grown pillars, the highly pre-strained (11%) pillars showed low strengths close to the bulk strength (~ 1 GPa) independent of specimen size. However, the 500 nm pillars pre-strained to 4% showed significant scatter in yield strength. It was hypothesized (Bei *et al.*, 2008) that the as-grown pillars are defect free, and hence yielding occurs by nucleation of dislocations which requires higher stresses, while the highly pre-strained (11%) pillars had a high dislocation density and yielding occurs by activation of the pre-existing dislocations at lower stresses. The scatter in the yield strength for the 4% pre-strained pillars was attributed to dislocation spacing being of the order of the pillar size. However, Bei et al. (Bei *et al.*, 2008) did not have microstructural evidence to validate this hypothesis.

Recently, Johanns et al. (Johanns *et al.*, 2012) performed *in-situ* tensile tests on the same Mo-alloy fibers (300-600 nm) that were tested in compression by Bei et al. (Bei *et al.*, 2008). While the yield strengths for the pre-strained fibers matched the results of compression testing (Bei *et al.*, 2008), a significant discrepancy was observed in the case of the as-grown fibers. Unlike the compression tests, where the pillars yielded without any scatter, the yield strength in tension showed a large scatter with strengths ranging from 10 GPa to 1 GPa. Such a scatter in yield strength was also observed in the classical tensile tests on metallic whiskers by Brenner (Brenner, 1956, 1957). The scatter was attributed to the complex statistical distribution of defects in the whiskers. However, the inter-relationship between strength, scatter and specimen size has not be thoroughly studied by a statistical approach.

Interestingly, Shim et al. (Shim *et al.*, 2008) observed analogous stochastic behavior in spherical indentation pop-in where the relevant length scale is the indenter radius akin to the pillar length in micro-pillar compression. They (Shim *et al.*, 2008) reported that pop-in during nanoindentation is indicative of the onset of dislocation plasticity and thereby is an indirect measure of yield strength. They observed that the maximum shear stress at pop-in (calculated based on Hertzian elastic contact) decreases with increasing indenter tip radius. More recently, Morris et al. (Morris *et al.*, 2011) reported similar observations for a wide range of tip radii on single crystal Mo. They observed that the scatter in shear stress at pop-in is high at intermediate radii while the distribution is less scattered for small and large radii. Also, similar to the results reported by Shim et al. (Shim *et al.*, 2008) on single crystal Ni, the maximum shear stress at pop-in decreases with increasing indenter radii. These observations are analogous to the yield strength of Mo-alloy fibers during tension / compression where the length scale of interest is the pillar length instead of the indenter radius.

The above experimental observations point towards the importance of stochastic processes in small scale deformation. There have been a few attempts (El-Awady *et al.*, 2009; Ng and Ngan, 2008a; Ngan *et al.*, 2006; Parthasarathy *et al.*, 2007) to model the stochastics of small scale deformation. Ngan et al. (Ngan *et al.*, 2006) simulated the micro-pillar compression test using molecular dynamics (MD) by assigning a "Weibull" like model for the atomic displacements. They assumed that yielding occurs by homogeneous nucleation of dislocations and disregarded the role of any pre-existing dislocations. Their model predictions match the results reported by Uchic et al. (Uchic *et al.*, 2009) for certain values of the model inputs but lack any justification for the choice. Parthasarathy et al. (Parthasarathy *et al.*, 2007) proposed a stochastic model for flow strength based on random single arm dislocation source lengths on a single slip system that is oriented at 45^0 to the loading direction. They argued that the single arm sources have random lengths between zero and the radius of the pillar, and that yielding occurs by the dislocation that has the longest source length. This results in smaller pillars having smaller source lengths, producing higher yield strengths, since strength is inversely proportional to the length of the dislocation. The model was found to match the experimental results on gold micro-pillars (Greer *et al.*, 2005; Ng and Ngan, 2008b). However, the model does not consider the case of dislocation free pillars and yielding due to nucleation of dislocations. Ng and Ngan (Ng and Ngan, 2008a) extended the model of Parthasarathy et al (Parthasarathy *et al.*, 2007) by considering multiple slip systems. Their model predictions match experimental results on micro-pillar compression of aluminum (Ng and Ngan, 2008b). Recently, El-Awady et al. (El-Awady *et al.*, 2009) performed 3D dislocation dynamics (DD) simulations by assuming a Weibull distribution for the length of single armed dislocations on different slip planes and Frank-Read sources. The simulations are compared to the experimental results (Dimiduk *et al.*, 2005; Frick *et al.*, 2008) for various hypothetical probability distribution functions for the source lengths.

In summary, from the experimental observations it is apparent that the yield / flow strength (or shear stress at pop-in) and scatter in strength scales with size. Most of the models consider yielding either due to nucleation of dislocations or due to activation of pre-existing ones but not both. Also, most models assume a Weibull distribution to introduce randomness and do not have direct observations of dislocation structures by TEM. Also, the models do not address the issue of scatter in the yield strength. Hence, the current work focuses on developing a stochastic model to predict the average and scatter in yield strength in the presence and absence of dislocations by assuming random spatial location and orientation of dislocations using the defect densities estimated by microscopy (TEM) or micro-focus x-ray techniques.

The first article presents TEM observations of defects in as-grown and pre-strained Mo-alloy fibers tested in tension and compression. Dislocation densities in the as-grown and pre-strained states are estimated to qualitatively reconcile the experimental results on micro-pillar compression (Bei *et al.*, 2008). The second article presents a simple stochastic model to reconcile the apparent discrepancy in yield strength between micro-pillar compression (Bei *et al.*, 2008) and tension (Johanns *et al.*, 2012) of Mo-alloy fibers. The proposed model predicts yield strength in the presence and absence of dislocations in small specimens subject to uniaxial tension or compression. The model assumes two different types of randomness, viz., randomness in the spatial location of dislocations and randomness in the stress needed to activate them. The model has the capability to predict the scatter in the yield strength in addition to the mean. Monte Carlo simulations are also performed for comparison. The model predictions are compared to the experimental results using the dislocation densities reported in the first article. The third article extends the modeling framework presented in the second article to spherical indentation pop-in wherein the stress fields are very complex. The model predictions of maximum shear stress at first pop-in for different indenter radii are compared to experimental results on single crystal Mo using the dislocation densities estimated by micro-focus x-ray technique.

References

Bei, H., Shim, S., George, E. P., Miller, M. K., Herbert, E. G., & Pharr, G. M. 2007. Compressive strengths of molybdenum alloy micro-pillars prepared using a new technique. ***Scripta Mater***, 57(5): 397-400.

Bei, H., Shim, S., Pharr, G. M., & George, E. P. 2008. Effects of pre-strain on the compressive stress-strain response of Mo-alloy single-crystal micropillars. ***Acta Mater***, 56(17): 4762-4770.

Brenner, S. S. 1956. Tensile Strength of Whiskers. ***J Appl Phys***, 27(12): 1484-1491.

Brenner, S. S. 1957. Plastic Deformation of Copper and Silver Whiskers. ***J Appl Phys***, 28(9): 1023-1026.

Dimiduk, D. M., Uchic, M. D., & Parthasarathy, T. A. 2005. Size-affected single-slip behavior of pure nickel microcrystals. ***Acta Mater***, 53(15): 4065-4077.

El-Awady, J. A., Wen, M., & Ghoniem, N. M. 2009. The role of the weakest-link mechanism in controlling the plasticity of micropillars. ***J Mech Phys Solids***, 57(1): 32-50.

Frick, C. P., Clark, B. G., Orso, S., Schneider, A. S., & Arzt, E. 2008. Size effect on strength and strain hardening of small-scale 111 nickel compression pillars. ***Mater Sci Eng A***, 489(1-2): 319-329.

Greer, J. R., & Nix, W. D. 2008. Size dependence in mechanical properties of gold at the micron scale in the absence of strain gradients. ***Appl Phys A***, 90(1): 203-203.

Greer, J. R., Oliver, W. C., & Nix, W. D. 2005. Size dependence of mechanical properties of gold at the micron scale in the absence of strain gradients. ***Acta Mater***, 53(6): 1821-1830.

Johanns, K. E., Sedlmayr, A., Phani, P. S., Monig, R., Kraft, O., George, E. P., & Pharr, G. M. 2012. In-situ tensile testing of single-crystal molybdenum-alloy fibers with various dislocation densities in a scanning electron microscope. ***J Mater Res***, 27(3): 508-520.

Kiener, D., Motz, C., Schoberl, T., Jenko, M., & Dehm, G. 2006. Determination of mechanical properties of copper at the micron scale. ***Adv. Eng. Mater.***, 8(11): 1119-1125.

Morris, J. R., Bei, H., Pharr, G. M., & George, E. P. 2011. Size Effects and Stochastic Behavior of Nanoindentation Pop In. ***Phys Rev Lett***, 106(16).

Ng, K. S., & Ngan, A. H. W. 2008a. Breakdown of Schmid's law in micropillars. ***Scripta Mater***, 59(7): 796-799.

Ng, K. S., & Ngan, A. H. W. 2008b. Stochastic nature of plasticity of aluminum micro-pillars. ***Acta Mater***, 56(8): 1712-1720.

Ngan, A. H. W., Zuo, L., & Wo, P. C. 2006. Size dependence and stochastic nature of yield strength of micron-sized crystals: A case study on Ni3Al. ***Proc R Soc London A***, 462(2070): 1661-1681.

Parthasarathy, T. A., Rao, S. I., Dimiduk, D. M., Uchic, M. D., & Trinkle, D. R. 2007. Contribution to size effect of yield strength from the stochastics of dislocation source lengths in finite samples. ***Scripta Mater***, 56(4): 313-316.

Richter, G., Hillerich, K., Gianola, D. S., Monig, R., Kraft, O., & Volkert, C. A. 2009. Ultrahigh Strength Single Crystalline Nanowhiskers Grown by Physical Vapor Deposition. ***Nano Lett***, 9(8): 3048-3052.

Shim, S., Bei, H., George, E. P., & Pharr, G. M. 2008. A different type of indentation size effect. ***Scripta Mater***, 59(10): 1095-1098.

Uchic, M. D., Shade, P. A., & Dimiduk, D. M. 2009. Plasticity of Micrometer-Scale Single Crystals in Compression. ***Annu Rev Mater Res***, 39: 361-386.

Volkert, C. A., & Lilleodden, E. T. 2006. Size effects in the deformation of sub-micron Au columns. ***Philos. Mag.***, 86(33-35): 5567-5579.

CHAPTER I

Scanning transmission electron microscope observations of defects in as-grown and pre-strained Mo-alloy fibers

A version of this chapter was originally published by P. Sudharshan Phani, K.E. Johanns, G. Duscher, A. Gali, E.P. George and G.M. Pharr:

P. Sudharshan Phani, K.E. Johanns, G. Duscher, A. Gali, E.P. George, G.M. Pharr. “Scanning transmission electron microscope observations of defects in as-grown and pre-strained Mo-alloy fibers.” *Acta. Mater.* 59 (2011): 2172-2179.

Authors:

P. Sudharshan Phani [1], K. E. Johanns [1], G. Duscher [1,2], A. Gali [1,2], E. P. George [1,2], and G. M. Pharr [1,2]

[1] *Dept. of Materials Science and Engineering, University of Tennessee, Knoxville, TN 37996*

[2] *Materials Science and Technology Division, Oak Ridge National Laboratory, Oak Ridge, TN 37831*

P. Sudharshan Phani’s involvement in the article: Prepared samples and carried out TEM imaging, analyzed TEM data and correlated TEM data to prior experimental results, wrote and revised the article.

Co-researchers’ contributions are listed as follows:

K.E. Johanns performed sample preparation and TEM imaging with Phani and assisted in analyzing the microscopy data.

G. Duscher trained and assisted Phani and Johanns in TEM imaging.

A. Gali carried out arc-melting and single crystal growth.

E.P. George provided technical support in crystal growth and helped to correlate the microscopy data to experimental results

G.M. Pharr conceived the overall study and worked with Phani and Johanns to correlate the microscopy data to experimental results, helped prepare and revise the article.

Abstract

Compression testing of micro-pillars has recently been of great interest to the small-scale mechanics community. Previous compression tests on single crystal Mo-alloy micro-pillars produced by directional solidification of eutectic alloys showed that as-grown pillars yield at strengths close to the theoretical strength while pre-strained pillars yield at considerably lower stresses. In addition, the flow behavior changes from stochastic to deterministic with increasing pre-strain. In order to gain a microstructural insight into this behavior, an aberration corrected scanning transmission electron microscope was used to study the defect structures in as-grown and pre-strained single crystal Mo-alloy fibers. The as-grown fibers were found to be defect free over large lengths while the highly pre-strained (16%) fibers had high defect densities that were uniform throughout. Interestingly, the fibers with intermediate pre-strain (4%) exhibited an inhomogeneous defect distribution. The observed defect structures and their distributions are correlated with the previously reported stress–strain behavior. Some of the previous mechanistic interpretations of compression tests are examined in the light of new microstructural observations.

1. Introduction

Characterizing and understanding the mechanical response of a material to external stimuli has become increasingly important as engineering structures become smaller. Plastic deformation at the nano-scale may be the least understood mechanical phenomenon, but is certainly important as it places a limit on the maximum operating stress of small-scale components and structures. However, property measurement at such small scales can often be difficult, time consuming, and involve complex testing geometries (e.g. nano-indentation). In that regard, there has been great interest in micro-pillar compression testing to study small-scale plasticity in engineering materials, where a uniform stress field lends itself to more straightforward data interpretation and avoids complications due to strain gradients (Bei *et al.*, 2007a; Bei *et al.*, 2008; Uchic and Dimiduk, 2005; Uchic *et al.*, 2009).

From analogies to bulk material behavior, it is clear that the mechanical response of metallic materials during micro-pillar compression will be a strong function of the intrinsic defects that control deformation. However, at these scales the effect of defect microstructure will not be averaged over large volumes as in conventional mechanical tests. The result is deformation that can be dominated by discrete events involving a limited number of defects. Transmission electron microscopy (TEM) and other small-scale characterization techniques have proven invaluable for correlating microstructures to mechanical testing data. There are a number of investigations of metallic micro-pillar microstructures in the literature (Brenner, 1956; Frick *et al.*, 2008; Greer and Nix, 2006; Hemker and Nix, 2008; Kiener *et al.*, 2008; Kiener *et al.*, 2009; Kim *et al.*, 2010; Lee *et al.*, 2009; Maass *et al.*, 2008; Ng and Ngan, 2008; Norfleet *et al.*, 2008; Shan *et al.*, 2008). As expected, dislocation nucleation, dislocation motion, dislocation interaction (with other dislocations and surfaces) in combination with crystal orientation and boundary conditions all play important roles in material deformation.

One expects a defect-free single-crystal material subjected to a uniform compressive stress to reach the theoretical shear strength. Indeed, Bei et al. (Bei *et al.*, 2007a; Bei *et* *al.*, 2008) have measured compressive yield strengths in a careful set of experiments on single-crystal micro-pillars of a Mo-alloy and shown that as-grown pillars exhibited theoretical strengths. In contrast, when the NiAl-Mo composite was first pre-strained, which presumably introduces dislocations, before the Mo-alloy pillars were exposed and compressed, it resulted in dramatically lower strengths. In addition, there appeared to be a transition from stochastic to deterministic behavior with increasing pre-strain for a given pillar size. Lee et al. (Lee *et al.*, 2009) have observed similar reductions in strength with pre-strain in Au micro-pillars fabricated by focused ion beam (FIB) milling, although theoretical strengths were not reached in as-grown samples.

Bei et al. (Bei *et al.*, 2008) proposed three mechanistic hypotheses to explain the observed behavior in the absence of microstructural evidence or knowledge of dislocation densities:

1. As-grown pillars are virtually pristine and therefore nucleation of dislocations at the theoretical strength is required for plastic deformation.
2. The dislocation density induced by pre-straining above a certain strain is such that plasticity is governed by the collective motion and interaction of dislocations and not dislocation nucleation, thereby resulting in deterministic behavior.
3. In pillars with low pre-strain, the dislocation spacing approaches the pillar size and this results in stochastic behavior because the number of defects is very small.

The above hypotheses assume that initial defect structures play a critical role in the response of a material in the micro-pillar compression test. In order to evaluate their validity, this paper reports TEM observations of dislocation structures in as-grown and pre-strained single crystal Mo-alloy fibers extracted from a directionally solidified NiAl-Mo composite - similar to the material used by Bei et al. (Bei *et al.*, 2008). The focus will be on microstructural defects with specific emphasis on dislocations. In this regard, the current work specifically focuses on imaging large areas of as-grown and pre-strained fibers to quantify the dislocation densities (rather than individual dislocation properties such as, Burgers vectors or slip plane analyses) for correlation to the prior work on micro-pillar compression tests. Conventional TEM sample preparation with FIB milling was not used in order to avoid possible microstructural changes due to ion damage (Bei *et al.*, 2007b; El-Awady *et al.*, 2009; Kiener *et al.*, 2007; Shim *et al.*, 2009). A recent paper by Lowry et al. (Lowry *et al.*, 2010), has demonstrated the possibility of achieving strengths close to theoretical strengths by annealing FIB-milled molybdenum nanopillars inside a TEM suggesting that this may be a way to overcome FIB damage in some materials.

2. Materials and methods

2.1 Fiber preparation

Arc-melted and subsequently directionally solidified Ni-45.5Al-9Mo (at%) eutectic composites were grown in an optical floating zone furnace at a growth rate of 80 mm/h in order to achieve fiber sizes on the order of 300-500 nm. Further details of the experimental technique and composite microstructure can be found elsewhere (Bei and George, 2005). It is well known (Bei and George, 2005) that the fibers are not well-aligned at the outer surface of the composite. Hence, 3 mm diameter cylindrical specimens from the center of the composite were cut parallel to the growth direction using electric discharge machining (EDM). Both faces of the section were mechanically polished through 4000 grit silicon carbide grinding paper to remove the EDM damage layer. Samples were then pre-strained in compression to approximately 4 and 16% engineering strain (i.e. the overall change in length). The starting aspect ratio of each sample was approximately 1:1. After pre-straining, samples were sectioned in half, perpendicular to the fibers, to extract fibers from regions that avoided dead zones typically produced during compression.

Drops of a 10HCl-10H_2O_2-80H_2O (vol %) solution were placed on one surface of the sectioned and polished composite sample to selectively etch away the NiAl matrix (Frankel *et al.*, 2009). The etching time was chosen to produce fiber lengths ranging from 20-40 μm. Residual etchant was carefully wicked away with a cloth. The sample was then sonicated in a methanol solution to collect fibers that broke away from the etched surface. The above process was repeated a number of times until the solution contained enough fibers to deposit a reasonable number on a TEM grid. A plastic pipette was used to drop the methanol solution containing fibers onto a 300-mesh holey-carbon copper TEM grid [Ted Pella, Redding, CA] for TEM examination.

2.2 Scanning TEM (STEM)

A VG Microscopes' HB603U dedicated STEM with a Nion aberration corrector operating at 300 kV was used to examine the as-grown and pre-strained Mo-alloy fibers. The microscope was operated at a convergence angle of 27 mrad. The outer angle of the bright field detector and the inner angle of the high angle annular dark field detector were 30 mrad and 70 mrad respectively. Initially, the crystal structure and growth direction were examined by atomic resolution imaging. Convergent beam electron diffraction (CBED) patterns were collected in low order zone axes and crystallinity was confirmed for all the fibers. Fibers were tilted over a range of angles to ensure that all dislocations were visible. Thinning of the fibers was not required as the STEM mode in combination with a high operating voltage allowed imaging of relatively thicker samples than those examined by conventional TEM. Furthermore, the STEM mode offers better resolution of the defects. However, given the higher convergence angle in the dedicated STEM used for this study, it was not possible to achieve two-beam condition (Norfleet *et al.*, 2008) in order to determine the slip system or Burgers vector of the dislocations.

2.3 Dislocation density measurement

The apparent dislocation density, ρ, was estimated in a manner that accounts for the fact that dislocations in the sampled volume in the TEM are projected onto a 2D image using the relation:

$$\rho = \frac{1}{t}\left[\frac{\sum n_1}{\sum L_1} + \frac{\sum n_2}{\sum L_2}\right]$$

where, t is the sample thickness (assumed to be equal to the width of the square cross section fibers in the present study) and n is the number of intersecting dislocations on a grid of lines with length L (Rohatgi and Vecchio, 2002). The subscripts 1 and 2 refer to vertical and horizontal grid lines. Fig. 1.1 shows a representative image of a fiber with the overlaid grid used for dislocation density calculations. Grid spacings were varied and appropriately chosen such that the calculated dislocation densities were independent of grid size.

3. Results

3.1 Microstructure of as-grown fibers

The scanning electron microscope (SEM) characterization of the as-grown fibers has been elaborately presented in an earlier work (Bei and George, 2005). The specimen used for the current study was free of cellular growth structures and the fibers were well aligned having nearly square cross-sections. A high resolution Fourier filtered Z-contrast image along with the CBED pattern of a fiber in the $\langle 110 \rangle$ zone axis is shown in Fig. 1.2. The $\langle 001 \rangle$ direction corresponds to the fiber axis while the fiber faces are perpendicular to the $\langle 110 \rangle$ direction, corroborating previously reported findings (Bei and George, 2005; Bei *et al.*, 2007b). Also, based on the CBED patterns at different locations in the fiber, it was confirmed that the entire fiber is a single crystal.

Fig. 1.3 shows representative bright field STEM micrographs of different as-grown fibers. No evidence of any defects could be observed in these micrographs. It is also worth noting that the fibers were tilted to different orientations to confirm the absence of any defects. A total fiber length of 186 μm was imaged in several different fibers to provide better statistics. The fiber tips had some defects, presumably due to the sonication, and hence were not considered in the analyses. While the as-grown fibers were mostly defect-free, a few defects were occasionally observed as summarized in Fig. 1.4. The defects included dislocations (Fig. 1.4a), fiber branches (Fig. 1.4b) and a grain boundary (Fig. 1.4c). Fig. 4d shows a Fourier-filtered image showing {001} planes with an edge component of a dislocation at the grain boundary shown in Fig. 1.4c. The arrow pointing down shows an extra half plane between the planes shown with arrows pointing up. Based on CBED patterns from either side of the boundary, it was found to be a small angle tilt boundary.

In the 186 μm length of the as-grown fibers imaged, four different regions containing dislocations and one region with a grain boundary were found. Each region with dislocations was less than 0.5 μm long and typically had 2-5 dislocations. Based on these observations, we estimated that the number of defect-containing regions per micron length of fiber, for all the fibers that were imaged, was 0.03 μm^{-1}. Since the typical fiber length in the micro-pillar compression tests was around 1 μm (aspect ratio of 2.5 to 3) (Bei *et al.*, 2008), only 3 out of 100 micro compression tests on as-grown 1 μm long pillars would be affected by the defects. We also estimated the defect-free length fraction (calculated based on the defect-free length to the total length) in the as-grown fibers as 0.99, clearly indicating that the as-grown fibers are practically defect-free. Based on these observations, the as-grown fibers can be regarded as pristine, for all practical purposes, in the compression testing of specimens that are approximately 1 μm long.

3.2 Microstructure of 4 % pre-strained fibers

Fibers compressively pre-strained in the matrix to an engineering strain of 4% were imaged after etching away the matrix. Unlike the as-grown fibers, dislocations were frequently observed, but the dislocation densities and structures were not the same from fiber to fiber. However, for a given fiber, the dislocation density was generally uniform within the fiber length etched for imaging (10-20 μm). The dislocation densities could be broadly categorized into three different ranges - low (Fig. 1.5a & 1.5b), medium (Fig. 1.5c & 1.5d) and high (Fig. 1.5e & 1.5f). The total fiber length probed was 120 μm wherein the relative length fractions of low, medium and high were 0.23, 0.37 and 0.40 respectively. For the low defect density fibers shown in Fig. 1.5a & 1.5b, the overall average dislocation density was estimated to be 1.8 X 10^{12} m^{-2}, but that included some regions that were dislocation free. The medium defect density fibers shown in Fig. 1.5c & 1.5d were found to have an average dislocation density of 3.9 X 10^{12} m^{-2}, but that included fibers with density as low as 2.7 X 10^{12} m^{-2} and as high as 8.2 X 10^{12} m^{-2}. Within the high defect density fibers, a few regions had dislocation densities so high that we could not quantify them based on the line intercept method. Those that were measureable had an average density of 2.7 X 10^{13} m^{-2}. From these observations, it is clear that the 4% pre-strained fibers exhibit inhomogeneous defect structures.

3.3 Microstructure of 16 % pre-strained fibers

In sharp contrast to the 4% pre-strained fibers, the 16% pre-strained fibers exhibit uniformly high dislocation densities without any significant inhomogeneity over a total fiber length of 100 μm that was imaged. Fig. 1.6 shows four representative bright field STEM micrographs of the 16% pre-strained fibers. A higher magnification image of the fibers is shown in Fig. 1.7, wherein many small dislocation loops can be observed along with the straight dislocations. Loops of similar sizes were also observed by Oh et al. (Oh *et al.*, 2009) during in-situ micro-tensile tests on aluminium and were found to be prismatic. It is clear from these micrographs that 16% pre-strain induces a significantly higher average dislocation density compared to the 4% pre-strain. We also observed a few fibers with densities so high that they could not be quantified based on the line intercept method. The average dislocation density in the fibers that were measurable was estimated to be around 4.4 X 10^{13} m^{-2} ± 6.5 X 10^{12} m^{-2}.

4. Discussion

To correlate the current microstructural observations to the micro-pillar compression data of Bei et al. (Bei *et al.*, 2008),some of their results are now briefly discussed. Note that while the as-grown and 4% pre-strained fibers examined here are similar to those reported by Bei et al. (Bei *et al.*, 2008), microstructural data of 16% pre-strained fibers are reported in the present study in comparison to 11% reported by Bei et al. (Bei *et al.*, 2008). Fig. 1.8 shows the compressive stress-strain plots (Bei *et al.*, 2008) along with microstructure at various pre-strains. The as-grown pillars (0% pre-strain) yield with very little scatter at stresses close to the theoretical strength (see Fig. 1.8a), while the 11% pre-strained pillars also yield with little scatter, but at a much lower stress (see Fig. 1.8b). The 4% pre-strained pillars, on the other hand, show considerable scatter in strength (see Fig. 1.8c), with some of the pillars yielding at strengths as low as that of the 11% pre-strained pillars.

It is evident from the micrograph shown in Fig. 1.8a that the as-grown fibers are practically defect-free and hence exhibit yield strengths close to the theoretical strength during micro-pillar compression testing. This validates the suggestion of Bei et al. (Bei *et al.*, 2008) that the as-grown fibers behave like dislocation-free materials, and their high yield strength is that needed for dislocation nucleation. In the case of 11% pre-strained fibers, Bei et al. (Bei *et al.*, 2008) speculated that introducing a sufficiently large number of dislocations results in stable plastic deformation governed by bulk-like collective motion and interaction of dislocations without the need for nucleation. The STEM micrographs shown in Fig. 1.8b for 16% pre-strained fibers provide microstructural confirmation for this. Finally, the stochastic behavior observed at an intermediate pre-strain (4%) was speculated to occur when the dislocation spacing was of the order of specimen size (Bei *et al.*, 2008), i.e., with a limited number of dislocations, the strength would be very sensitive to the exact number and nature of the dislocations. However, from the present study (see micrographs in Fig. 1.8c), it is evident that the stochastic behavior is due to the inhomogeneous dislocation distribution observed at intermediate pre-strains, including low density and high density regions. The wide range of dislocation densities observed in the case of 4% pre-strained fibers is more likely the source of the scatter in the strengths. Furthermore, the very low strengths (approaching that of the highly pre-strained fibers) observed in some of the 4% pre-strained fibers are easier to explain by the inhomogeneous defect structures than by the dislocation spacing argument of Bei et al. (Bei *et al.*, 2008). Several possible explanations could be offered for the observed inhomogeneity. One is that pre-straining often resulted in cracking in the NiAl matrix. One would then expect different fiber strains to be produced locally in regions near cracks. A second possibility is that there could be significant strain localization in some fibers if their deformation is accompanied by strain softening, as is thought to be the case for the low defect fibers (Bei *et al.*, 2007a; Bei *et al.*, 2008). Both of these would result in inhomogeneous deformation, and therefore, a large spatial variation in dislocation densities.

It is instructive to compare the TEM results discussed above with earlier results of Laue micro-diffraction (Barabash *et al.*, 2010; Zimmermann *et al.*, 2010). Very sharp x-ray peaks were obtained from the as-grown fibers, indicative of perfect single crystals, but significant peak broadening and streaking was observed after the fibers were pre-strained, indicative of stored dislocations and deviatoric strains. From the measured x-ray peak widths, the dislocation density in the 11% pre-strained fibers was estimated to be in the range of 1×10^{13} to 3×10^{13} m^{-2} (Barabash *et al.*, 2010), which agrees well with the average density estimated from TEM of the 16% pre-strained fibers, 4.4×10^{13} m^{-2}. For the 4% pre-strained pillars, an average density is less meaningful since the dislocations are inhomogeneously distributed (Fig. 1.5). Nevertheless, in regions where the dislocation density was high (Fig. 1.5e & 1.5f) the density estimated from the TEM micrographs (2.7×10^{13} m^{-2}) is comparable to that estimated from x-ray measurements for the 5% pre-strained pillars (1×10^{13} to 3×10^{13} m^{-2} (Barabash *et al.*, 2010)). An intriguing result of the x-ray measurements was that there was little difference in the total dislocation densities of the 5% and 11% pre-strained pillars (Barabash *et al.*, 2010) despite the fact that their mechanical behaviors were significantly different, stochastic and deterministic, respectively (Bei *et al.*, 2008). The present TEM results suggest a possible explanation for this discrepancy. The x-ray measurements may not have had the spatial resolution needed to observe the inhomogeneity of the dislocation distribution in the 4% pre-strained pillars which we now believe is the cause of their stochastic response.

While the present microstructural observations explain the stochastic and deterministic behavior observed in micro-pillar compression testing, further investigation is needed to determine the exact cause of the inhomogeneity at intermediate pre-strains.

5. Summary

An aberration corrected STEM was used to investigate the defect structures of as-grown and pre-strained single-crystal Mo-alloy fibers. The as-grown fibers were obtained by selectively etching the NiAl matrix of a NiAl-Mo composite and depositing them on a TEM grid without the use of FIB in sample preparation. The fibers were compressively pre-strained in the matrix to different macro-strain levels to correlate the previously reported stress-strain behavior of the Mo-alloy micro-pillars with the microstructure. At one extreme, the as-grown fibers were practically defect-free and hence exhibited yield strengths close to the theoretical strength during micro-pillar compression testing. At the other extreme, the 16% pre-strained fibers showed high dislocation densities without any significant inhomogeneities, resulting in bulk-like, deterministic behavior. At an intermediate pre-strain (4%), the fibers exhibited inhomogeneous dislocation distributions resulting in stochastic behavior. The microstructural observations reported in this work help to explain the observed stress-strain behavior of Mo-alloy micro-pillars.

Acknowledgments

This work was supported by the US Department of Energy, Office of Basic Energy Sciences, Materials Science and Engineering Division (materials synthesis) and the Center for Defect Physics, an Energy Frontier Research Center funded by the US Department of Energy, Office of Science, Office of Basic Energy Sciences (materials characterization).

References

Barabash, R. I., Bei, H., Gao, Y., Ice, G. E., & George, E. P. 2010. 3D x-ray microprobe investigation of local dislocation densities and elastic strain gradients in a NiAl-Mo composite and exposed Mo micropillars as a function of prestrain. ***J Mater Res***, 25(02): 199-206.

Bei, H., & George, E. P. 2005. Microstructures and mechanical properties of a directionally solidified NiAl-Mo eutectic alloy. ***Acta Mater***, 53(1): 69-77.

Bei, H., Shim, S., George, E. P., Miller, M. K., Herbert, E. G., & Pharr, G. M. 2007a. Compressive strengths of molybdenum alloy micro-pillars prepared using a new technique. ***Scripta Mater***, 57(5): 397-400.

Bei, H., Shim, S., Miller, M. K., Pharr, G. M., & George, E. P. 2007b. Effects of focused ion beam milling on the nanomechanical behavior of a molybdenum-alloy single crystal. ***Appl Phys Lett***, 91(11): 111915.

Bei, H., Shim, S., Pharr, G. M., & George, E. P. 2008. Effects of pre-strain on the compressive stress-strain response of Mo-alloy single-crystal micropillars. ***Acta Mater***, 56(17): 4762-4770.

Brenner, S. S. 1956. Tensile Strength of Whiskers. ***J Appl Phys***, 27(12): 1484-1491.

El-Awady, J. A., Woodward, C., Dimiduk, D. M., & Ghoniem, N. M. 2009. Effects of focused ion beam induced damage on the plasticity of micropillars. ***Phys Rev B***, 80(10).

Frankel, D., Milenkovic, S., Smith, A. J., & Hassel, A. W. 2009. Nanostructuring of NiAl-Mo eutectic alloys by selective phase dissolution. ***Electrochim Acta***, 54(25): 6015-6021.

Frick, C. P., Clark, B. G., Orso, S., Schneider, A. S., & Arzt, E. 2008. Size effect on strength and strain hardening of small-scale 111 nickel compression pillars. ***Mater Sci Eng A***, 489(1-2): 319-329.

Greer, J. R., & Nix, W. D. 2006. Nanoscale gold pillars strengthened through dislocation starvation. ***Phys Rev B***, 73(24).

Hemker, K. J., & Nix, W. D. 2008. Nanoscale deformation - Seeing is believing. ***Nat Mater***, 7(2): 97-98.

Kiener, D., Grosinger, W., Dehm, G., & Pippan, R. 2008. A further step towards an understanding of size-dependent crystal plasticity: In situ tension experiments of miniaturized single-crystal copper samples. ***Acta Mater***, 56(3): 580-592.

Kiener, D., Motz, C., & Dehm, G. 2009. Micro-compression testing: A critical discussion of experimental constraints. ***Mater Sci Eng A***, 505(1-2): 79-87.

Kiener, D., Motz, C., Rester, M., Jenko, M., & Dehm, G. 2007. FIB damage of Cu and possible consequences for miniaturized mechanical tests. ***Mater Sci Eng A***, 459(1-2): 262-272.

Kim, J. Y., Jong, D. C., & Greer, J. R. 2010. Tensile and compressive behavior of tungsten, molybdenum, tantalum and niobium at the nanoscale. ***Acta Mater***, 58(7): 2355-2363.

Lee, S. W., Han, S. M., & Nix, W. D. 2009. Uniaxial compression of fcc Au nanopillars on an MgO substrate: The effects of prestraining and annealing. ***Acta Mater***, 57(15): 4404-4415.

Lowry, M. B., Kiener, D., LeBlanc, M. M., Chisholm, C., Florando, J. N., Morris, J. W., & Minor, A. M. 2010. Achieving the ideal strength in annealed molybdenum nanopillars. ***Acta Mater***, 58(15): 5160-5167.

Maass, R., Van Petegem, S., Zimmermann, J., Borca, C. N., & Van Swygenhoven, H. 2008. On the initial microstructure of metallic micropillars. ***Scripta Mater***, 59(4): 471-474.

Ng, K. S., & Ngan, A. H. W. 2008. Stochastic nature of plasticity of aluminum micro-pillars. ***Acta Mater***, 56(8): 1712-1720.

Norfleet, D. M., Dimiduk, D. M., Polasik, S. J., Uchic, M. D., & Mills, M. J. 2008. Dislocation structures and their relationship to strength in deformed nickel microcrystals. ***Acta Mater***, 56(13): 2988-3001.

Oh, S. H., Legros, M., Kiener, D., & Dehm, G. 2009. In situ observation of dislocation nucleation and escape in a submicrometre aluminium single crystal. ***Nat Mater***, 8(2): 95-100.

Rohatgi, A., & Vecchio, K. S. 2002. The variation of dislocation density as a function of the stacking fault energy in shock-deformed FCC materials. ***Mater Sci Eng A***, 328(1-2): 256-266.

Shan, Z. W., Mishra, R. K., Asif, S. A. S., Warren, O. L., & Minor, A. M. 2008. Mechanical annealing and source-limited deformation in submicrometre-diameter Ni crystals. ***Nat Mater***, 7(2): 115-119.

Shim, S., Bei, H., Miller, M. K., Pharr, G. M., & George, E. P. 2009. Effects of focused ion beam milling on the compressive behavior of directionally solidified micropillars and the nanoindentation response of an electropolished surface. ***Acta Mater***, 57(2): 503-510.

Uchic, M. D., & Dimiduk, D. A. 2005. A methodology to investigate size scale effects in crystalline plasticity using uniaxial compression testing. ***Mater. Sci. Eng., A***, 400: 268-278.

Uchic, M. D., Shade, P. A., & Dimiduk, D. M. 2009. Plasticity of Micrometer-Scale Single Crystals in Compression. ***Annu Rev Mater Res***, 39: 361-386.

Zimmermann, J., Van Petegem, S., Bei, H., Grolimund, D., George, E. P., & Van Swygenhoven, H. 2010. Effects of focused ion beam milling and pre-straining on the microstructure of directionally solidified molybdenum pillars: A Laue diffraction analysis. ***Scripta Mater***, 62(10): 746-749.

Appendix 1.1.

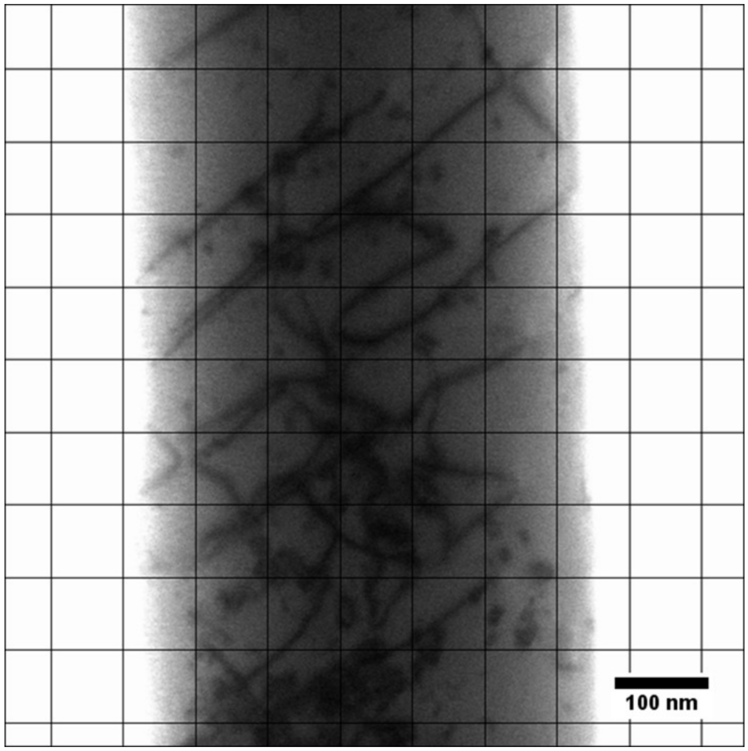

Figure 1.1. Representative STEM micrograph of a fiber with the superimposed grid for dislocation density calculations.

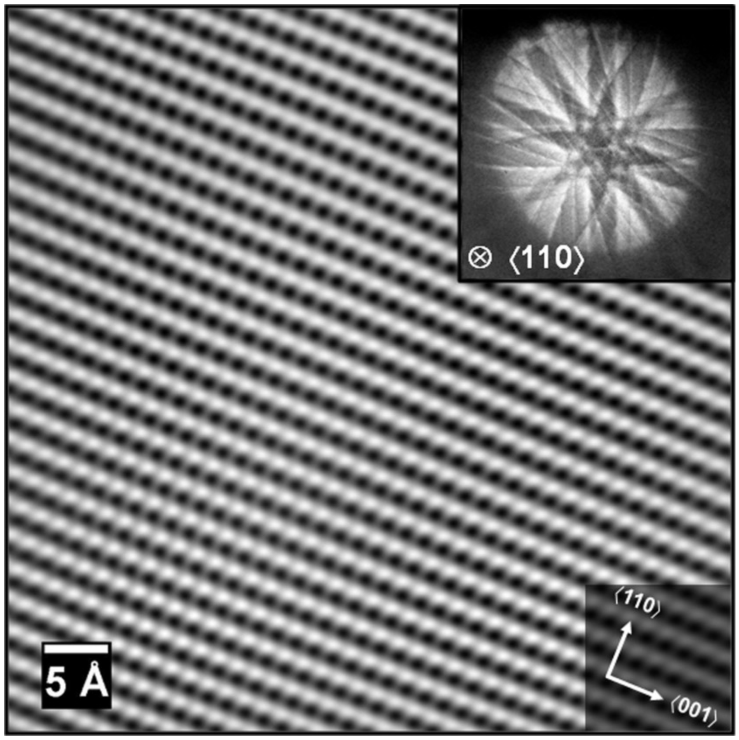

Figure 1.2. Fourier-filtered, high resolution Z-contrast image along with the CBED pattern of an as-grown fiber.

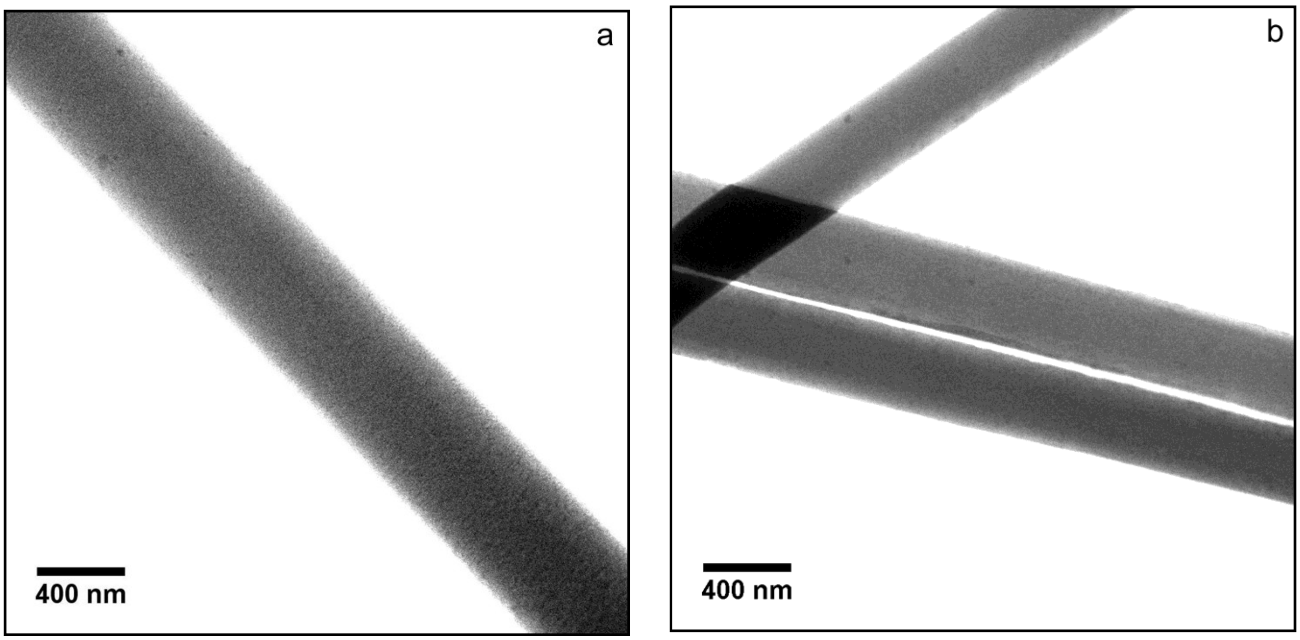

Figure 1.3. Representative bright field STEM micrographs of as-grown fibers.

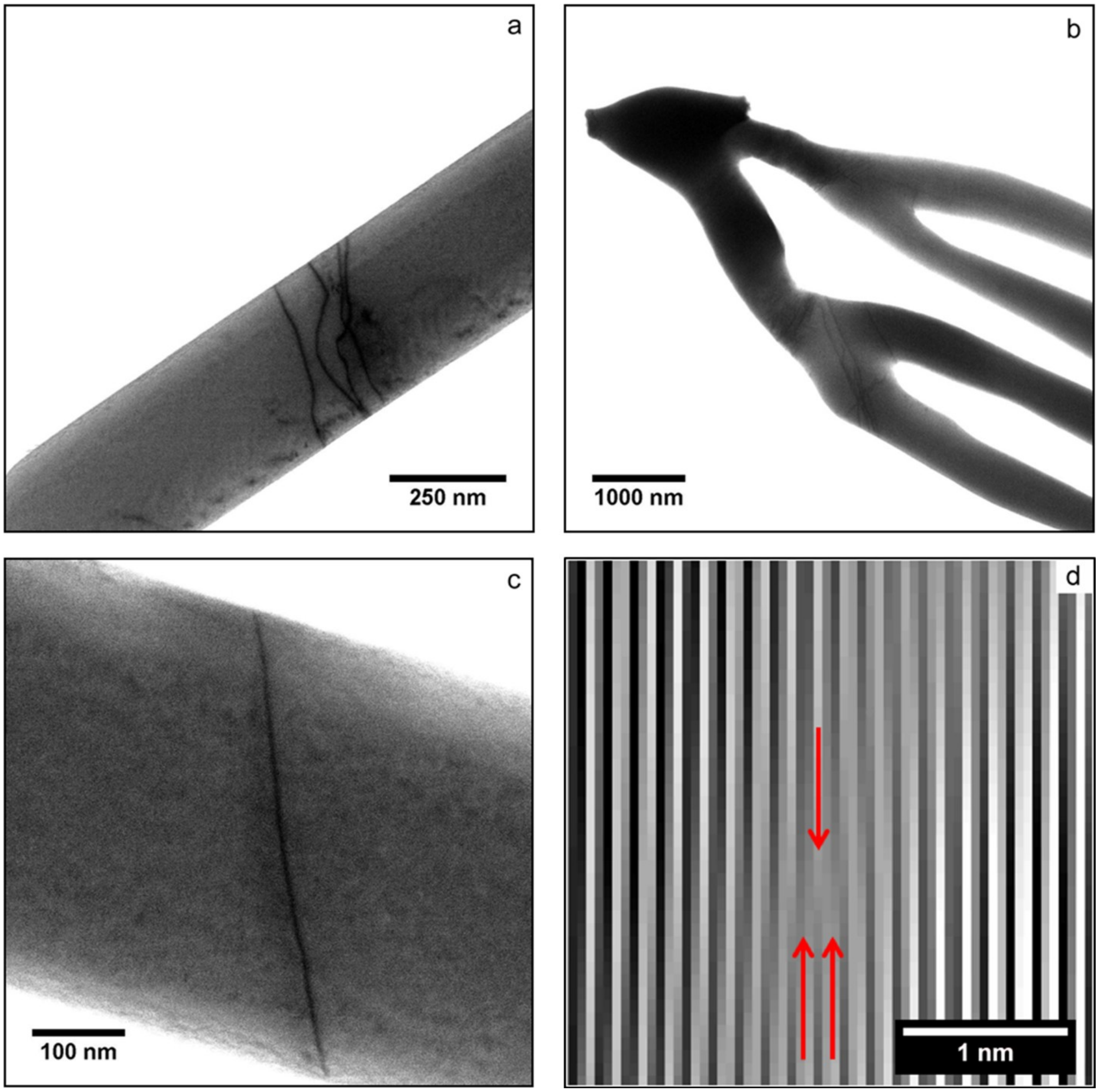

Figure 1.4. Bright field STEM micrographs of defects in as-grown fibers: (a) dislocations; (b) branches; (c) grain boundary; and (d) Fourier filtered image showing (001) planes with an edge component of a dislocation at the grain boundary shown in (c) (the arrow pointing down shows an extra half plane between the planes shown with arrows pointing up).

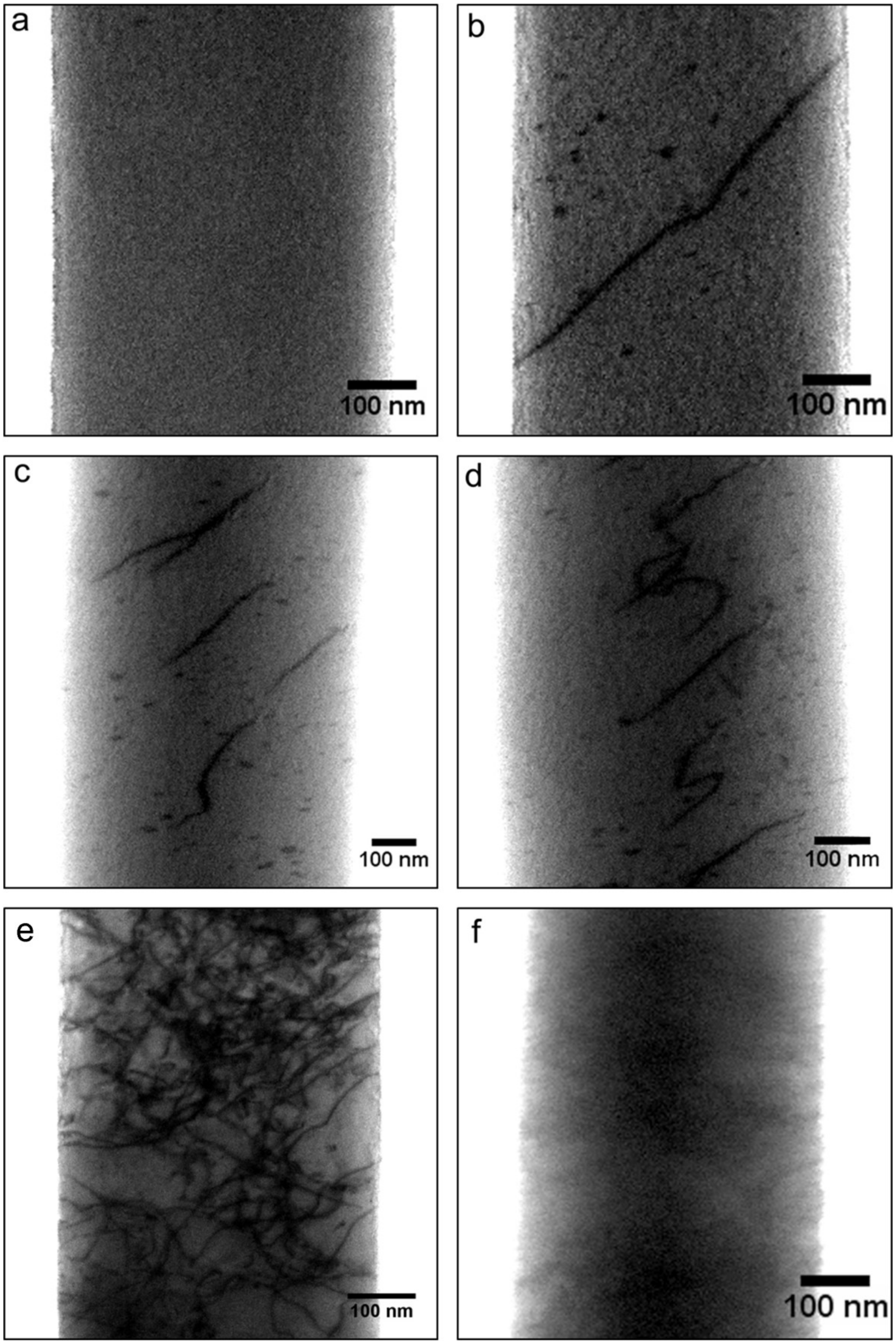

Figure 1.5. Representative bright field STEM micrographs of 4% pre-strained fibers having (a), (b) low, (c), (d) medium, and (e), (f) high dislocation densities. Note that the dislocation density is so large in (f) that the dislocations are difficult to resolve.

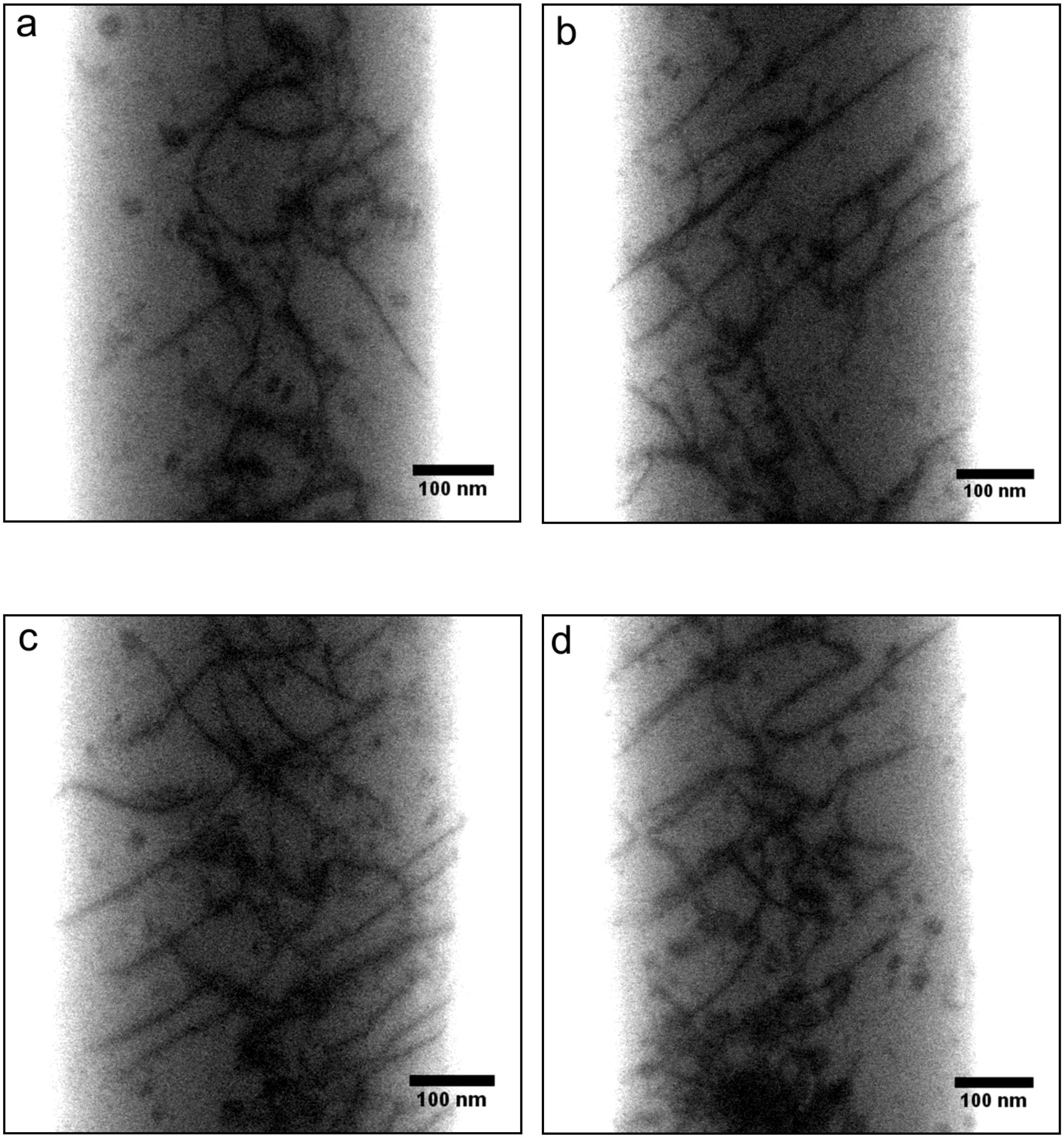

Figure 1.6. Representative bright field STEM micrographs of 16% pre-strained fibers.

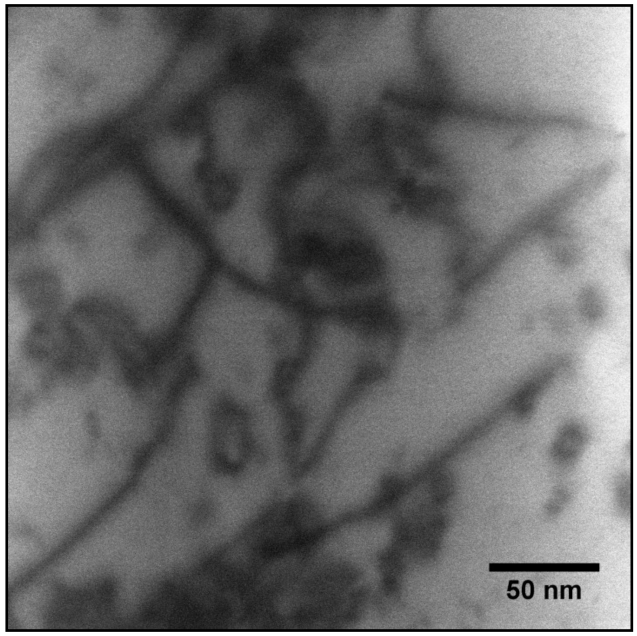

Figure 1.7. Bright field STEM micrograph of 16% pre-strained fibers showing dislocation loops in addition to straight dislocations.

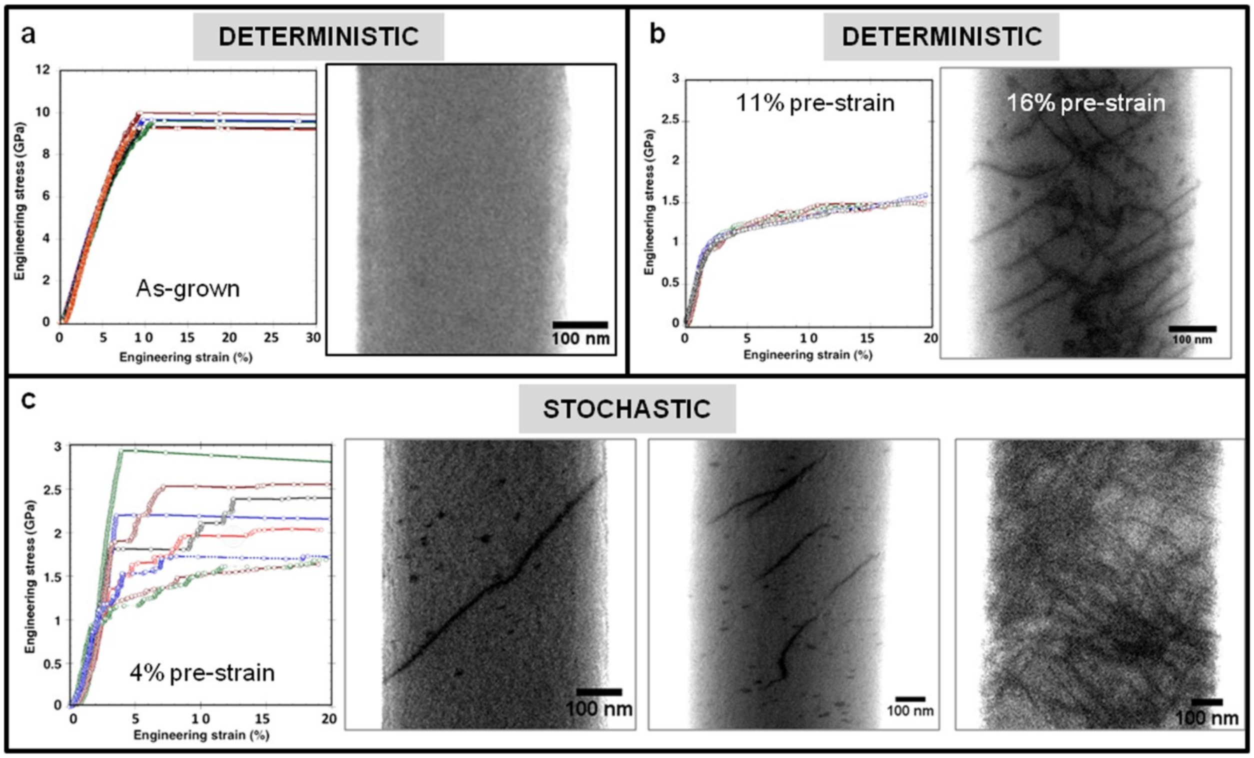

Figure 1.8. Compressive stress-strain plots (Bei *et al.*, 2008) along with microstructure of Mo-alloy fibers showing deterministic behavior: (a) 0% pre-strain (as-grown), (b) 11% / 16% pre-strain and stochastic behavior (c) 4% pre-strain.

CHAPTER II
A simple stochastic model for yielding in specimens with limited number of dislocations

This article will be submitted to the *Acta Materialia*. It hasn't been published anywhere, nor will it be before I turn in the final version of my ETD, so I didn't include a publication statement.

Authors:

P. Sudharshan Phani [1], K. E. Johanns [1], E. P. George [1,2], and G. M. Pharr [1,2]

[1] *Dept. of Materials Science and Engineering, University of Tennessee, Knoxville, TN 37996*

[2] *Materials Science and Technology Division, Oak Ridge National Laboratory, Oak Ridge, TN 37831*

P. Sudharshan Phani's involvement in the article: Developed the model and derived the equations, compared model predictions with experimental results, wrote and revised the article.

Co-researchers' contributions are listed as follows:

K.E. Johanns performed Monte Carlo simulations and assisted in model development and data analysis.

E.P. George provided inputs in model development and manuscript revision.

G.M. Pharr conceived the basic idea and worked with Phani and Johanns to develop the model, helped prepare and revise the article.

Abstract

A simple statistical model is developed based on a random distribution and orientation of dislocations in order to explain recent experimental observations of the strength of small specimens containing a limited number of dislocations. Two different types of randomness are introduced, viz., randomness in the spatial location of the dislocations and randomness in the stress needed to activate them. For convenience, the randomness in the activation stress is modeled by assigning a random Schmid factor to the dislocations. In contrast to previous stochastic models, the current model predicts not only the yield strength in the presence of dislocations but also in their absence. Furthermore, the model predicts the scatter in the yield strength in addition to the mean. The model is found to quantitatively explain the yield strength and scatter in micro-compression / tension tests of Mo-alloy fibers using dislocation densities and arrangements measured by TEM. The results of Brenner's classic tensile tests on metallic whiskers are qualitatively reconciled. The model adds credence to the notion that "smaller is stronger" from a purely statistical point of view.

1. Introduction

Over the past decade, there has been significant interest in the mechanical behavior of materials at small length scales due to the unique mechanistic insights offered by testing specimens whose dimensions approach the average dislocation spacing, as well the miniaturization of engineering components to sub-micrometer scales. This has accentuated the need for better characterization tools and pertinent experiments. One such example is the micro-pillar compression test, wherein the initial yield and flow behavior of micrometer size test specimens has been extensively studied, as recently reviewed by Uchic et al. (Uchic *et al.*, 2009). These experiments offer exciting opportunities to systematically study the effect of specimen size on strength and have given credibility to the popular notion that "smaller is stronger". In small specimens, deformation is often controlled by a limited number of dislocations, and as a result, the yield strength is often very scattered and stochastic as observed by Brenner in his classic tensile tests on metallic whiskers (Brenner, 1956). Brenner had great mechanistic insight, in spite of not having a great deal of supporting microstructural evidence, noting that "the very large scatter in the strength of whiskers as a function of their size indicates that the strengths of the perfect whiskers must be decreased by defects which are distributed statistically in a rather complex manner." (Brenner, 1956). This points not only to the importance of understanding the scatter in strength in such experiments but also the need for a statistically-based approach to model the behavior.

More recently, Johanns et al. (Johanns *et al.*, 2012) have reported results of in-situ micro-tensile tests on 10-30 μm long Mo-alloy fibers having nearly square cross-sections with side lengths ranging from 360 to 550 nm. The fibers were produced by directional solidification of a Mo-NiAl eutectic and were thought to be nearly dislocation free. A large scatter in yield strength was observed in the tensile tests, with strengths ranging from a high near the theoretical strength of ~9.2 GPa down to the bulk strength of ~1 GPa. This was in sharp contrast to micro-pillar compression tests on ~1 μm long specimens of the same material (Bei *et al.*, 2008), wherein the material yielded consistently at the theoretical strength (~9.2 GPa). An important clue to the difference in behavior came from recent TEM observations of the Mo-alloy fibers (Phani *et al.*, 2011), which revealed that the as-grown fibers were not, in fact, dislocation free, but rather contained a few dislocations with an average linear spacing along the fiber length of about 37 μm. At this spacing, the linear dislocation density (number per unit length) is such that there is a high probability of having a strength-reducing dislocation in a 30 μm tensile specimen, whereas the probability of having one in a 1 μm long compression specimen is very small. Thus, a difference in behavior between the tensile and compression specimens is expected.

In this paper, we use this basic idea to develop a weak-link based statistical model that numerically describes the behavior. Most of the prior statistical modeling work has been based on molecular dynamics (Ngan *et al.*, 2006; Zuo and Ngan, 2006) or dislocation dynamics (El-Awady *et al.*, 2009) assuming a Weibull distribution of strengths. In addition, most statistical models for deformation in small specimens have been based on the nucleation of dislocations (Ngan *et al.*, 2006; Zuo and Ngan, 2006) or the activation of pre-existing dislocations (Ng and Ngan, 2008a, b; Parthasarathy *et al.*, 2007), but not both. Here, both are considered since they may simultaneously act to produce scatter in the observed strengths. In this context, the approach taken here provides an estimate of not only the mean value of the yield strength, but also an estimate of the scatter in strength and how it may be distributed. We begin by providing a physical description of the model along with a statistically based mathematical development that describes it, and then move on to applying the model to the Mo-fiber experiments and Brenner's observations for copper whiskers.

2. Modeling approach

Fig. 2.1 shows a schematic overview of the proposed weak-link one-dimensional (1D) model, wherein random test sections of length ℓ are drawn from a large sample space of length L and subjected to compression or tensile testing. If the randomly drawn test sections are dislocation free, then dislocations must first be nucleated and the specimen yields at the theoretical strength. However, if the specimen contains dislocations, then yielding is determined by the dislocation that needs the lowest stress for activation and movement. Hence, the yield strength depends both on the spatial distribution of dislocations and the distribution of their activation strengths. In this way, the dislocation distribution in the test section of length ℓ can be considered to be comprised of two types of randomness, viz., randomness in the spatial distribution of the dislocations and randomness in the strength of the dislocations, i.e., the stress needed to activate them. While the randomness in the spatial distribution is fairly straightforward to describe, the randomness in the activation stress can be modeled in several different ways, viz., a random Schmid factor, variable source length, solute distribution, crystal orientation, etc. For simplicity, the randomness in the activation stress is modeled here by assigning a random Schmid factor to the dislocations, although other types of randomness could also be included in the basic modeling framework. A mathematical description for the model is developed in closed form by simple statistical methods and independently verified using Monte Carlo techniques. The Monte Carlo simulations help not only in validating the analytical model but also in visualizing the scatter in strength expected when only a limited number of tests are conducted.

The model development is presented in four parts. First, a simple model for yielding based on randomness in the spatial distribution of the dislocations is developed in section 2.1. This model is then extended in section 2.2 to include randomness in the activation stress by assigning a random Schmid factor to the dislocations. A mathematical description for the scatter in the yield strength is presented in section 2.3, and finally, the model is extended to two-dimensional (2D) dislocation structures in section 2.4.

The primary assumptions of the model may be summarized as follows:

(i) The dislocations are non-interacting.

(ii) The dislocations are modeled as point defects in the 1D model and as straight-line defects perpendicular to the cross section in the 2D model.

(iii) The model assigns random Schmid factors to the dislocations to simulate the activation of pre-existing dislocations. However, the current framework could be used to model any other physical mechanism that determines activation strength such as random source lengths (Parthasarathy *et al.*, 2007), crystal orientation, solute interaction, etc., which themselves might include other contributions to size dependent behavior.

(iv) Yielding occurs either due to nucleation of dislocations at the theoretical strength or due to the movement of a pre-existing dislocation when the resolved shear stress on the dislocation exceeds the critical resolved shear stress.

(v) Although the model is inherently athermal, it could easily be extended to include thermally activated processes for dislocation nucleation or dislocation motion.

2.1 Yielding for a random spatial distribution of dislocations

We begin by considering the case of a random spatial distribution of dislocations in one-dimension (1D) in which the dislocations are all oriented to have a maximum Schmid factor $s_{max} = 0.5$ and thus have exactly the same strength. This is shown on the left side of Fig. 2.1b. Throughout this paper, σ's will used to indicate tensile strengths while τ's will be used for shear strengths. In samples with a limited number of dislocations, some test specimens will be dislocation-free and thus yield by nucleation of dislocations at the theoretical yield strength, σ_0. However, when dislocations are present, the strength will be reduced and determined from a weak-link perspective by the dislocation with the smallest tensile stress needed to activate its motion, i.e., the dislocation with the largest Schmid factor, in which case the strength will be considerably less than the theoretical strength. For simplicity, we consider that the lower limit on strength is given by the bulk strength, σ_b, which can be related to the critical resolved shear stress τ_{CRSS} by assuming a maximum Schmid factor ($s_{max} = 0.5$) through $\sigma_b = \tau_{CRSS} / s_{max}$. Thus, for the simple case on the left-hand side of Fig. 2.1b, there are only two possible yield strengths depending on the presence or absence of dislocations, viz., the theoretical yield strength, σ_0, or the bulk strength, σ_b. The probabilities of each of these two strength levels can then be used to determine the average yield strength σ_{avg} by a weighted rule of mixtures. From a mathematical perspective, the problem then reduces to determining the probability that there is or is not a dislocation in the test section. As shown in Appendix 2.1, the probability of finding i ($i \leq n$) dislocations in a test section of length ℓ randomly drawn from a large sample space of length L having n dislocations such that the 1D dislocation density is $\rho_{1D} = n/L$ is

$$p(i) = \frac{n!}{(n-i)!i!}\left[\frac{\ell}{L}\right]^i\left[1-\frac{\ell}{L}\right]^{n-i} = \frac{n!}{(n-i)!i!}\left[\frac{\rho_{1D}\ell}{n}\right]^i\left[1-\frac{\rho_{1D}\ell}{n}\right]^{n-i}. \tag{1}$$

If the smaller test section is drawn from a very large sample space, $n \to \infty$ & $L \to \infty : \rho_{1D} = n/L$, Eq. (1) simplifies to

$$\lim_{n\to\infty} p(i) = \lim_{n\to\infty} \frac{n!}{(n-i)!i!}\left[\frac{\rho_{1D}\ell}{n}\right]^i\left[1-\frac{\rho_{1D}\ell}{n}\right]^{n-i} = \frac{(\rho_{1D}\ell)^i}{i\,!}e^{-\rho_{1D}\ell}. \tag{2}$$

This is the probability mass function of the well-known Poisson distribution. The applicability of the Poisson distribution in modeling the stochastic behavior of dislocations in indentation pop-in has been recently discussed by Morris et al. (Morris *et al.*, 2011). Substituting $i = 0$ into Eq. (2), the probability of finding a dislocation-free test section is

$$p(0) = e^{-\rho_{1D}\ell}. \tag{3}$$

On the other hand, the probability of finding at least one dislocation in the test section is 1- $p(0)$=1- $e^{-\rho_{1D}\ell}$. Thus, the average yield strength σ_{avg} determined from a simple weighted average (rule of mixtures) is

$$\sigma_{avg} = \sigma_o e^{-\rho_{1D}\ell} + \sigma_b\left(1-e^{-\rho_{1D}\ell}\right). \tag{4}$$

From Eq. (4) it is apparent that for a given σ_0 and σ_b, the average yield strength depends only on the non-dimensional parameter $\rho_{1D}\ell$, which is the expected number of dislocations in the test section. Alternatively, the parameter $\rho_{1D}\ell$ can be interpreted as the ratio of the test section length (ℓ) to the average spacing of the dislocations (λ_{avg}), where, $\lambda_{avg} = 1 / \rho_{1D}$.

Based on the same simple principles, Fig. 2.2 summarizes the Monte Carlo method used to simulate the models developed in this paper. The number of dislocations (n), length of the large sample space (L), test section length (ℓ), theoretical strength (σ_0), critical resolved shear stress (τ_{CRSS}) and Schmid factor (s) of the dislocations are used as inputs. The dislocations are assigned random locations, and a test section is randomly picked from the large sample space. A yield strength of σ_o is assigned if the test section is dislocation-free, while the dislocation with the highest Schmid factor in the test section (i.e., the weakest link) is used to calculate the yield strength in the presence of dislocations. A large number of iterations (typically 30000) are usually needed to accurately calculate the average yield strength.

Fig. 2.3 shows a comparison of the average yield strength predicted by the simple model with no variation in the activation stress (Eq. (4)) to the Monte Carlo trials using $\sigma_0 = 10$ GPa and $\sigma_b = 1$ GPa. The average yield strength predicted by the model transitions from a higher strength level (theoretical strength) to a lower strength level (bulk strength) as the non-dimensional test section length $\rho_{1D}\ell$ (or ℓ / λ_{avg}) is increased. It is thus apparent that a purely statistical treatment can offer some explanation for the common observation that "smaller is stronger". As expected, there is also good agreement between the average yield strength determined by the analytical model and the Monte Carlo results. The individual Monte Carlo data points from 100 random trials at each level of $\rho_{1D}\ell$ are also shown in the plot. The Monte Carlo data points are slightly staggered vertically in the plot for clarity of presentation. Close examination of these points indicates that for the smaller test sections there are more data points congregated at the theoretical strength (10 GPa) whereas for the larger test sections the data points are clustered at the bulk strength (1 GPa). This is to be expected since the smaller test sections are more likely to be dislocation-free while the larger ones have a greater probability of having dislocations.

2.2 Yielding for random orientation and spatial distribution of dislocations

The model presented in section 2.1 can be extended to include randomness in the stress needed to activate pre-existing dislocations. Such randomness can be modeled in several different ways, for example, a random Schmid factor s, a random rotational orientation for the dislocation (Ng and Ngan, 2008a), a random dislocation source length (Parthasarathy *et al.*, 2007), or through a variety of other strength determining factors such as randomness in the solute distribution, crystal orientation, etc. For simplicity in development, the randomness in strength is modeled here by assigning a random Schmid factor in the range $0 \leq s \leq 0.5$ as schematically shown in Fig. 2.1b (the Schmid factors are shown beside the dislocations), which is equivalent to assigning a random rotational orientation. Following the weak-link assumption, yielding in the presence of dislocations with random Schmid factors is then determined by the dislocation with the highest Schmid factor. Hence, the yield strength of a test section having i dislocations can be expressed as

$$\sigma_Y = \min\left(\frac{\tau_{CRSS}}{s_1}, \frac{\tau_{CRSS}}{s_2} ......, \frac{\tau_{CRSS}}{s_i} \right) \; or, \tag{5a}$$

$$\sigma_Y = \frac{\tau_{CRSS}}{s^*}, \; where \; s^* = \max(s_1, s_2 ..., s_i). \tag{5b}$$

For a test section to have the yield strength given by Eq. (5b), the highest Schmid factor in the test section has to be s^*. The probability of having a highest Schmid factor that falls in the range between s^* and $s^*+\Delta s^*$ in a test section with i dislocations is given by

$$p(s^*) = i \left(\frac{s^*}{s_{\max}} \right)^i \left(\frac{\Delta s}{s^*} \right), \tag{6}$$

where s_{max} is the maximum possible Schmid factor ($s_{max} = 0.5$) and Δs is an infinitesimal increment in Schmid factor. Details of the derivation of this relation are provided in Appendix 2.2. Since the current model is developed based on a weak-link argument, one could also use the Weibull distribution to determine the strength. However, the Weibull distribution (Rinne, 2009) assumes that the strength of a specimen scales based on a function of the form $\sigma \propto (1/V)^{1/m'}$, where V is the volume and m' is the Weibull modulus, while the current model does not need any such assumptions; that is, the strength is simply related to the dislocation density and sample size by incorporating the necessary physical mechanisms.

It is entirely possible that the maximum Schmid factor in a test section is so low that the yield strength calculated using Eq. (5b) is higher than the theoretical strength, σ_0. In such a case, the yield strength in the model would be the theoretical strength due to the fact that it would be easier to nucleate a new dislocation than to move the existing one. The probability of such an event (i.e., the probability that all i dislocations have Schmid factors less than s_{min}) is

$$p(s < s_{min}) = \left(\frac{s_{\min}}{s_{\max}} \right)^i , \qquad (7)$$

where, s_{min} represents the minimum Schmid factor below which nucleation is favored over activation. Similar to the approach presented in section 2.1 to determine the average yield strength, a weighted average is taken to calculate the average yield strength in this case as well.

In all, there are then three possible ways in which the strength can be determined: (1) the theoretical strength due to nucleation of dislocations in dislocation-free test sections; (2) the theoretical strength due to nucleation of dislocations in test sections with dislocations having low Schmid factors ($s < s_{min}$); and (3) a yield strength between the theoretical strength and bulk strength given by Eq. (5b) due to activation of pre-existing dislocations. Hence, the average yield strength based on the weighted average can be written as

$$\sigma_{avg} = \sigma_o p(0) + \sum_{i=1}^{n} \sigma_o p(i) p(s < s_{\min}) + \sum_{s_{\min}}^{s_{\max}} \sum_{i=1}^{n} \frac{\tau_{CRSS}}{s^*} p(i) p(s^*) . \qquad (8)$$

For the limiting case of drawing the test section from a large sample space ($n \to \infty$ & $L \to \infty : \rho_{1D} = n/L$), Eq. (8) simplifies to:

$$\sigma_{avg} = \sigma_o \exp\left(-\rho_{1D}\ell\right) + \sigma_o \exp\left(-\rho_{1D}\ell\right)\left[\exp\left(\frac{\rho_{1D}\ell s_{\min}}{s_{\max}}\right) - 1\right] + \sigma_b \rho_{1D}\ell \exp\left(-\rho_{1D}\ell\right) \int_{s_{\min}}^{s_{\max}} \frac{\exp\left[\left(\frac{\rho_{1D}\ell}{s_{\max}}\right)s\right]}{s} ds. \qquad (9)$$

The integral in the third term of this equation is a standard exponential integral that can be evaluated numerically. The three terms in this equation represent the three types of strength contributions.

Fig. 2.4 compares the average yield strength determined by Eq. (9) to 30000 Monte Carlo simulations for $\sigma_0 = 10$ GPa, $\sigma_b = 1$ GPa and $s_{max} = 0.5$ where it is apparent that the two methods of calculation compare very well. Individual Monte Carlo data points at several discrete specimen lengths from 100 trials are also shown in the plot, with the data points slightly staggered horizontally and vertically for clarity. Unlike the case of random spatial distribution of dislocations (Fig. 2.3), wherein only two discrete strength values are possible, including the randomness in Schmid factors provides for a continuous strength variation from the theoretical strength to the bulk strength, as is evident in the Monte Carlo data points shown in Fig. 2.4. As mentioned earlier, the randomness in activation stress has been modeled by assigning to the dislocations random Schmid factors in the range $0 \leq s \leq 0.5$. Although not shown here, it was verified using Monte Carlo simulations that the yield strength predicted by assuming a random spatial orientation of dislocations (random rotations θ) yields identical results.

2.3 Modeling scatter in the yield strength

The Monte Carlo data points shown in Fig. 2.4 clearly show a large scatter in yield strength at intermediate values of $\rho_{1D}\ell$. In this section, an analytical treatment is presented to model this scatter and derive a closed-form solution for the scatter bounds. The scatter bounds can be defined in several different ways. Here, we have chosen to define the bounds as the limiting strength values within which a given percentage of the strengths lie. For example, 90 % scatter bounds (the typical value that will be used in this paper) would exclude the top and bottom 5% of the strengths and include the middle 90% of the strengths. The procedure for determining the upper bound is described in detail; similar arguments can be used to determine the lower bound.

In order to determine the upper bound of scatter, two different cases need to be considered:

Case 1 - the theoretical strength constitutes more than the top α fraction of the strengths (α is usually taken here to be 0.05),

Case 2 - the theoretical strength constitutes less than the top α fraction of the strengths.

For *Case 1*, the upper bound (σ_{UB}) is the theoretical strength itself. However, as $\rho_{ID}\ell$ increases, the contribution of lower strengths increases and the theoretical strength no longer constitutes the top α fraction of the strengths. Hence, there is a cutoff $(\rho_{ID}\ell)_{UB}$ up to which theoretical strength constitutes the top α fraction of the strengths but above which the upper bound falls. The cutoff in $\rho_{ID}\ell$ can be determined by equating the probabilities of having theoretical strengths to α, which yields

$$p(\sigma_o) = \lim_{n \to \infty} \left[p(0) + \sum_{i=1}^{n} p(i) p(s < s_{\min}) \right] = \alpha. \tag{10}$$

The corresponding probabilities can be substituted into this equation to give the cutoff in $\rho_{ID}\ell$ as

$$(\rho_{ID}\ell)_{UB} = \frac{\ln \alpha}{\frac{s_{\min}}{s_{\max}} - 1}, \tag{11}$$

where, $\sigma_{UB} = \sigma_o$, for $\rho_{ID}\ell \le (\rho_{ID}\ell)_{UB}$.

For *case 2*, the upper bound (σ_{UB}) can be determined by rank ordering the strengths in descending order and identifying the lowest strength up to which the top α fraction of the strengths lie. This can be expressed as

$$\lim_{n\to\infty}\left[p(0)+\sum_{i=1}^{n}p(i)p(s<s_{\min})+\sum_{s_{\min}}^{s_{UB}}\sum_{i=1}^{n}p(i)p(s^*)\right]=\alpha, \tag{12}$$

where s_{UB} is the Schmid factor corresponding to the upper bound (σ_{UB}). Eq. (12) can be simplified to give the upper bound of the strength as

$$\sigma_{UB}=\sigma_b\left(\frac{\rho_{ID}\ell}{\rho_{ID}\ell+\ln\alpha}\right), \text{ for } \rho_{ID}\ell\geq(\rho_{ID}\ell)_{UB}. \tag{13}$$

The lower bounds for both the cases can be obtained by substituting 1-α for α in Eq. (11) and Eq. (13), respectively.

Fig. 2.5a shows the average yield strength along with the predicted upper and lower scatter bounds for σ_0 = 10 GPa, σ_b = 1 GPa, s_{max} = 0.5 and α = 0.05 (90 % scatter bounds). Results of 100 Monte Carlo trials at several discrete specimen lengths are also shown for comparison. It is evident from the plot that the model accurately captures the scatter bounds predicted by the Monte Carlo calculations. Fig. 2.5b shows an expanded view of Fig. 2.5a with more Monte Carlo trials (10000), wherein the capability of the model to precisely capture the bounds for the shorter specimens is apparent. While the large scatter in the yield strength for $\ell / \lambda_{avg} \sim 1$ is reasonable, it is interesting to note that there is considerable scatter even for a very small value of ℓ / λ_{avg} due to the finite probability of finding dislocations in small test sections drawn from a large sample space having a random distribution of dislocations.

A closer look at Fig. 2.5a indicates that the distribution of strengths at a given value of ℓ / λ_{avg} is not Gaussian but is skewed to extremes of strengths depending on the value of ℓ / λ_{avg} . For example, the distribution is heavily skewed towards higher strengths for small values of ℓ / λ_{avg} (ℓ / λ_{avg} < 0.1) where the test section is expected to be dislocation-free either due to low dislocation density or small test section length or a combination of both. At the other extreme, for high values of ℓ / λ_{avg} (ℓ / λ_{avg} > 10), the distribution is skewed towards lower strengths where the probability of finding at least one dislocation with a high Schmid factor is high due to a high dislocation density or a large test section length or both. Interestingly, at intermediate values of ℓ / λ_{avg} ($\ell / \lambda_{avg} \sim 1$), where a large scatter in yield strength is observed, the distribution predominantly shows strengths close to the theoretical or bulk strength indicating that the intermediate strengths are less probable. This distribution is somewhat surprising as it seems counter-intuitive to have lower probabilities for intermediate strengths. It results from the fact that while the probability of all the possible Schmid factors is identical, the fact that yielding is dictated by the dislocation with the highest Schmid factor (weakest link) requires all the dislocations in the test section to have a relatively low Schmid factor to exhibit an intermediate yield strength, which itself is a low probability event.

2.4 Extending the model to 2D dislocation structures

The model developed here can be easily extended to 2D by simple arguments. Fig. 2.6a shows a schematic representation of a random spatial distribution and orientation of n dislocations in a 2D specimen of area A_0 such that the dislocation density $\rho_{2D} = n/A_0$ (number per unit area rather than per unit length). Fig. 2.6b shows a test section of area A ($A \leq A_0$) randomly drawn from the larger feature having n dislocations. This problem is similar to the one shown in Fig. 2.1, except for the fact that the 1D specimen has been extended to 2D. Accordingly, the probabilities can be derived by following the same procedures as those presented in section 2.1 and Appendix 2.1. The probabilities in 2D can be obtained by replacing the test section length (ℓ) by the test section area (A) and substituting the corresponding 2D dislocation density ρ_{2D}. Hence, the probability of finding i ($i \leq n$) dislocations in the test section of area A is

$$p(i) = \frac{n!}{(n-i)!i!}\left[\frac{A}{A_0}\right]^i\left[1-\frac{A}{A_0}\right]^{n-i} = \frac{n!}{(n-i)!i!}\left[\frac{\rho_{2D}A}{n}\right]^i\left[1-\frac{\rho_{2D}A}{n}\right]^{n-i}. \qquad (14)$$

All the other equations derived in 1D can be similarly extended to 2D by replacing the length by area and using the corresponding dislocation density. Note that the average spacing of the dislocations in the 2D model can be written as, $\lambda_{avg} = (\rho_{2D})^{-0.5}$.

3. Comparison with experimental results

3.1 Micro-compression / tensile testing of Mo-alloy fibers

The yield strengths predicted by the model are now compared to the experimental data for micro-compression / tensile testing of as-grown and pre-strained Mo-alloy fibers ((Bei *et al.*, 2008) for compression and (Johanns *et al.*, 2012) for tension). The only inputs to the model are the theoretical strength (σ_0), the bulk strength (σ_b), the critical resolved shear stress (τ_{CRSS}) and the dislocation density (ρ_{1D} or ρ_{2D}). The dislocation densities were obtained from the TEM observations of Sudharshan Phani et al. (Phani *et al.*, 2011). For the as grown fibers, they found that dislocations were occasionally found along the fiber length with an average spacing of 37 μm, giving a linear dislocation density ρ_{1D} = 2.7 x 10^4 m^{-1}. After compressively pre-straining to 16%, the dislocation density became more uniform and increased significantly to a two-dimensional density (number per unit area) or three-dimensional density (line length per volume) of 4.4 x 10^{13} m^{-2}. The other model inputs used for calculations are those proposed by Bei et al. (Bei *et al.*, 2008), specifically σ_0 = 9.2 GPa, σ_b = 1.0 GPa, and τ_{CRSS} = 0.5 GPa.

Fig. 2.7 shows the experimental data for the as-grown and 16% pre-strained Mo-alloy fibers and compares it to the model predictions for the scatter in yield strength. The dislocation densities used for the various pre-strain levels are shown directly on the plot. In order to compare specimens with different dislocation densities and lengths, the yield strengths have been plotted against the non-dimensional specimen length ℓ / λ_{avg}, which is the ratio of test section length to the average spacing of dislocations, where the average dislocation spacing (λ_{avg}) was determined from $\lambda_{avg} = 1 / \rho_{1D}$ or $\lambda_{avg} = (\rho_{2D})^{-0.5}$. As discussed earlier, with increasing specimen length, the model predicts a transition in yield strength from an upper strength level, the theoretical strength σ_0, to a lower strength level, the bulk strength σ_b, with a large amount of scatter at intermediate values of ℓ / λ_{avg}. As shown in the figure, the model prediction for the upper and lower bounds of yield strength closely mimics the experimental data. The as-grown compression pillars with lengths of around 1μm yield consistently at the theoretical yield strength, while there is a large amount of scatter for as-grown fibers tested in tension with lengths in the range 10-30 μm, both of which are predicted by the model. The model also accurately predicts the lower strengths and absence of scatter for the 16% pre-strained fibers tested in tension; these samples yield consistently at the bulk strength because they contain so many dislocations. It is thus evident from this figure that the size effect (shorter specimens are stronger) and the scatter in the yield strength can both be explained based on the stochastics of having dislocations in the test section.

3.2 Brenner's metallic whisker strengths

The current model can also be applied to the results of the classic whisker tests of Brenner (Brenner, 1956), who tensile tested small whiskers with diameters in the range 1.2 to 15.2 μm. However, due to the lack of dislocation density data for the whiskers, one needs to make a reasonable guess of the dislocation density to be used in the model, and hence the experimental results can be only qualitatively reconciled. Here, we will assume a relatively small dislocation density of 2×10^8 m^{-2}, which is consistent with the notion that some of the whiskers were thought to be close to dislocation-free. Another difficulty in analyzing Brenner's data is that while he provided data on the yield strength for different whisker diameters, the corresponding lengths of the whiskers were not reported (the range of lengths was 1 to 4 mm), so we cannot apply the model exactly as we did for the Mo-alloy fibers. Rather, we assume here that the diameter of the fibers can be used to gauge the dislocation contents. In order to use our 2D model, we assume that the length of the whisker is linearly proportional to the diameter such that the smallest diameter whisker (1.2 μm) has a length of 1mm and the largest diameter whisker (15.2 μm) has a length of 4 mm.

Subject to these constraints and uncertainties, Fig. 2.8 compares the predictions of the 2D model developed here to Brenner's data for copper whiskers. The assumed model parameters were: σ_0 = 300 kg/mm^2, σ_b = 40 kg/mm^2, τ_{CRSS} = 20 kg/mm^2 and ρ_{2D} = 2×10^8 m^{-2}. In spite of the abovementioned uncertainties, there is relatively good agreement between Brenner's power law best-fit curve to the experimental data and the predictions of the model based on a limited number of Monte Carlo simulations. In addition, most of the experimental data fall within the scatter bounds predicted by the model. Hence, the simple model can be used qualitatively and semi-quantitatively to reconcile the observed size effect and scatter in Brenner's data.

4. Comments on the relationship between strength and specimen size

Finally, we wish to use the model to comment on the expected behavior of a log-log plot of yield strength vs. specimen size, such as that shown in Fig. 2.9a. Such plots have recently received a great deal of attention, with the slope in the mid-range being interpreted as having important mechanistic implications (Kraft *et al.*, 2010; Uchic *et al.*, 2009). For the model with a random spatial distribution of dislocations presented in section 2.1, an expression for the maximum value of the slope can be derived in a simple closed form. Fig. 2.9a shows the model prediction for the yield strength as a function of specimen length ℓ, wherein three different regimes of strength are apparent. In regimes 1 and 3, the strength is close to the theoretical strength and bulk strength, respectively, with slopes close to zero. However, in regime 2, the yield strength transitions from the higher strength regime (theoretical strength) to the lower strength regime (bulk strength), and there is an apparent "size effect" in strength characterized by a slope *m*. The boundaries of the transition regime (regime 2) were determined by calculating the strength at which there is 10 % deviation from the theoretical and bulk strengths, and an "average slope" was determined by a linear fit of strengths inside these boundaries. The maximum value of the slope (m_{max}) can be determined from

$$m_{\max} = -W\left(\frac{\sigma_0 - \sigma_b}{\sigma_b} e^{-1}\right), \tag{15}$$

where, *W* is the Lambert W function. Both measures of slope are plotted as a function of $(\sigma_0-\sigma_b)/\sigma_b$ in Fig. 2.9b. Details of the derivation are provided in Appendix 2.3.

While Eq. (15) gives the maximum value of the slope in regime 2 for the simple case of random spatial distribution of dislocations presented in section 2.1, the corresponding maximum and average slope for the case of random spatial distribution and orientation of dislocations (section 2.2) can be numerically determined using Eq. (9) in conjunction with the procedure outlined in Appendix 2.3. These are also plotted in Fig. 2.9b, where it is apparent that the additional randomness in orientation does not significantly change the slope. Note that based on the current statistical modeling approach, the yield strength transitions from a higher strength regime (theoretical strength) to a lower strength regime (bulk strength) and the slope in the transition regime (maximum slope and average slope) is uniquely determined only by these strength levels and is not a function of the dislocation density or specimen size. Hence, the non-dimensional parameter of prime importance in determining the slope is $(\sigma_0-\sigma_b)/\sigma_b$. The range of $(\sigma_0-\sigma_b)/\sigma_b$ shown in the plot conservatively covers most engineering materials. It is interesting to note that the average slope is between 0 and -2.0 for this range, and that for the Mo-alloy fibers the average slope predicted by the model based on the known material parameters is -0.72. This is very close to a recent compilation (Kim *et al.*, 2010) of slopes measured from micro-pillar tests on Mo (-0.48 in tension and -1.07 in compression). These observations thus suggest that there may be an explanation for the observed slopes based on simple statistical concepts.

5. Summary and conclusions

A simple statistical model is developed based on a random spatial distribution and orientation of dislocations in order to explain recent experimental observations of the yield strength of small specimens containing a limited number of dislocations. The model predicts not only the yield strength in the presence of dislocations but also in their absence. The average yield strength for a given dislocation density transitions with specimen size from a higher strength level (the theoretical strength) to a lower strength level (the bulk strength), giving credence to the notion that "smaller is stronger" from a purely statistical point of view. In addition to predicting the average yield strength, the scatter in yield strength is also predicted. The model reconciles the discrepancy in the yield strength and scatter observed in micro-compression and micro-tensile tests of Mo-alloy fibers using dislocation densities and arrangements measured by TEM. The scatter in yield strength of Brenner's metallic copper whiskers during tensile testing is also qualitatively explained by the model, and the expected range of the power law slope of yield strength vs. specimen size is predicted from a purely statistical approach. The model can be readily extended to other size dependencies in small-scale mechanics, including indentation pop-in.

Acknowledgements

This work was supported by the US Department of Energy, Office of Basic Energy Sciences, Materials Sciences and Engineering Division.

References

Bei, H., Shim, S., Pharr, G. M., & George, E. P. 2008. Effects of pre-strain on the compressive stress-strain response of Mo-alloy single-crystal micropillars. ***Acta Mater***, 56(17): 4762-4770.

Brenner, S. S. 1956. Tensile Strength of Whiskers. ***J Appl Phys***, 27(12): 1484-1491.

El-Awady, J. A., Wen, M., & Ghoniem, N. M. 2009. The role of the weakest-link mechanism in controlling the plasticity of micropillars. ***J Mech Phys Solids***, 57(1): 32-50.

Johanns, K. E., Sedlmayr, A., Phani, P. S., Monig, R., Kraft, O., George, E. P., & Pharr, G. M. 2012. In-situ tensile testing of single-crystal molybdenum-alloy fibers with various dislocation densities in a scanning electron microscope. ***J Mater Res***, 27(3): 508-520.

Kim, J. Y., Jong, D. C., & Greer, J. R. 2010. Tensile and compressive behavior of tungsten, molybdenum, tantalum and niobium at the nanoscale. ***Acta Mater***, 58(7): 2355-2363.

Kraft, O., Gruber, P. A., Monig, R., & Weygand, D. 2010. Plasticity in Confined Dimensions. ***Annu Rev Mater Res***, 40: 293-317.

Morris, J. R., Bei, H., Pharr, G. M., & George, E. P. 2011. Size Effects and Stochastic Behavior of Nanoindentation Pop In. ***Phys Rev Lett***, 106(16).

Ng, K. S., & Ngan, A. H. W. 2008a. Breakdown of Schmid's law in micropillars. ***Scripta Mater***, 59(7): 796-799.

Ng, K. S., & Ngan, A. H. W. 2008b. Stochastic theory for jerky deformation in small crystal volumes with pre-existing dislocations. ***Philos Mag***, 88(5): 677-688.

Ngan, A. H. W., Zuo, L., & Wo, P. C. 2006. Size dependence and stochastic nature of yield strength of micron-sized crystals: A case study on Ni3Al. ***Proc R Soc London A***, 462(2070): 1661-1681.

Parthasarathy, T. A., Rao, S. I., Dimiduk, D. M., Uchic, M. D., & Trinkle, D. R. 2007. Contribution to size effect of yield strength from the stochastics of dislocation source lengths in finite samples. ***Scripta Mater***, 56(4): 313-316.

Phani, P. S., Johanns, K. E., Duscher, G., Gali, A., George, E. P., & Pharr, G. M. 2011. Scanning transmission electron microscope observations of defects in as-grown and pre-strained Mo alloy fibers. ***Acta Mater***, 59(5): 2172-2179.

Rinne, H. 2009. ***The Weibull distribution : A handbook***. Boca Raton: CRC Press.

Uchic, M. D., Shade, P. A., & Dimiduk, D. M. 2009. Plasticity of Micrometer-Scale Single Crystals in Compression. ***Annu Rev Mater Res***, 39: 361-386.

Zuo, L., & Ngan, A. H. W. 2006. Molecular dynamics study on compressive yield strength in Ni3Al micro-pillars. ***Philos Mag Lett***, 86(6): 355-365.

Appendix 2.1.

Probability of having *i* dislocations in a test section of length ℓ randomly drawn from a sample space of length *L*

Let a large sample space of length L be discretized into k identical parts of length Δx. Let the test section of length ℓ have k' parts such that,

$$k = \frac{L}{\Delta x} \text{ and } k' = \frac{\ell}{\Delta x} \tag{A1}$$

The probability of having exactly i dislocations in the test section is

$$p(i) = \frac{\text{no. of ways of arranging } 'i' \text{ dislocations in the test section}}{\text{Total no. of ways of arranging all the dislocations}} = \frac{{}^{k'}C_i \, {}^{k-k'}C_{n-i}}{{}^{k}C_n}. \tag{A2}$$

Substituting the values of k and k' from Eq. (A.1) and taking the limiting case of an infinitesimal length increment ($\Delta x \to 0$), the probability becomes

$$p(i) = \lim_{\Delta x \to 0} \left[\frac{\prod_{a=0}^{i-1} \left(\frac{\ell}{\Delta x} - a \right) \prod_{a=0}^{n-i-1} \left(\frac{L-\ell}{\Delta x} - a \right)}{\prod_{a=0}^{n-1} \left(\frac{L}{\Delta x} - a \right)} \right] \left[\frac{(n)!}{(n-i)!(i)!} \right]. \tag{A3}$$

This equation can be further simplified to

$$p(i) = {}^{n}C_i \left[\frac{\ell}{L} \right]^{i} \left[1 - \frac{\ell}{L} \right]^{n-i}. \tag{A4}$$

Appendix 2.2.

Probability of having a highest Schmid factor of s^* in a test section with i dislocations

To estimate the probability of having a highest Schmid factor of s^* in the test section, we discretize the Schmid factor domain [0 s_{max}] into infinitesimal increments of size Δs and calculate the probability of having at least one dislocation with a Schmid factor between s^* and $s^* + \Delta s$ and all the remaining dislocations having Schmid factors less than s^*.

The probability of all the i dislocations having Schmid factors less than s* is

$$p(s < s^*) = \left(\frac{s^*}{s_{\max}} \right)^i . \tag{A5}$$

The probability of having at least one dislocation with Schmid factor between s^* and s^* + Δs, given that all the dislocations have Schmid factors less than s^* is

$$p(s^*) = p(s < s^* + \Delta s) - p(s < s^*) = \left[\frac{s^* + \Delta s}{s_{\max}} \right]^i - \left[\frac{s^*}{s_{\max}} \right]^i . \tag{A6}$$

Under the limiting case of small Δs, the above equation can be simplified by Taylor expansion to

$$p(s^*) = i \left(\frac{s^*}{s_{\max}} \right)^i \left(\frac{\Delta s}{s^*} \right) . \tag{A7}$$

Appendix 2.3.

Maximum power law slope of yield strength vs. specimen size

The average yield strength for a random spatial distribution of dislocations is given by Eq. (4). The power law slope m of the average yield strength (σ_{avg}) vs. specimen size (ℓ) is then given by

$$m = \frac{d}{d\ln\ell}\ln\sigma_{avg} = -\frac{(\sigma_o - \sigma_b)e^{-\rho_{1D}\ell}\rho_{1D}\ell}{(\sigma_o - \sigma_b)e^{-\rho_{1D}\ell} + \sigma_b}. \quad \text{(A8)}$$

The maximum value of the slope (m_{max}) obtained by equating the derivative of the above equation to zero is:

$$m_{\max} = 1 - \rho_{1D}\ell^* = -W\left(\frac{\sigma_o - \sigma_b}{\sigma_b}e^{-1}\right), \quad \text{(A9)}$$

where,. $\ell^* = \dfrac{W\left(\dfrac{\sigma_o - \sigma_b}{\sigma_b}e^{-1}\right) + 1}{\rho_{1D}}$ (A10)

Here, W is the Lambert W function and ℓ^* is the specimen length at which the maximum slope occurs.

The range of possible slopes then becomes $-W\left(\dfrac{\sigma_o - \sigma_b}{\sigma_b}e^{-1}\right) \le m \le 0$ and is independent of the dislocation density.

Appendix 2.4.

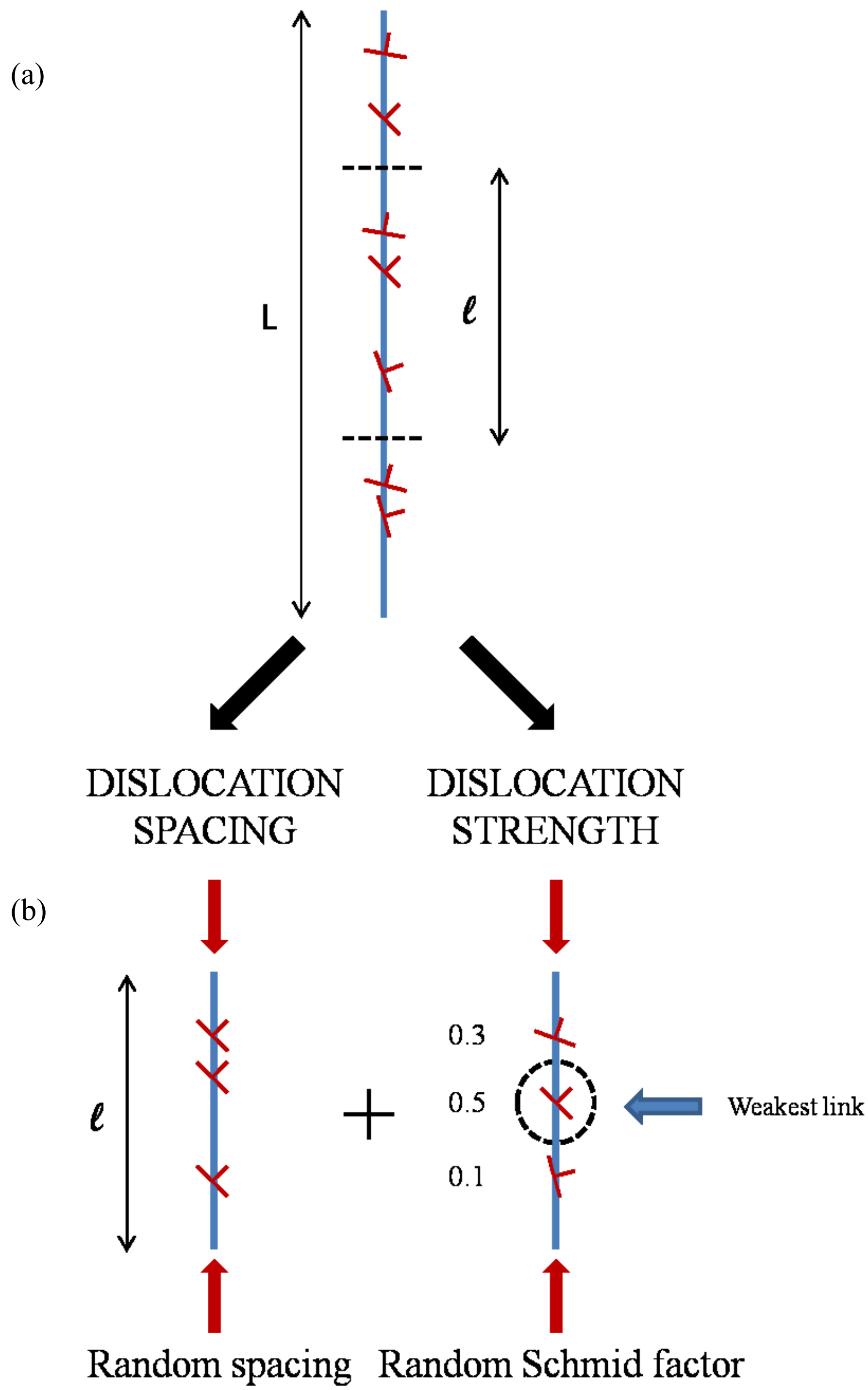

Figure 2.1. Generic framework to model the yield strength of small one-dimensional specimens with a limited number of dislocations.

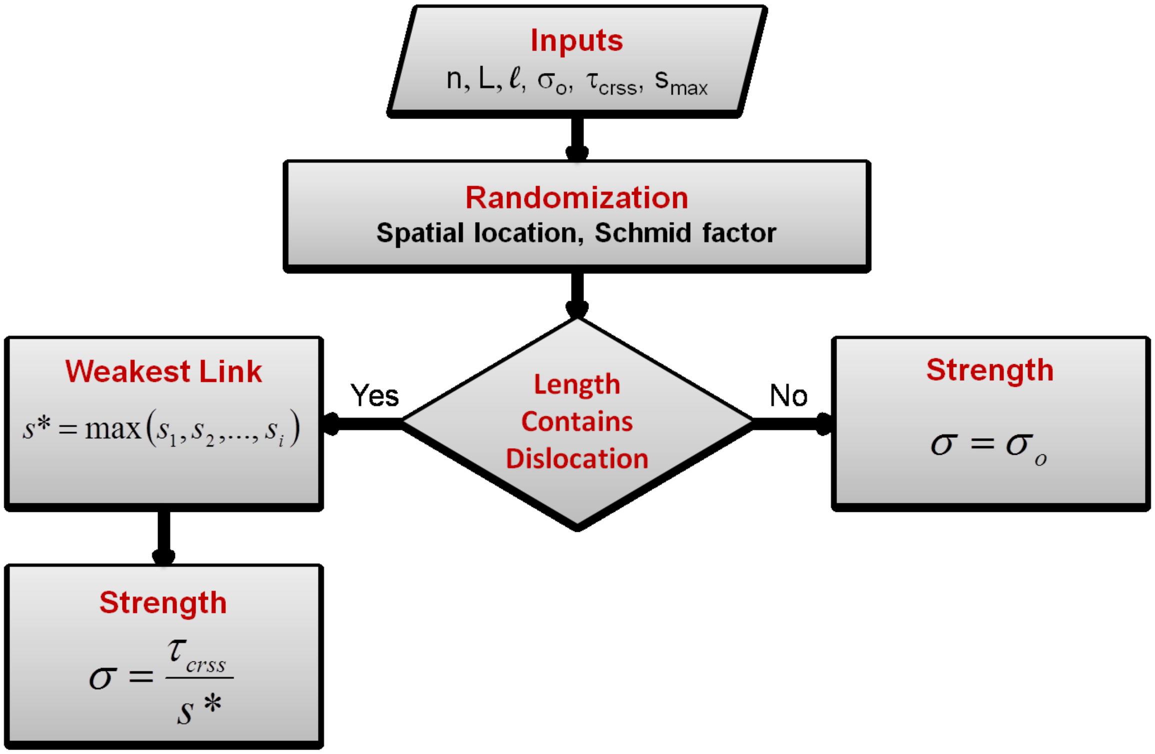

Figure 2.2. Flow chart for Monte Carlo calculation procedures.

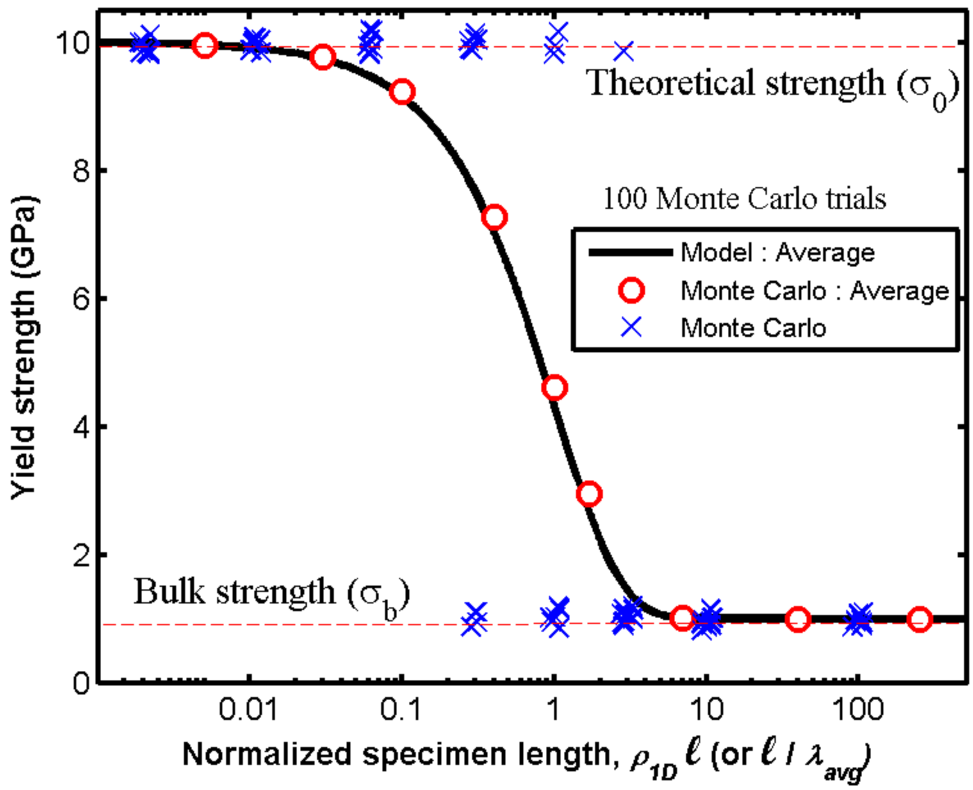

Figure 2.3. Model predictions for the dependence of the yield strength on the non-dimensional specimen length based on random dislocation locations with a fixed Schmid factor of 0.5. Results for 100 Monte Carlo simulations are shown for comparison at several discrete specimen lengths.

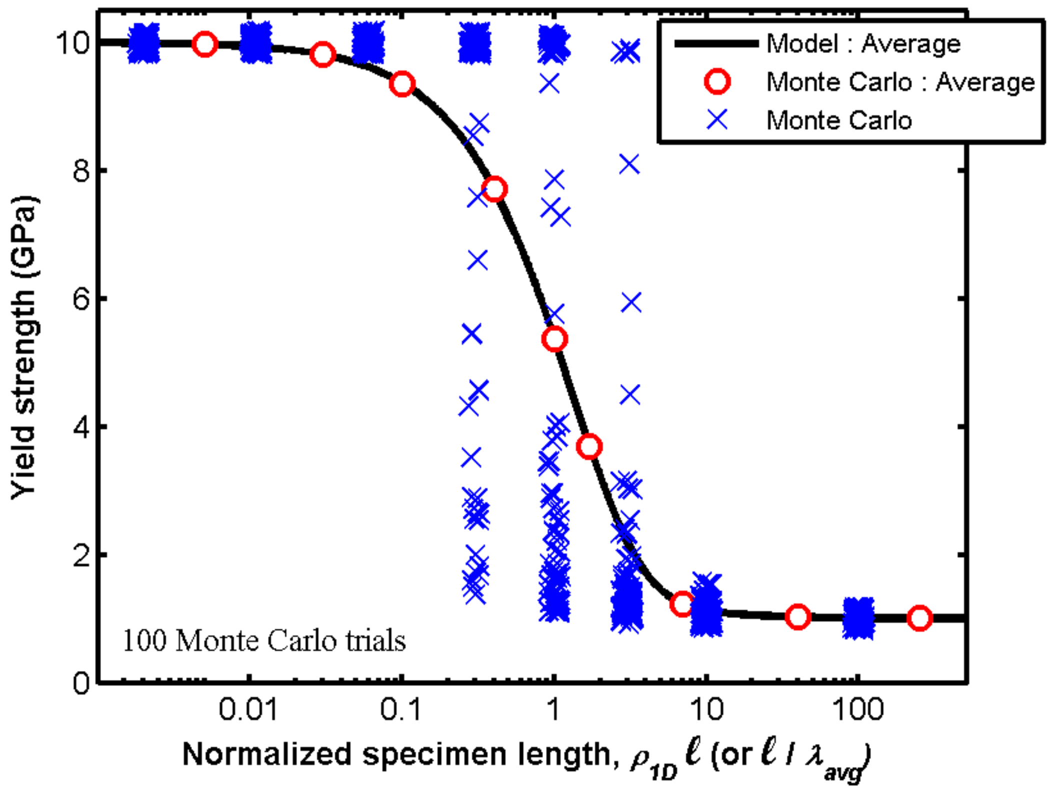

Figure 2.4. Model predictions for the dependence of the yield strength on the non-dimensional specimen length based on random dislocation locations with a random Schmid factor in the range $0 \leq s \leq 0.5$. Results for 100 Monte Carlo simulations are shown for comparison at several discrete specimen lengths.

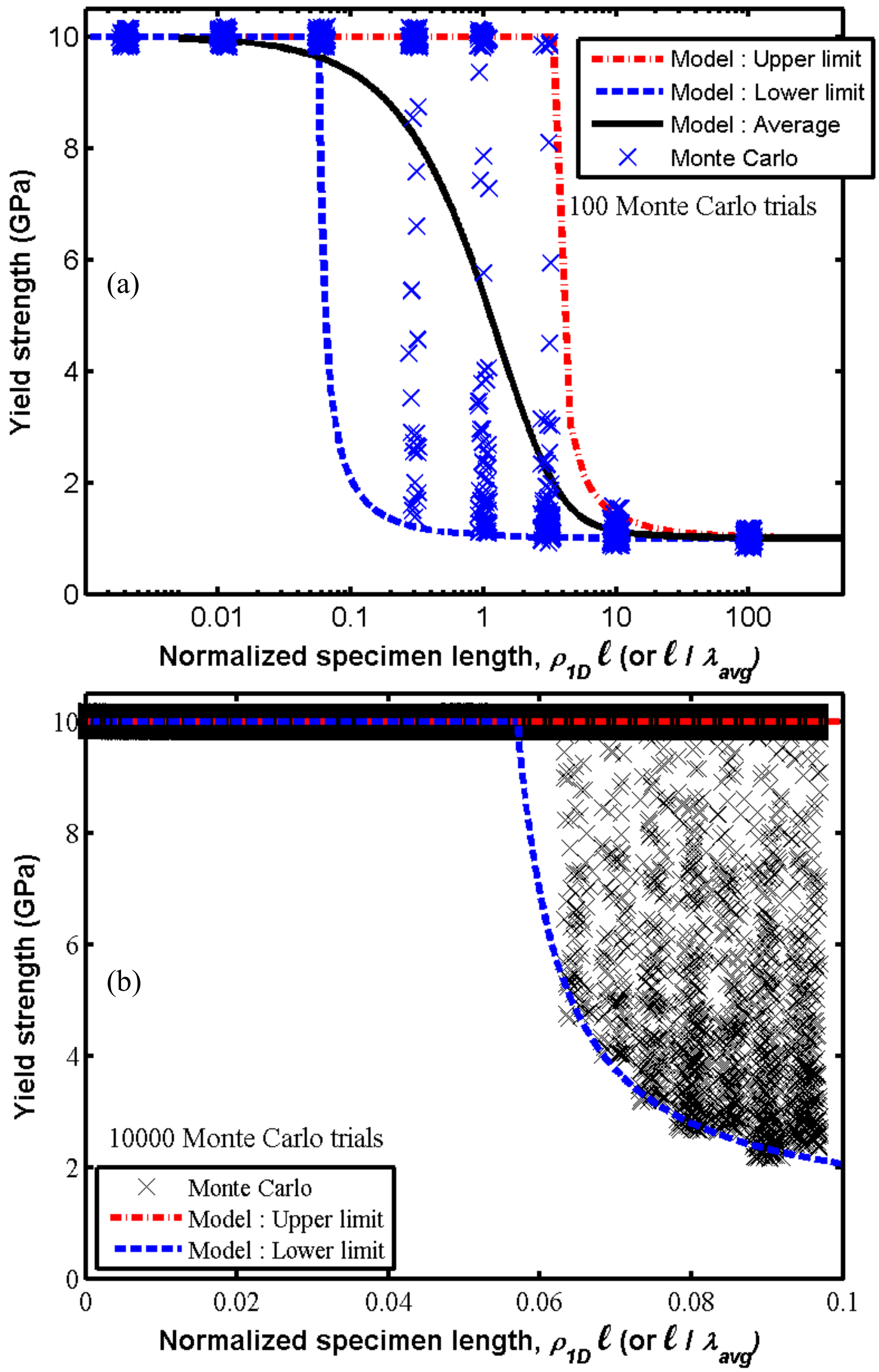

Figure 2.5. Comparison of scatter in strength predicted by model and Monte Carlo simulations: (a) over the entire range of interest; and (b) details of the behavior for shorter specimens.

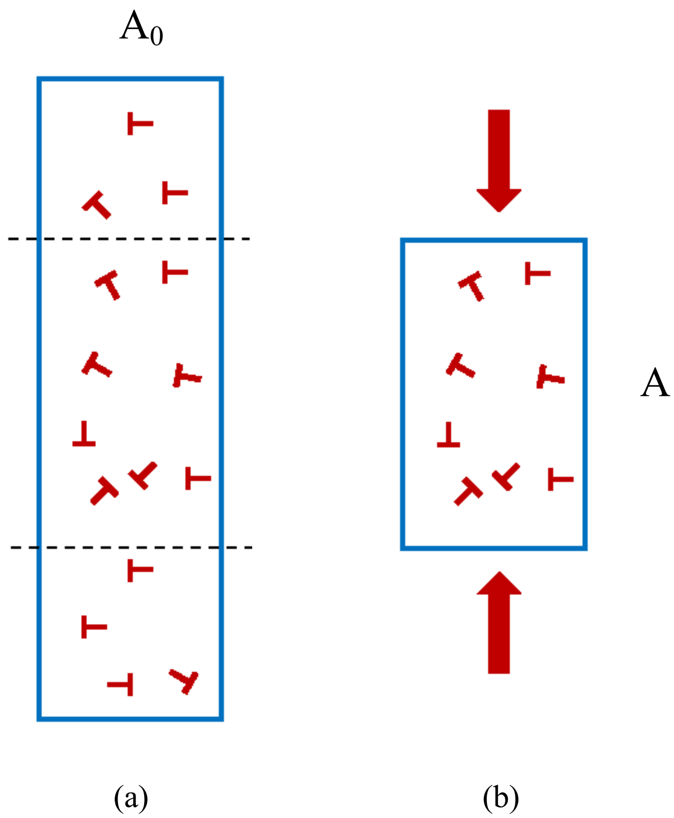

Figure 2.6. Schematic of random spatial distribution and Schmid factor for dislocations in a 2D specimen: (a) large sample space of area A_0, and (b) a test section of area A.

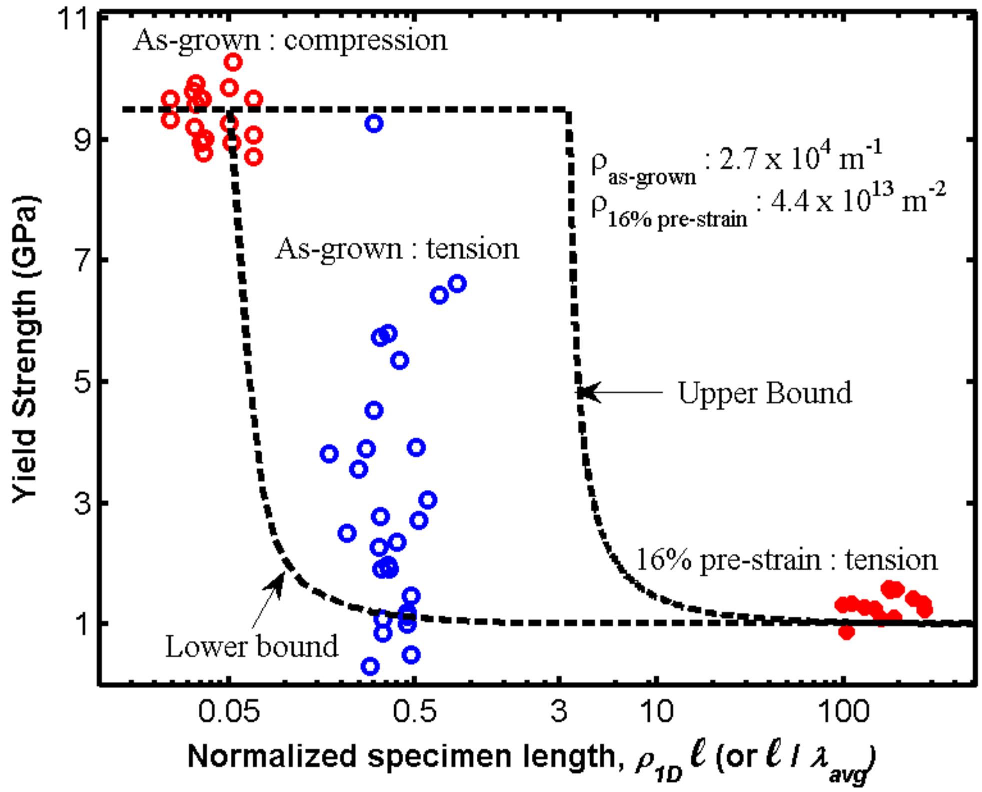

Figure 2.7. Comparison of model predictions and experimental results for compression and tension of Mo-alloy fibers.

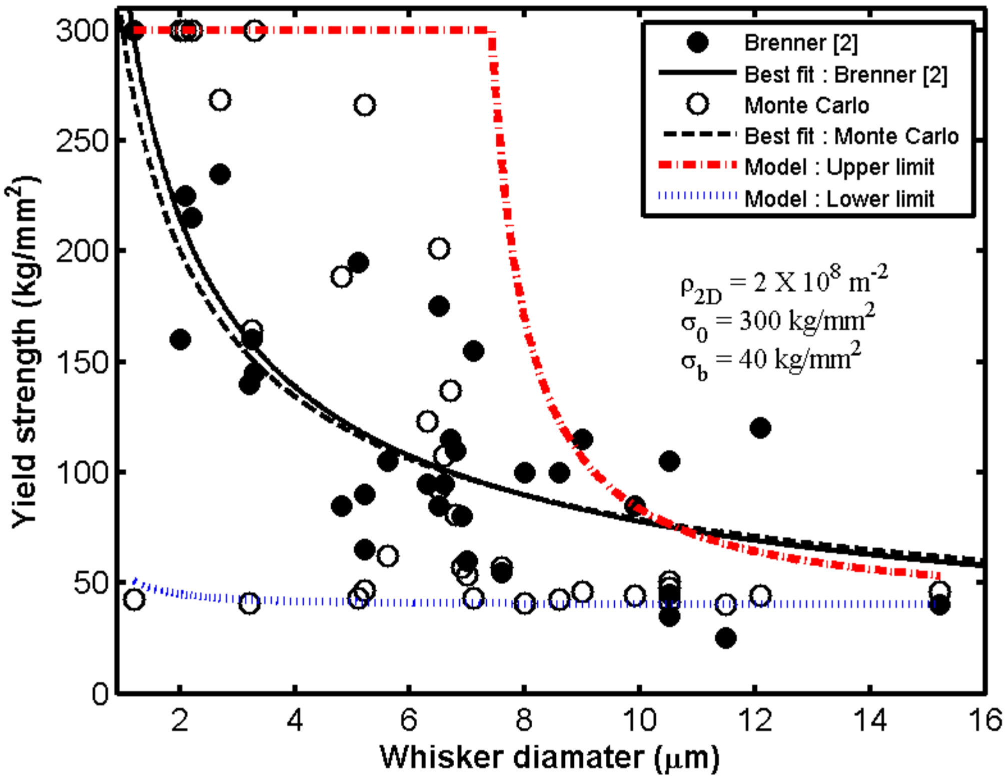

Figure 2.8. Comparison of the model to the experimental data of Brenner obtained in tensile tests of small-diameter copper whiskers (Brenner, 1956).

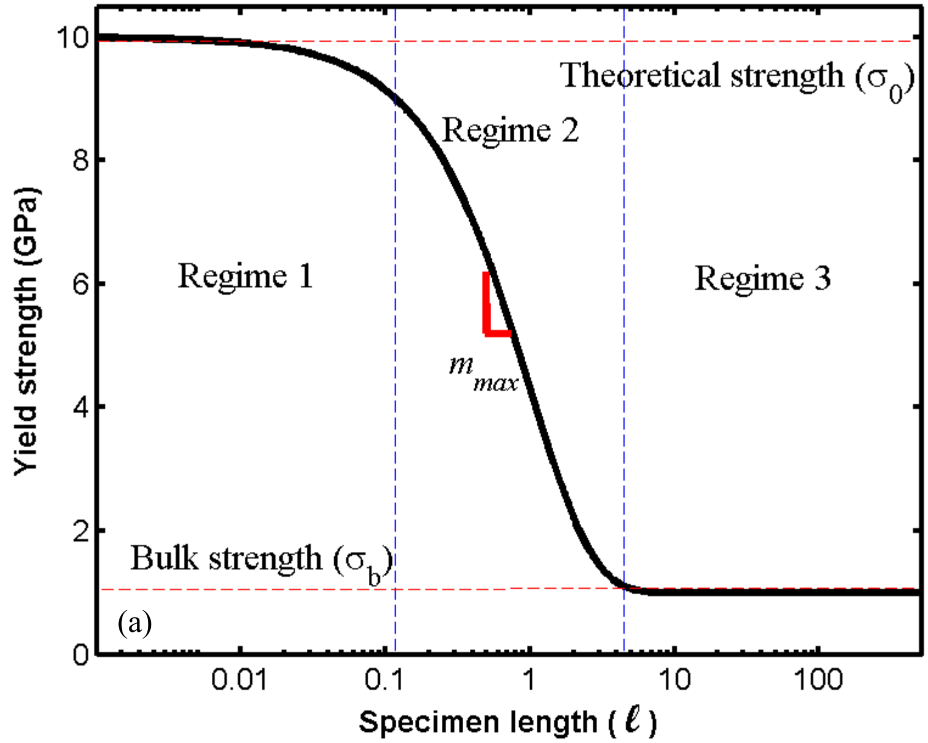

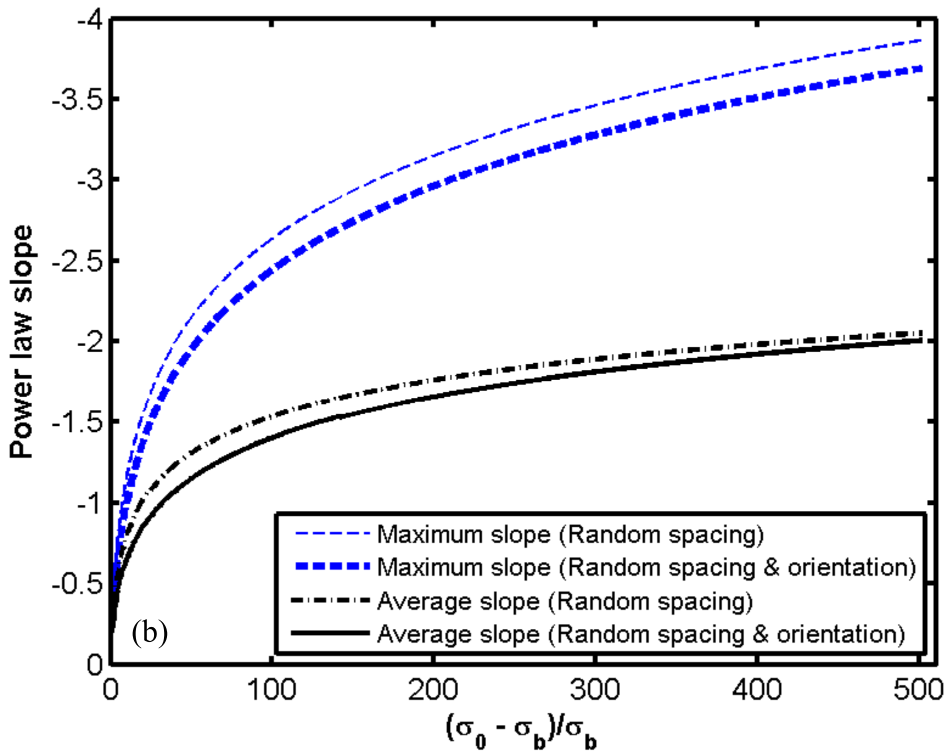

Figure 2.9. Model predictions for: (a) yield strength as a function of specimen length; and (b) power law slope for a wide range of theoretical and bulk strengths.

CHAPTER III
A stochastic model for the size dependence of spherical indentation pop-in

This article will be submitted to the *Journal of Materials Research*. It hasn't been published anywhere, nor will it be before I turn in the final version of my ETD, so I didn't include a publication statement.

Authors:

P. Sudharshan Phani [1], K. E. Johanns [1], E. P. George [1,2], and G. M. Pharr [1,2]

[1] *Dept. of Materials Science and Engineering, University of Tennessee, Knoxville, TN 37996*
[2] *Materials Science and Technology Division, Oak Ridge National Laboratory, Oak Ridge, TN 37831*

P. Sudharshan Phani's involvement in the article: Developed the model and derived the equations, compared model predictions with experimental results, wrote and revised the article.

Co-researchers' contributions are listed as follows:

K.E. Johanns performed Monte Carlo simulations and assisted in model development and data analysis.

E.P. George provided inputs in model development and manuscript revision.

G.M. Pharr conceived the basic idea and worked with Phani and Johanns to develop the model, helped prepare and revise the article.

Abstract

A simple stochastic model is developed to determine the pop-in load and maximum shear stress at pop-in for nanoindentation experiments conducted with spherical indenters. The model incorporates two separate mechanisms: pop-in due to nucleation of dislocations in dislocation-free regions and pop-in due to the activation of pre-existing dislocations. Two different types of randomness are used to model the stochastic behavior including randomness in the spatial location of the dislocations beneath the indenter and randomness in the spatial orientation of the dislocations. In addition to correctly predicting the average maximum shear stress at pop-in and how it depends on indenter radius, the model also adequately describes the scatter in pop-in loads. Monte Carlo simulations are performed to validate the model and visualize the scatter expected in a limited number of tests. The model predictions are in close agreement with recent experimental observations of indenter size effects on pop-in in molybdenum single crystals.

1. Introduction

The physical origin of the popular notion that "smaller is stronger", i.e., that strength depends on size and increases at small scales, has long been a subject of debate. Recent advances in small-scale mechanical testing have provided great opportunities to explore the underlying mechanisms of these effects. One such example is micro-pillar compression testing, wherein the yield and flow behavior of micrometer and sub-micrometer test specimens has been examined extensively (Greer *et al.*, 2005; Hemker and Sharpe, 2007; Kiener *et al.*, 2008; Kiener *et al.*, 2006; Kraft *et al.*, 2010; Schneider *et al.*, 2009; Uchic and Dimiduk, 2005; Volkert and Lilleodden, 2006) and summarized by Uchic et al. (Uchic *et al.*, 2009).

Recently, Shim et al. (Shim *et al.*, 2008) demonstrated that size effects can also be observed in nanoindentation testing. Specifically, they found that the shear stress at which nanoindentation pop-in occurs in highly annealed single crystals of Ni tested with spherical indenters decreases with increasing indenter radius. Since the sudden displacement burst that characterizes nanoindentation pop-in represents the transition from elastic to plastic flow and is mechanistically caused by the nucleation of dislocations in dislocation-free regions or the activation of pre-existing dislocations, it is the indentation equivalent of yielding in pillar testing. In pillar testing of single phase materials, there are two important length scales: (1) the size of the pillar and (2) the average spacing of the dislocations they contain, and it is often when these two length scales are similar that the unusual size effects on strength become important. In addition to the size effect, one might expect the strength of small pillars to be very scattered and stochastic since the yield and flow behavior are controlled by only a small number of dislocations whose character, orientation, and mobility might vary significantly from one pillar to the next.

A similar effect would be expected in nanoindentation pop-in. As shown in Fig. 3.1, here again there are two important length scales: (1) the average spacing of dislocations λ_{avg} =

$\rho^{-0.5}$, where ρ is the dislocation density, and (2) the size of the highly stressed zone under the contact, which itself would scale with the radius of the indenter, R, as well as the indentation load, F, and the elastic modulus, E. As shown in Fig. 3.2a, recent nanoindentation pop-in experiments on single crystal molybdenum (Mo) by Morris et al. (Morris *et al.*, 2011) have shown a strong size effect with the maximum shear stress at pop-in transitioning with increasing indenter radius from a high level corresponding to the theoretical strength to a lower level corresponding to the bulk strength. In addition to the size effect on the average strength, a very large scatter in the shear stress at pop-in is observed for the intermediate radii. As shown in Fig. 3.2b, this behavior is analogous to recently reported tensile and compression tests on sub-micron diameter Mo-alloy fibers, in which compression experiments were performed on short pillars (1-3 μm in length) and micro-tension tests were performed on much longer fibers (10-30 μm long). As the figure shows, varying the normalized gauge length of the specimen, ℓ / λ_{avg} where ℓ is the gauge length and λ_{avg} is the average dislocation spacing, gives rise to a large size effect on the yield strength as well a large variability in the scatter in a manner very similar to the pop-in data in Fig. 3.2a. Even though nanoindentation data are more difficult to analyze because of the complex nature of the indentation stress fields, the nanoindentation pop-in experiments have a distinct advantage over the compression/tension tests because they are quick and easy to perform. Thus, a greater number of tests can be conducted at a single geometric length scale (i.e., indenter radius), which helps to better define and quantify the details of the observed scatter.

Sudharshan Phani et al. (Phani *et al.*) have recently developed a stochastic model for yielding in tensile or compression specimens with a limited number of dislocations. Based on a combination of nucleation of dislocations in dislocation-free regions and activation of pre-existing ones, the model adequately explains the size effects and scatter observed during the testing of the Mo-alloy fibers (Fig. 3.2b). Here, we take the physical principles underpinning that model and reformulate it to describe nanoindentation pop-in with spherical indenters. Most prior statistical models for nanoindentation pop-in have been based either on nucleation of dislocations (Ngan *et al.*, 2006; Schuh and Lund,

2004) or activation of pre-existing ones (Morris *et al.*, 2011) , but not both. In addition to explaining the size effect, the model also provides a way to estimate the scatter in the data and how it will vary with indenter radius.

2. Modeling approach

Fig. 3.3 shows a schematic of the proposed pop-in model. The two-dimensional model assumes that pop-in begins when the first dislocation is activated or nucleated, i.e., there is a burst of strain due to an avalanche of dislocation activity when the first dislocation begins to move and others are rapidly multiplied. In this regard, it is the motion of the easiest to move dislocation that controls the behavior, and the model is based on simple weak link concepts. The outer boundary of the highly stressed zone is chosen to correspond with the critical resolved shear stress (τ_{crss}), implying that all of the stresses inside the zone are greater than τ_{crss}. If the zone contains dislocations that can be activated, as on the right side of Fig. 3.3, i.e., $\tau > \tau_{act}$, (τ is the maximum principal shear stress and τ_{act} is the resolved shear needed to activate the dislocation), then pop-in occurs by activation of the dislocation that requires the lowest shear stress to move it. In this manuscript, τ will be used to denote the maximum principal shear stress as calculated by the methods given in Appendix 3.1. If the zone does not have any dislocations that are activated due to unfavorable orientation relative to the indentation stress field or there are no dislocations at all in the zone, as on the left side of Fig. 3.3, then pop-in occurs by homogeneous nucleation of dislocations when the theoretical strength (τ_{nuc}) is exceeded. Thus, the occurrence of pop-in is a random event that depends on the spatial distribution and activation of dislocations.

To mathematically develop this, we introduce two types of randomness, viz., randomness in the spatial location of dislocations and randomness in the orientation of the dislocations, where the latter results in randomness in the indentation stress needed to activate them. The randomness in spatial location, which determines the number of dislocations in the highly stressed zone, can be modeled by Poisson statistics (Phani *et* *al.*). The randomness in activation stress can be modeled by assuming that the dislocations are randomly orientated relative to the direction of the maximum indentation shear stress. In a more detailed analysis, one could also incorporate other sources of randomness that depend on the specific physics of other possible strengthening mechanisms, viz., dislocation source length variations, solute distributions, crystal orientation, etc. However, for the sake of simplicity, such effects are not considered here. The model can also be developed and implemented using Monte Carlo principles. A flow chart of the algorithm used for the Monte Carlo simulations is shown in Fig. 3.4. The Monte Carlo method helps not only to validate the analytical model but also to visualize the scatter that would be expected in a limited number of tests.

The model development follows closely along the lines of the stochastic model for uniaxial micro-pillar compression / tension testing presented recently by Sudharshan Phani et al. (Phani *et al.*). The primary assumptions of the model are:

(i) The dislocations are non-interacting.

(ii) The model is developed in two dimensions (2D), wherein the dislocations are modeled as straight line defects perpendicular to the cross section.

(iii) The model is athermal but could be easily extended to include thermally activated processes such as stress-assisted, thermally activated dislocation nucleation.

(iv) Pop-in occurs either due to the nucleation of dislocations at the theoretical strength or due to the motion of a pre-existing dislocation when the local resolved shear stress on the dislocation exceeds the activation stress τ_{crss}.

(v) The model assigns random orientations to model the activation of pre-existing dislocations. However, the general framework could be used to extend the model to other physical mechanisms such as random source lengths (Parthasarathy *et al.*, 2007), crystal orientation (Li *et al.*, 2011), etc.

(vi) The model applies to an elastically isotropic medium. Elastic anisotropy could be added at the expense of mathematical simplicity.

2.1 Generic framework for the model

The model is a simple extension of the model developed previously by Sudharshan Phani et al. (Phani *et al.*) for uniaxial micro-pillar compression testing and micro-fiber tension testing. In that model, the yield strength under uniaxial stress conditions for a random spacing and orientation of dislocations was determined. The inputs to the model are the dislocation density, ρ, the theoretical strength, τ_{nuc}, and the critical resolved shear stress, τ_{crss}. The model estimates the average yield strength through a weighted average of the probabilities of the various strengths, which in turn are calculated based on the length (in 1D) or cross sectional area (in 2D) of the specimens, the dislocation density (ρ), and the stress acting on the specimens. Due to the relatively simple specimen geometry for the uniaxial tests, the cross sectional area is constant and the stress acting on the specimen is uniform at a given load. However, neither of these applies to indentation testing.

In order to extend the model to indentation, where the stresses vary significantly from point to point beneath the contact, one needs to consider the stress distribution under a spherical indenter and use it to establish the area of the highly stressed zone as schematically shown in Fig. 3.5. Since pop-in represents the transition from elastic to elastic-plastic deformation during indentation, the stresses at pop-in in spherical indentation can be estimated from Hertzian elastic contact mechanics. The right hand side of Fig. 3.5 shows the contours of maximum principal shear stress in the highly stressed zone, estimated using the analytical solution for the elastic stress field under a spherical indenter (Fischer-Cripps, 2000; Huber, 1904). The equations for the various stress components are given in Appendix 3.1. Three representative contours are shown in the figure denoted by τ, τ_a and τ_b such that $\tau_b < \tau < \tau_a$, indicating that the stress field decays with distance from the indenter. The key geometric feature in the figure is the area enclosed within a specific maximum principal shear stress contour τ (shaded region) at an applied load F, i.e., the area inside of which the stresses are all greater than some critical value. Using Hertzian contact stresses and the dimensional analysis outlined in Appendix 3.2, this area is given by

$$A(F,\tau) = \frac{k}{\tau}\left(F - F_\tau\right), \tag{1a}$$

where, F_τ is the minimum load required to produce a maximum shear stress of τ given by the Hertzian expression shown in Eq. (A12) of Appendix 3.2, and k is a constant that depends on Poisson's ratio (ν). The value of the constant k can be obtained by fitting the numerically determined areas enclosed in the contours of maximum principal shear stresses for Hertzian elastic contact as a function of Poisson's ratio and is given by

$$k = 0.022\nu^2 - 0.0226\nu + 0.1245. \tag{1b}$$

In all further calculations, we will assume $\nu = 0.3$ which results in a value of 0.1194 for k.

Based on the area of the highly stressed zone in Fig. 3.5, the probability of pop-in at an applied load can be estimated by weak link principles as shown schematically in Fig. 3.6. For the dislocation arrangement shown there, which includes randomness in spatial location and spatial orientation, pop-in will occur by dislocation activation if at least one dislocation inside the highly stressed zone can be activated, i.e., the *resolved* shear stress at the location of the dislocation inside the zone is greater than the stress needed to activate it, τ_{crss}. Hence, the probability of pop-in at a given load depends not only on the probability of finding a dislocation inside the zone, but also on the probability p_{act} that the local resolved shear stress is sufficient to move it. Since the stress field inside the zone is not uniform, we discretize it into N small equal area elements, each having an area dA (see Fig. 3.6) given by

$$dA = \frac{A\left(F, \tau_{crss}\right)}{N}, \tag{2}$$

where, $A(F,\tau_{crss})$ is the area enclosed within the maximum principal shear stress contour of τ_{crss} at a load F obtained by substituting $\tau = \tau_{crss}$ into Eq. (1a). Let j denote an integer incremental variable that varies from 1 to N and is used to increment the areas inside the τ_{crss} contour from dA to $A(F,\tau_{crss})$. When $j = N$, $\tau = \tau_{crss}$ and the enclosed area inside the τ_{crss} contour is equal to $A(F,\tau_{crss})$. The probability of activating at least one dislocation within the infinitesimal area element dA can then be integrated inside the zone up to the boundary (which has an area $A(F,\tau_{crss})$) to estimate the probability of pop-in at a given load F. Following the procedure outlined in Appendix 3.3, this gives

$$p(F) = 1 - \exp\left(-\rho dA \lim_{N \to \infty} \sum_{j=1}^{N} p_{act} \right), \tag{3}$$

which provides the generic framework needed to estimate the probability of pop-in for any type of probability distribution for dislocation activation, p_{act}.

To this point, the discussion has been limited to pop-in by activation of pre-existing dislocations. However, if pop-in does not occur up to a load F_{nuc} at which a maximum shear stress equal to the theoretical strength is generated, then pop-in will occur by the nucleation of dislocations. Considering that pop-in may take place by either process, the average pop-in load can be estimated as a weighted average of the pop-in probabilities at various loads (Eq. (3)). This gives

$$F_{avg} = F_{nuc}\left(1 - \int_{F_{crss}}^{F_{nuc}} dp \right) + \int_{F_{crss}}^{F_{nuc}} F dp, \tag{4}$$

where the first term corresponds to pop-in by dislocation nucleation and the second term to activation of a pre-existing dislocation. In this equation, F_{nuc} and F_{crss} are calculated by substituting τ_{nuc} and τ_{crss} into Eq. (A12) of Appendix 3.2, respectively.

The generic framework developed here can be applied to different situations for the required activation stress by estimating the corresponding probability of activation p_{act}. In this work, we focus on two such cases. In case 1, all the dislocations are assumed to be favorably oriented relative to the direction of maximum principal shear stress so that randomness in dislocation orientation is not a factor, and only the randomness in spatial location is important. In case 2, the dislocations are assumed to be both randomly located and randomly oriented so that both factors play a role. Although the latter case is more realistic, much of the more important controlling physics is embodied in the former, which is also easier to develop in closed mathematical form.

2.2 Case 1: All dislocations are favorably oriented relative to the maximum principal shear stress

Fig. 3.7 shows a schematic representation of case 1, wherein all the dislocations are shown as points with the dislocation line normal to the cross section. Under the condition that all the dislocations are favorably oriented relative to the direction of maximum principal shear stress, any dislocation inside the zone will be activated since $\tau_{act} = \tau_{crss}$; that is, τ inside the zone is always greater than τ_{crss} and hence the probability of activation $p_{act} = 1$. Substituting a value of 1 for p_{act} in Eq. (3), the average pop-in load (F_{avg}) can be determined in a closed form using Eq. (4) and is given by

$$F_{avg} = F_{crss} + \frac{\tau_{crss}}{\rho k}\left\{1 - \exp\left[-\frac{\rho k}{\tau_{crss}}\left(F_{nuc} - F_{crss}\right)\right]\right\}, \tag{5}$$

where, F_{crss} and F_{nuc} are calculated as explained earlier. The average load can now be substituted into the Hertzian expression for τ_{max}

$$\tau_{\max} = 0.31\left(\frac{6FE_r^2}{\pi^3 R^2}\right)^{\frac{1}{3}}, \tag{6}$$

to give the average maximum shear stress at pop-in (Shim *et al.*, 2008). The value of τ_{max} computed in this way is then a measure of the stress needed to initiate dislocation plasticity. Note that for the limiting cases of low ($\rho \to 0$) and high ($\rho \to \infty$) dislocation density, the model correctly predicts the maximum shear stress at pop-in as τ_{nuc} and τ_{crss}, respectively. Fig. 3.8 shows a comparison of the average maximum shear stress at pop-in determined by the model along with 20000 Monte Carlo simulations using E =100 GPa, τ_{nuc} = 10 GPa and τ_{crss} = 1 GPa. With increasing indenter radius, the maximum shear stress at pop-in transitions from a high strength level (τ_{nuc}) to a lower strength level (τ_{crss}), which is precisely the size effect observed in spherical indentation by Shim et al. (Shim *et al.*, 2008). The plot also shows that the transition moves from left to right with decreasing dislocation density, as would be expected based on the interplay of the two important length scales in the problem - the indenter radius, R, and the average spacing of dislocations, $\rho^{-0.5}$. The good agreement between the model predictions and the Monte Carlo results confirms the utility of Eq. (5).

2.3 Case 2: Dislocations are randomly oriented relative to the direction of maximum principal shear stress

The geometry for case 2 is shown in Fig. 3.9, wherein the dislocations are oriented at random angles with respect to the direction of the maximum principal shear stress (τ). To define this orientation, we let the dislocation be rotated through an angle α (α is a random angle between 0 and 360^0) with respect to the r-axis of the specimen and the direction of the maximum principal shear stress be at an angle θ relative to the r-axis of the specimen (see Fig. 3.9a). For the dislocation to be activated, the resolved shear stress acting in the direction of motion of the dislocation on its glide plane should be greater than τ_{crss}. This resolved shear stress is given by (Dieter, 1976)

$$\tau_{res} = \tau_j \cos 2(\theta - \alpha), \tag{7}$$

where τ_j is the magnitude of the maximum principal shear stress in the infinitesimal area element *dA* shown on the left hand side of Fig. 3.9a.

Fig. 3.9b shows the distribution of the angles of maximum principal shear stress (θ) along the contours of maximum principal shear stress for Hertzian elastic contact, from which it follows that θ generally varies from 0 to 45^0 and from 65 to 90^0. If we assume a random distribution of angles within the specified range, then $(\theta - \alpha)$ should be a random angle between -90^0 and 360^0. For the dislocation to be activated, the resolved shear stress τ_{res} must be greater than τ_{crss}, and the probability of such an event is

$$p_{act} = \frac{2}{\pi} \cos^{-1}\left(\frac{\tau_{crss}}{\tau_j}\right). \tag{8}$$

Substituting the above into Eq, (3), we obtain the probability of pop-in that can be used to calculate the average pop-in load (F_{avg}) using Eq. (4). However, unlike case 1, the average pop-in load cannot be written in a closed form but must be computed numerically from the governing equations.

Fig. 3.10 shows the average maximum shear stress at pop-in for case 2 determined by the model and 20000 Monte Carlo trials using E =100 GPa, τ_{nuc} = 10 GPa and τ_{crss} = 1 GPa. Similar to case 1 (Fig. 3.8), there is near perfect agreement between the model and the Monte Carlo results, with the shear stress transitioning from a higher strength level (τ_{nuc}) to a lower strength level (τ_{crss}) with increasing indenter radius. The figure also shows the model results for case 1 for comparison. It is interesting to note that the model predictions for case 2 are in fact very close to those for case 1, implying that most of the stochastic behavior is embodied in the randomness in spatial location alone. Thus, the simple closed form of Eq. (5) is a reasonable first order estimate of the expected behavior.

2.4 Scatter in the maximum shear stress at pop-in

One can also use the approach developed here to estimate the amount of scatter that would be expected in the data and how it varies with material and geometric parameters. To this end, we estimate the scatter in maximum shear stress at pop-in using the approach developed previously by Sudharshan Phani et al (Phani *et al.*) for uniaxial tension / compression. As in the previous work, we model the scatter bounds by the limiting maximum shear stress values within which a given percentage of the maximum shear stresses lie. For example, 90 % scatter bounds (the bounds that will be used this paper), would exclude the top and bottom 5% of the maximum shear stresses but include the middle 90% of the stresses. Details on how these scatter bounds can be calculated are given elsewhere (Phani *et al.*).

Fig. 3.11a shows the 90 % scatter bounds for maximum shear stress at pop-in predicted by the model (case 1) using E =100 GPa, τ_{nuc} = 10 GPa and τ_{crss} = 1 GPa. Results of 100 Monte Carlo trials at several discrete indenter radii are also shown for comparison. It is evident from the plot that the model accurately captures the scatter bounds predicted by the Monte Carlo calculations. In addition, similar to the results for average maximum shear stress at pop-in shown in Fig. 3.10, Fig. 3.11b shows that the scatter bounds for case 1 and case 2 are also very close, with the results for case 2 slightly shifted to the right of case 1. Similar to the trend observed in uniaxial testing, the scatter is minimal at the extremes of the length scale while it is large at intermediate values. However, unlike the model for uniaxial testing of small fibers, the scatter in the transition regime is not so concentrated at the extreme values. Thus, the complexity of the spatial stress variation under the indenter tends to produce data for which the scatter behaves in a more usual way.

3. Comparison with experimental results

Lastly, we compare the maximum shear stress at pop-in predicted by the model to the experimental pop-in data for molybdenum single crystals reported by Morris et al. (Morris *et al.*, 2011). The inputs to the model are the theoretical strength (τ_{nuc}), the critical resolved shear stress (τ_{crss}), the dislocation density (ρ) and the elastic modulus (E). All material inputs were those used by Morris et al. (Morris *et al.*, 2011), with the exception of the dislocation density, where $\rho = 10^{11}$ m^{-2} was assumed based on the recent x-ray line broadening measurements for this material referred by Morris et al. (Morris *et al.*, 2011). Since the model does not consider scatter in the theoretical strength (this could be added by considering nucleation to be a stress-assisted, thermally activated process), an average value (15.9 GPa) for the maximum shear stress at pop-in for the smallest radius was taken as the theoretical stress (τ_{nuc}), while the smallest shear stress value in the data set (0.4 GPa) was taken as τ_{crss}. The polycrystalline average elastic modulus and Poisson's ratio for molybdenum are 327 GPa and 0.3, respectively.

Fig. 3.12 shows a comparison of the experimental data and the model predictions (case 1) plotted as the cumulative probability of the maximum shear stress at pop-in for the different indenter radii. The indenter radius (in μm) is shown beside the corresponding curve. Excellent agreement between the model predictions and the experimental data is seen for the wide range of indenter radii. It is also worth noting that the current model closely follows the experimental data even at very small indenter radii, unlike the model presented by Morris et al. (Morris *et al.*, 2011), wherein pop-in due to nucleation of dislocations was not considered.

Fig. 3.13 shows the experimental data along with the 90% scatter bounds predicted by the model (case 1). The plot shows that the model accurately captures the range of scatter for the wide range of indenter radii used in the experiments. From these observations, it is clear that the current approach can be used to reconcile the experimentally observed size effect in maximum shear stress at pop-in from a purely statistical point of view.

4. Summary and conclusions

A weak link statistical model has been developed to predict the pop-in loads and maximum shear stress at pop-in as a function of indenter radius. The model considers pop-in not only due to the nucleation of dislocations but also the activation of pre-existing dislocations. The model predicts a transition in the maximum shear stress at pop-in from a higher strength level (τ_{nuc}) to a lower strength level (τ_{crss}) with increasing indenter radius, thus explaining recently reported experimental observations for Ni & Mo single crystals. The model also accurately captures the scatter in the Mo single crystal data. These results closely follow the "size effect" trends observed in micro-pillar testing. In combination, these results point toward the important role played by statistics in the mechanical behavior of materials at small length scales.

Acknowledgements

This work was supported by the US Department of Energy, Office of Basic Energy Sciences, Materials Sciences and Engineering Division.

References

Dieter, G. E. 1976. ***Mechanical metallurgy***: McGraw-Hill.

Fischer-Cripps, A. C. 2000. ***Introduction to Contact Mechanics***: Springer.

Greer, J. R., Oliver, W. C., & Nix, W. D. 2005. Size dependence of mechanical properties of gold at the micron scale in the absence of strain gradients. ***Acta Mater***, 53(6): 1821-1830.

Hemker, K. J., & Sharpe, W. N. 2007. Microscale characterization of mechanical properties. ***Annu Rev Mater Res***, 37: 93-126.

Huber, M. T. 1904. Zur Theorie der Berührung fester elastischer Körper. ***Annalen der Physik***, 319(6): 153-163.

Kiener, D., Grosinger, W., Dehm, G., & Pippan, R. 2008. A further step towards an understanding of size-dependent crystal plasticity: In situ tension experiments of miniaturized single-crystal copper samples. ***Acta Mater***, 56(3): 580-592.

Kiener, D., Motz, C., Schoberl, T., Jenko, M., & Dehm, G. 2006. Determination of mechanical properties of copper at the micron scale. ***Adv. Eng. Mater.***, 8(11): 1119-1125.

Kraft, O., Gruber, P. A., Monig, R., & Weygand, D. 2010. Plasticity in Confined Dimensions. ***Annu Rev Mater Res***, 40: 293-317.

Li, T. L., Gao, Y. F., Bei, H., & George, E. P. 2011. Indentation Schmid factor and orientation dependence of nanoindentation pop-in behavior of NiAl single crystals. ***J. Mech. Phys. Solids***, 59(6): 1147-1162.

Morris, J. R., Bei, H., Pharr, G. M., & George, E. P. 2011. Size Effects and Stochastic Behavior of Nanoindentation Pop In. ***Phys Rev Lett***, 106(16).

Ngan, A. H. W., Zuo, L., & Wo, P. C. 2006. Size dependence and stochastic nature of yield strength of micron-sized crystals: A case study on Ni3Al. ***Proc R Soc London A***, 462(2070): 1661-1681.

Parthasarathy, T. A., Rao, S. I., Dimiduk, D. M., Uchic, M. D., & Trinkle, D. R. 2007. Contribution to size effect of yield strength from the stochastics of dislocation source lengths in finite samples. ***Scripta Mater***, 56(4): 313-316.

Phani, P. S., Johanns, K. E., George, E. P., & Pharr, G. M. A simple stochastic model for yielding in specimens with limited number of dislocations. ***Acta Mater***, under review.

Schneider, A. S., Clark, B. G., Frick, C. P., Gruber, P. A., & Arzt, E. 2009. Effect of orientation and loading rate on compression behavior of small-scale Mo pillars. ***Mater. Sci. Eng., A***, 508(1-2): 241-246.

Schuh, C. A., & Lund, A. C. 2004. Application of nucleation theory to the rate dependence of incipient plasticity during nanoindentation. ***J Mater Res***, 19(7): 2152-2158.

Shim, S., Bei, H., George, E. P., & Pharr, G. M. 2008. A different type of indentation size effect. ***Scripta Mater***, 59(10): 1095-1098.

Uchic, M. D., & Dimiduk, D. A. 2005. A methodology to investigate size scale effects in crystalline plasticity using uniaxial compression testing. ***Mater. Sci. Eng., A***, 400: 268-278.

Uchic, M. D., Shade, P. A., & Dimiduk, D. M. 2009. Plasticity of Micrometer-Scale Single Crystals in Compression. ***Annu Rev Mater Res***, 39: 361-386.

Volkert, C. A., & Lilleodden, E. T. 2006. Size effects in the deformation of sub-micron Au columns. ***Philos. Mag.***, 86(33-35): 5567-5579.

Appendix 3.1.

Elastic stress field under a spherical indenter at an applied load *F*

The stress components in cylindrical coordinate system (r,θ,z) for an indenter of radius, R and contact radius, a, are given by (Huber, 1904; Fischer-Cripps, 2000):

$$\sigma_r = \sigma_{\max}\left\{\frac{1-2\upsilon}{3}\frac{a^2}{r^2}\left(1-\left(\frac{z}{\sqrt{u}}\right)^3\right)+\left(\frac{z}{\sqrt{u}}\right)^3\frac{a^2u}{u^2+a^2z^2}\right.$$
$$\left.+\frac{z}{\sqrt{u}}\left[u\frac{1-\upsilon}{a^2+u}+(1+\upsilon)\frac{\sqrt{u}}{a}\tan^{-1}\frac{a}{\sqrt{u}}-2\right]\right\} \tag{A1}$$

$$\sigma_z = -\sigma_{\max}\left(\frac{z}{\sqrt{u}}\right)^3\frac{a^2u}{u^2+a^2z^2} \tag{A2}$$

$$\tau_{rz} = -\sigma_{\max}\left(\frac{rz^2}{u^2+a^2z^2}\right)\left(\frac{a^2\sqrt{u}}{a^2+u}\right) \tag{A3}$$

where, $u = \frac{1}{2}\left\{\left(r^2+z^2-a^2\right)+\left[\left(r^2+z^2-a^2\right)^2+4a^2z^2\right]^{1/2}\right\}$.

Other important relations are:

$$\sigma_{\max} = \frac{3F}{2\pi a^2}, \text{ where } a = \left(\frac{3FR}{4E_r}\right)^{\frac{1}{3}} \text{ and } \frac{1}{E_r} = \frac{1-\nu^2}{E}+\frac{1-\nu_i^2}{E_i},$$

where E_i and E are the moduli of the indenter and specimen, respectively and, ν_i and ν are the Poisson's ratios for the indenter and the specimen.

The maximum principal shear stress (τ) and the corresponding angle (θ) it makes with the r-axis (see Fig. 3.9a) can be calculated from the above equations using the Mohr's circle concepts. These are given by (Dieter, 1976):

$$\tau = \frac{\sigma_1-\sigma_3}{2}, \tag{A4}$$

where, $\sigma_{1,3} = \frac{\sigma_r+\sigma_z}{2} \pm \left[\left(\frac{\sigma_r-\sigma_z}{2}\right)^2+\tau_{rz}^2\right]^{1/2}$ and

$$\theta = \frac{\pi}{4} + \frac{1}{2}\tan^{-1}\frac{\sigma_r - \sigma_z}{2\tau_{rz}}. \tag{A5}$$

Appendix 3.2.

Area enclosed within a maximum principal shear stress contour

The area enclosed within a maximum principal shear stress contour, τ, as schematically shown by the shaded region in Fig. 3.5 can be determined by dimensional analysis. Let the spatial coordinates be non-dimensionalized by the contact radius, a, and the stress components by the elastic modulus, E, such that

$$\bar{r} = r/a \text{ and } \bar{z} = z/a. \tag{A6}$$

The enclosed area (A) within a maximum principal shear stress contour can be non-dimensionalized as

$$\bar{A} = A/a^2. \tag{A7}$$

The stress components shown in Appendix 3.1 can now be re-written in non-dimensional form as:

$$\overline{\sigma_r}, \overline{\sigma_z}, \overline{\tau_{rz}}, \bar{\tau} = \frac{\sigma_{\max}}{E} f\left(\bar{r}, \bar{z}, \nu\right). \tag{A.8}$$

$$\text{Hence, } \bar{\tau} \propto \frac{\sigma_{\max}}{E} \propto \frac{F}{\pi E a^2}. \tag{A9}$$

From Eq. (A7) and Eq. (A9), the maximum principal shear stress can be written as

$$\bar{\tau} \propto \frac{F}{\pi E A} \text{ or } \tau \propto \frac{F}{\pi A}. \tag{A10}$$

Hence, for a maximum principal shear stress contour of τ (see Fig. 3.5), the enclosed area can be written as

$$\tau = k\frac{F - F_\tau}{A} \text{ or } A\left(F, \tau\right) = k\frac{F - F_\tau}{\tau}, \tag{A11}$$

where, k is the proportionality constant that is a function of Poisson's ratio ν, and F_τ is the minimum load required to generate a maximum shear stress of τ in the specimen. The value of F_τ can be determined from Hertzian elastic contact theory through the relation:

$$F_\tau = \frac{1}{6}\left(\frac{\pi}{0.31}\right)^3 \left(\frac{R}{E_r}\right)^2 \tau^3. \tag{A12}$$

Appendix 3.3.

Probability of pop-in due to activation of pre-existing dislocations

In the weak link model proposed (see Fig. 3.6), pop-in occurs by activation of dislocations at a load F if at least one dislocation is activated within the τ_{crss} contour. Let the specimen have n dislocations randomly oriented and spaced. The probability of at least one dislocation being activated is 1 minus the probability of none of the dislocations being activated. For the dislocations not to be activated within the τ_{crss} contour, either there should be no dislocations within the contour or the shear stress acting on the dislocations is lower than the activation stress. This can be written as

$$p(F) = 1 - [p(no\ dislos.\ within\ \tau_{CRSS}\ contour) \\ + \forall dislos.\ within\ \tau_{CRSS}\ contour : p(\tau_j < \tau_{act})]. \tag{A13}$$

Note that for a given dislocation

$$p(\tau_j < \tau_{act}) = 1 - p_{act}, \tag{A14}$$

where p_{act} is the probability of activation.

In order to calculate the probability of no dislocations being activated within the τ_{crss} contour, the area under the τ_{crss} contour can be discretized into N smaller equal area elements of area dA (see Fig. 3.6). The probabilities of no dislocations being activated within each area element can then be multiplied to obtain the probability of no dislocations being activated within the entire τ_{crss} contour.

For a specimen having n dislocations ($n \rightarrow \infty$) with a dislocation density ρ, the probability of finding i dislocations within an area dA is given by (Phani *et al.*)

$$p(i) = e^{-\rho dA} \frac{(\rho dA)^i}{(i)!}. \tag{A15}$$

Hence, the probability of no dislocations within an area dA is

$$p(0) = e^{-\rho dA}. \tag{A16}$$

The probability that all the dislocations within the infinitesimal area elements dA are not activated can then be written as

$$\forall dislos\ in\ \tau_{CRSS}\ contour : p(\tau_j < \tau_{act}) = \lim_{n\to\infty} \sum_{i=1}^{n} p(i)(1 - p_{act})^i. \tag{A17}$$

Substituting Eq. (A16) and (A17) in Eq. (A13) and multiplying the probabilities of all the area elements (1 to *N*), we obtain

$$p(F) = 1 - \lim_{N\to\infty} \prod_{j=1}^{N} \left[e^{-\rho dA} + \lim_{n\to\infty} \sum_{i=1}^{n} e^{-\rho dA} \frac{(\rho dA)^i}{(i)!} (1 - p_{act})^i \right]. \tag{A18}$$

The above equation can be simplified to

$$p(F) = 1 - \exp\left(-\rho dA \lim_{N\to\infty} \sum_{j=1}^{N} p_{act} \right). \tag{A19}$$

Appendix 3.4.

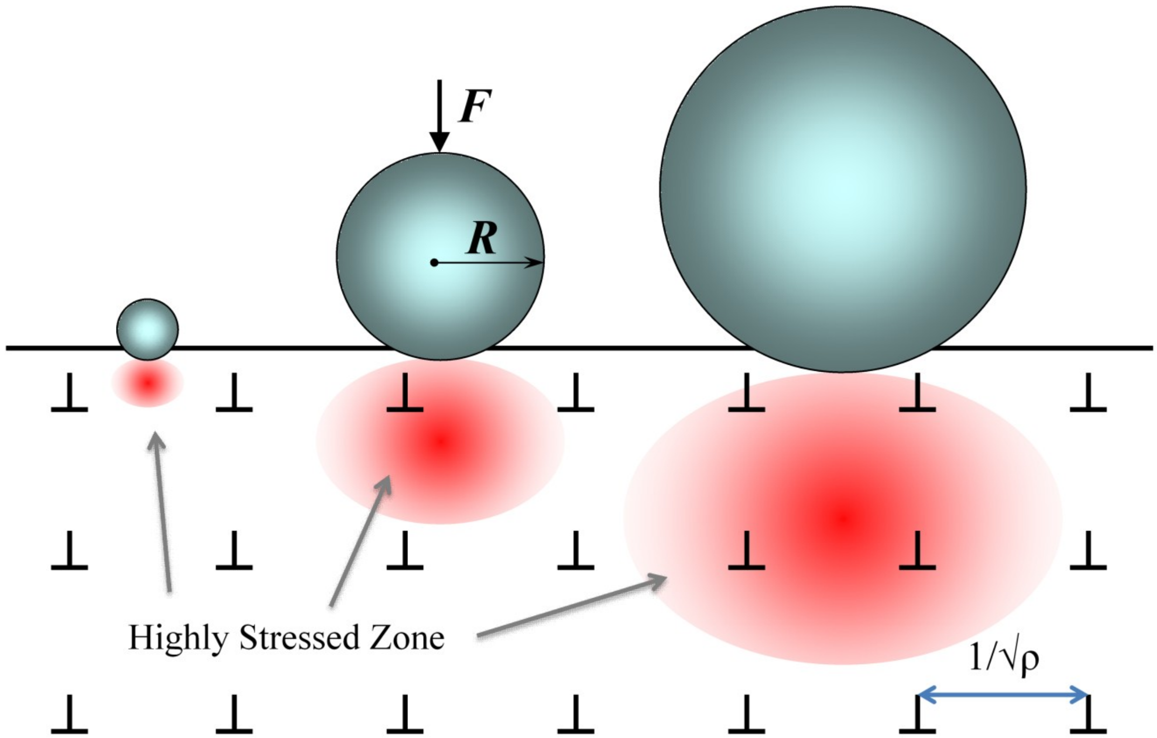

Figure 3.1. Schematic representation showing the length scales associated with spherical indentation pop-in. The geometric length scale is the radius of the spherical indenter or the size of the highly stressed zone. The material length scale is the average dislocation spacing.

(a)

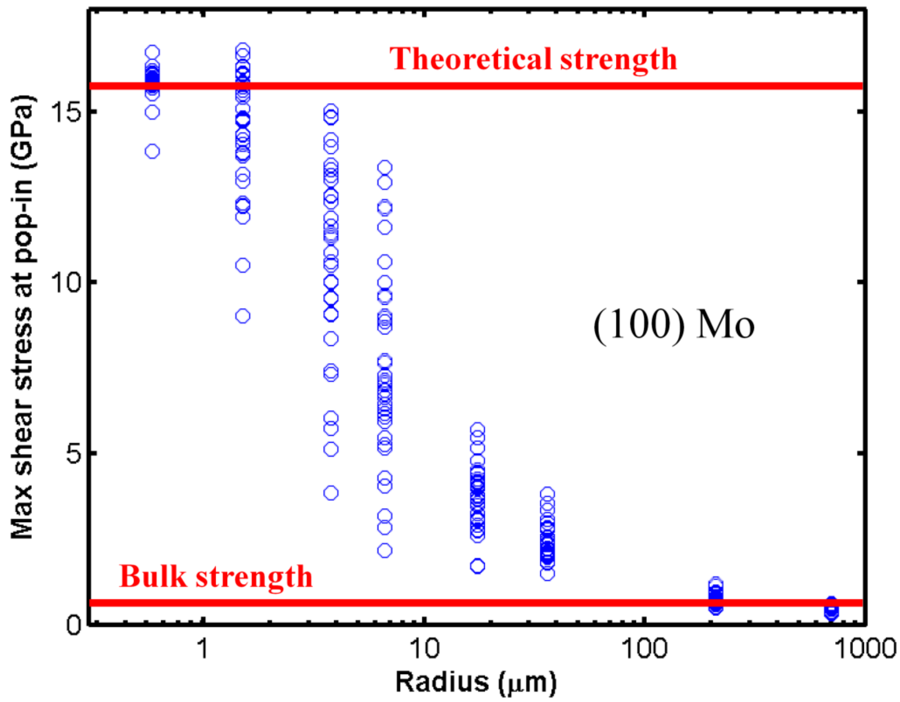

(b)

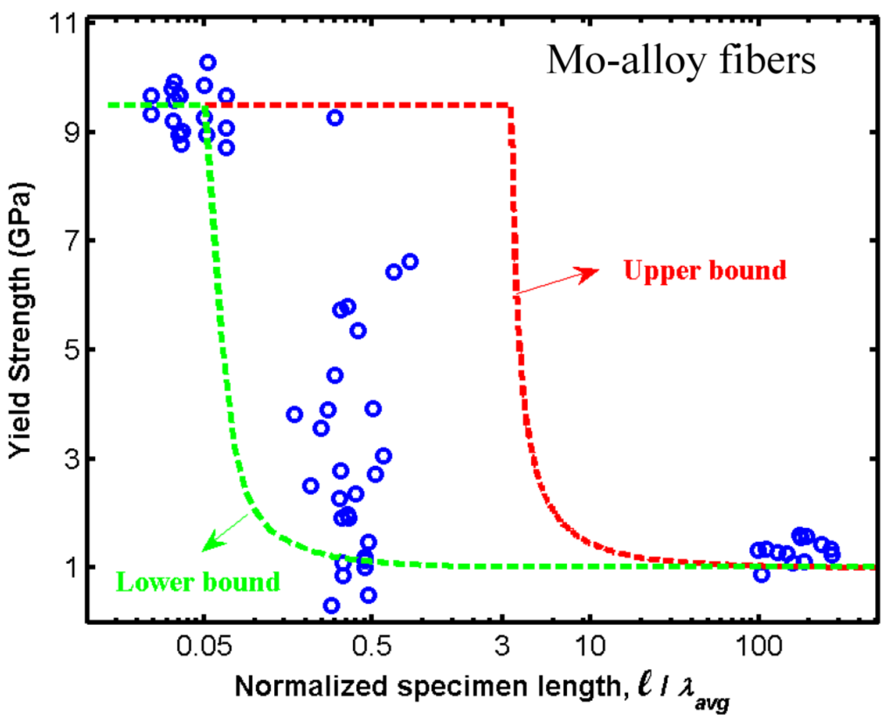

Figure 3.2. Size effects on strength: (a) influences of the indenter radius on the pop-in load during spherical nanoindentation (Morris *et al*., 2011); and (b) the dependence of the yield strength on normalized specimen length for uniaxial compression and tensile testing of small diameter (~400 nm) Mo-alloy fibers (Phani *et al*.).

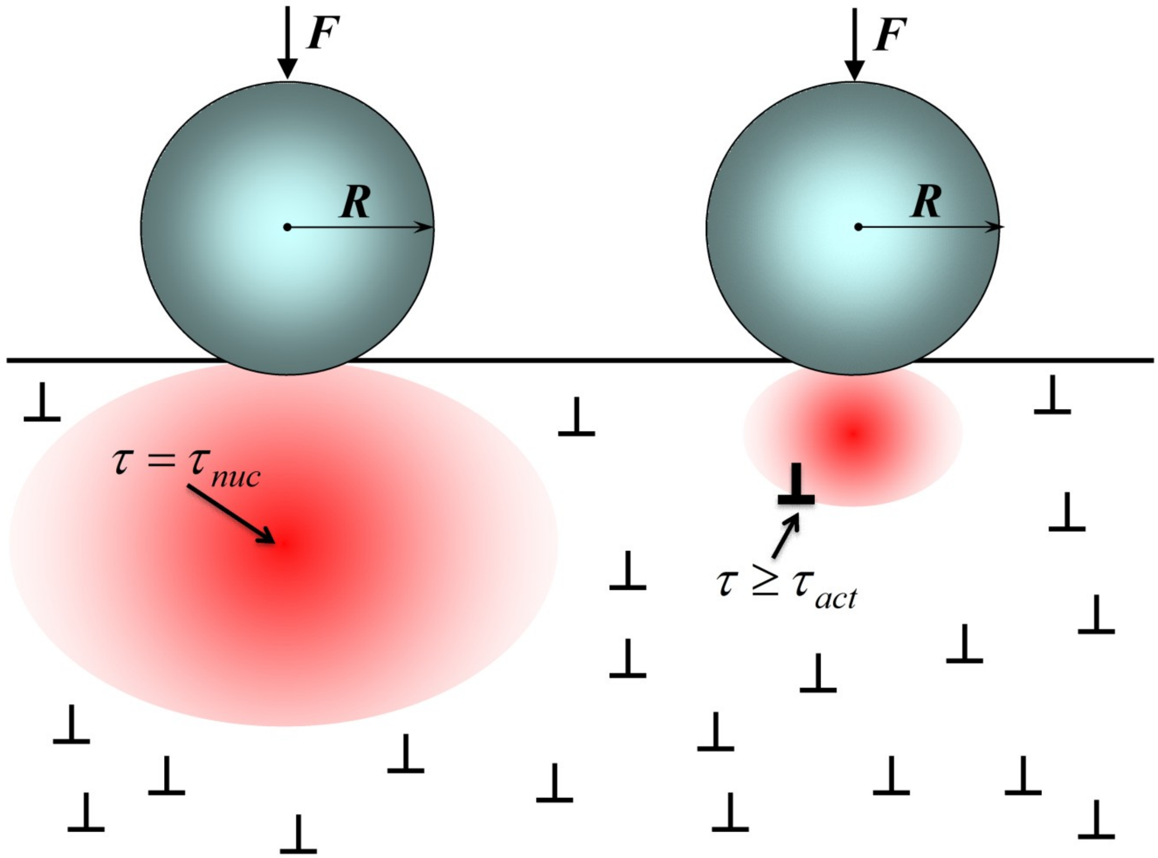

Figure 3.3. Schematic of the proposed model showing pop-in due to nucleation of dislocations in a region where the dislocation density is low (left) and activation of pre-existing dislocations in a region where the dislocation density is relatively high (right).

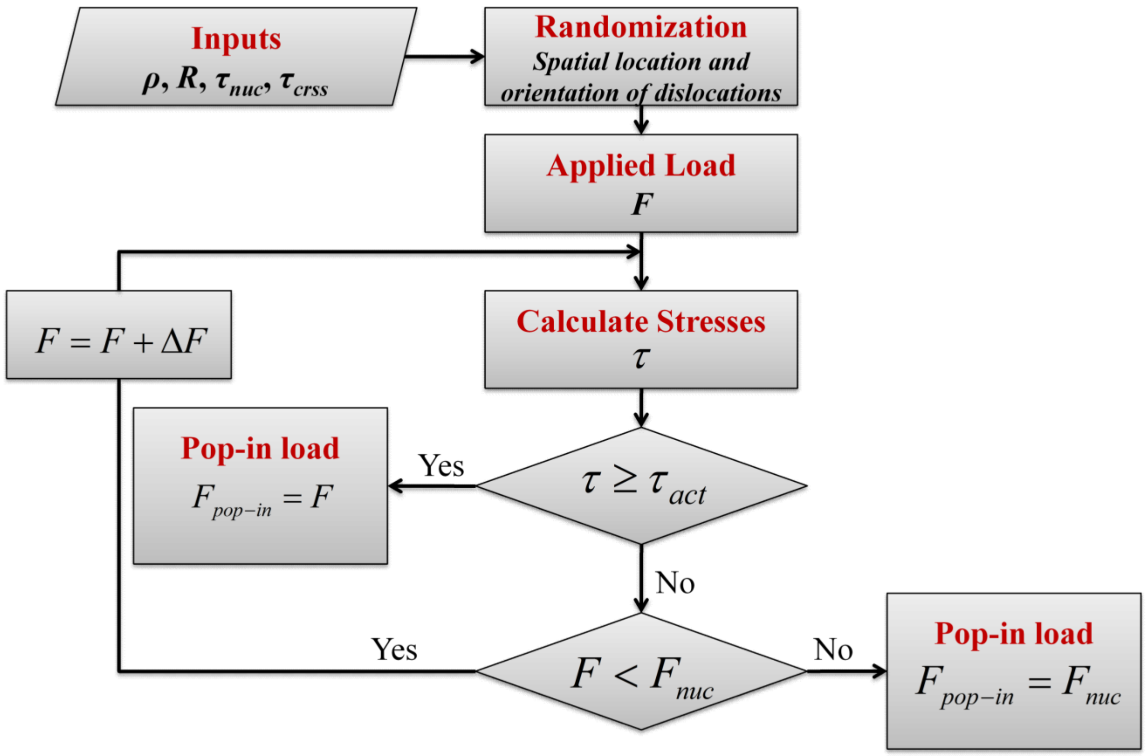

Figure 3.4. Flow chart showing the algorithm used for Monte Carlo simulations. F_{nuc} is the minimum load required to produce a maximum shear stress of τ_{nuc} given by the Hertzian expression shown in Eq. (A12) of Appendix 3.2.

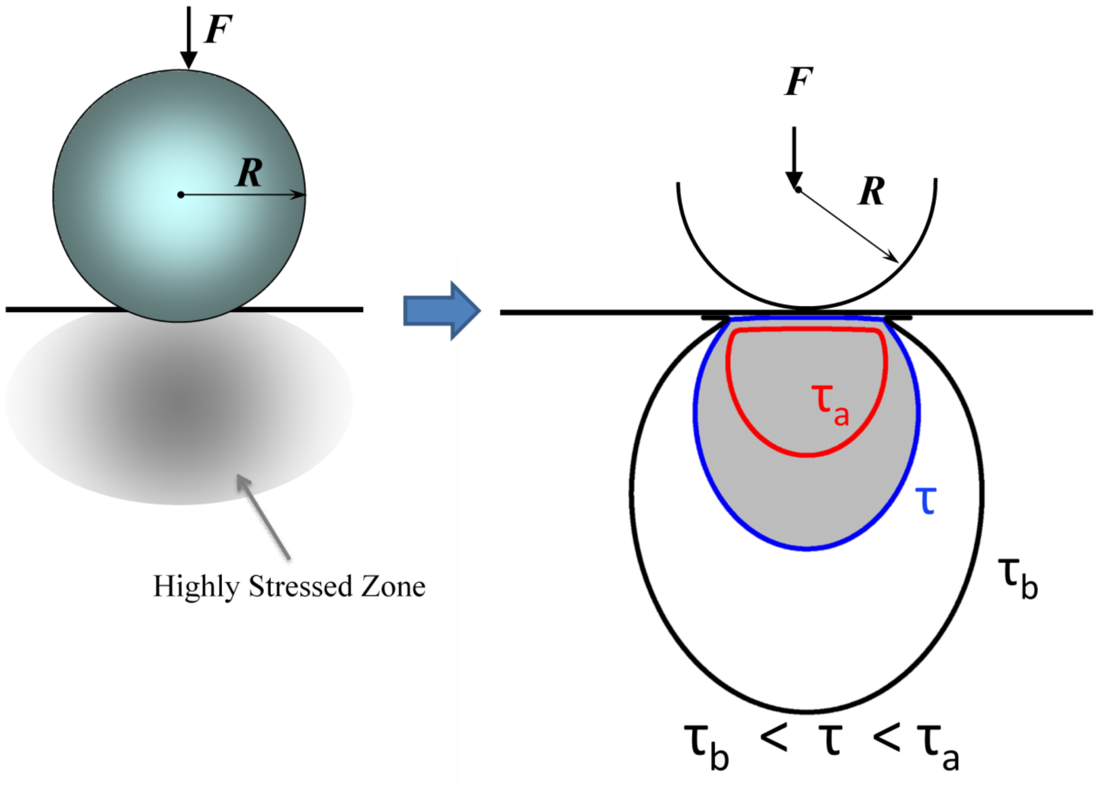

Figure 3.5. Schematic representation of the stress distribution in the highly stressed zone with three representative maximum principal shear stress contours (τ, τ_a and τ_b). The area within the contour of maximum principal shear stress of τ is shown as the shaded region on the right hand side of the figure.

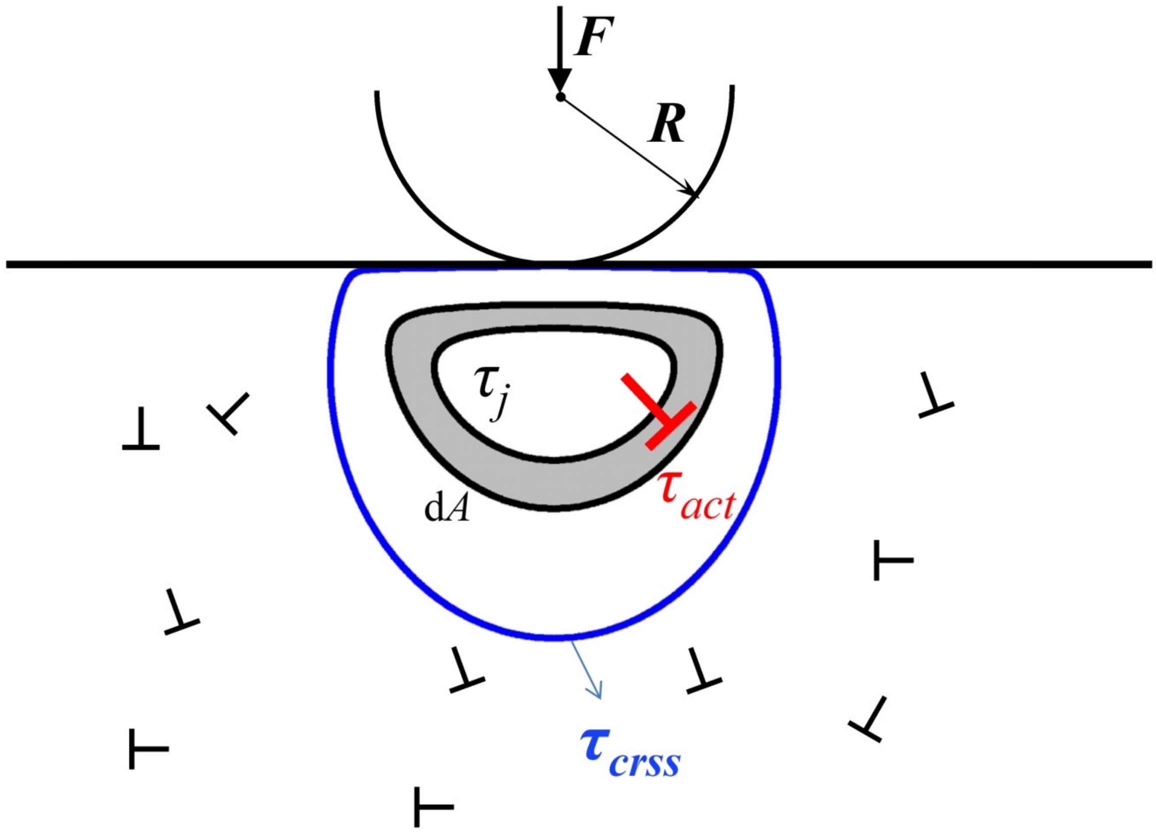

Figure 3.6. Schematic of contours of maximum principal shear stress and the differential area element used in the stochastic model.

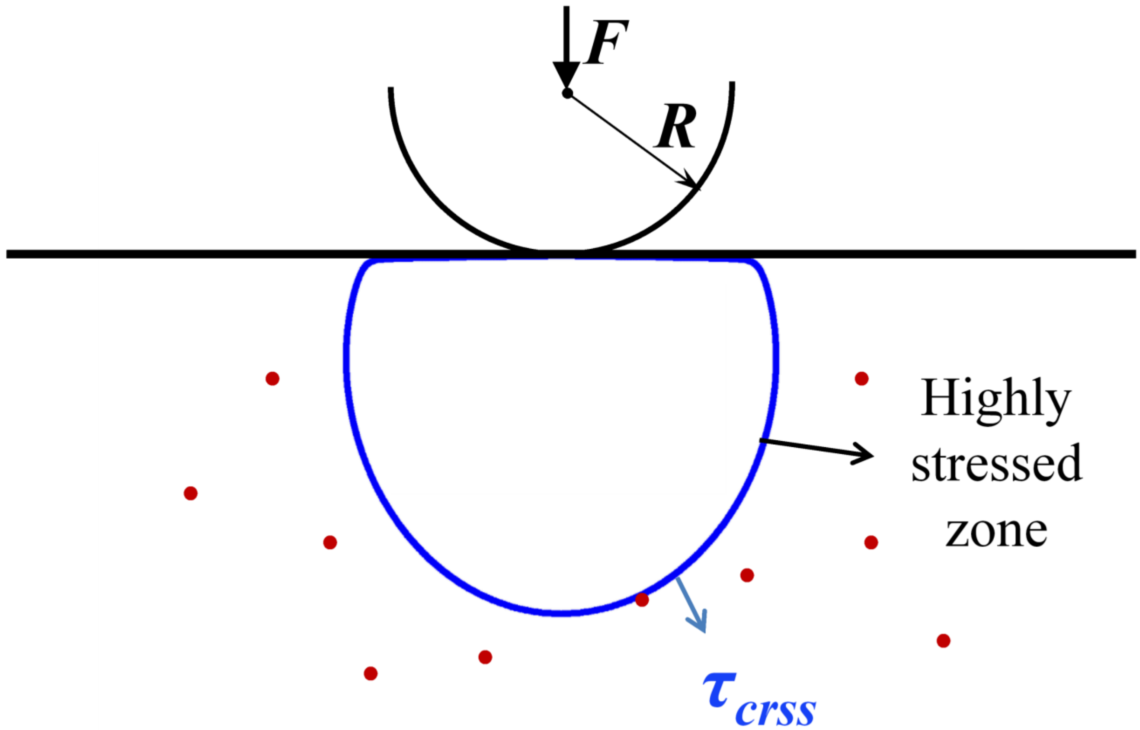

Figure 3.7. Schematic of randomly located dislocations (points), all favorably oriented relative to the direction of maximum principal shear stress (case 1). Pop-in occurs when the highly stressed zone grows to the point that it first contacts any dislocation.

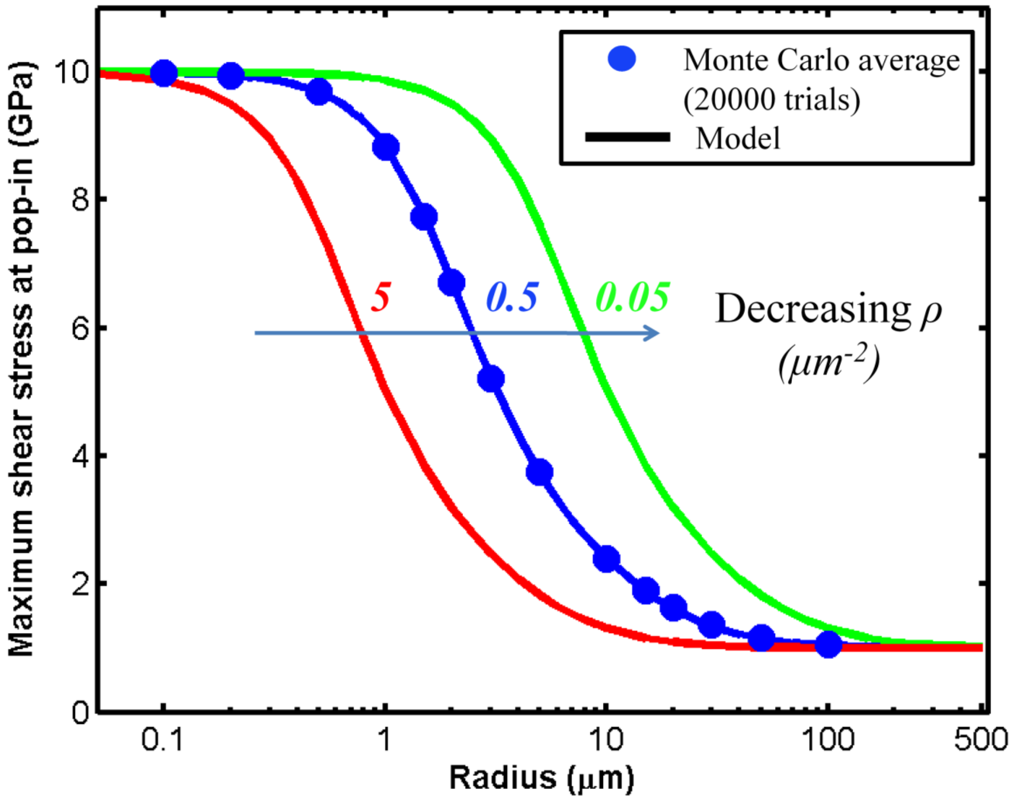

Figure 3.8. Comparison of model predictions (solid lines) and Monte Carlo results for case 1 along with model predictions for various dislocation densities.

(a)

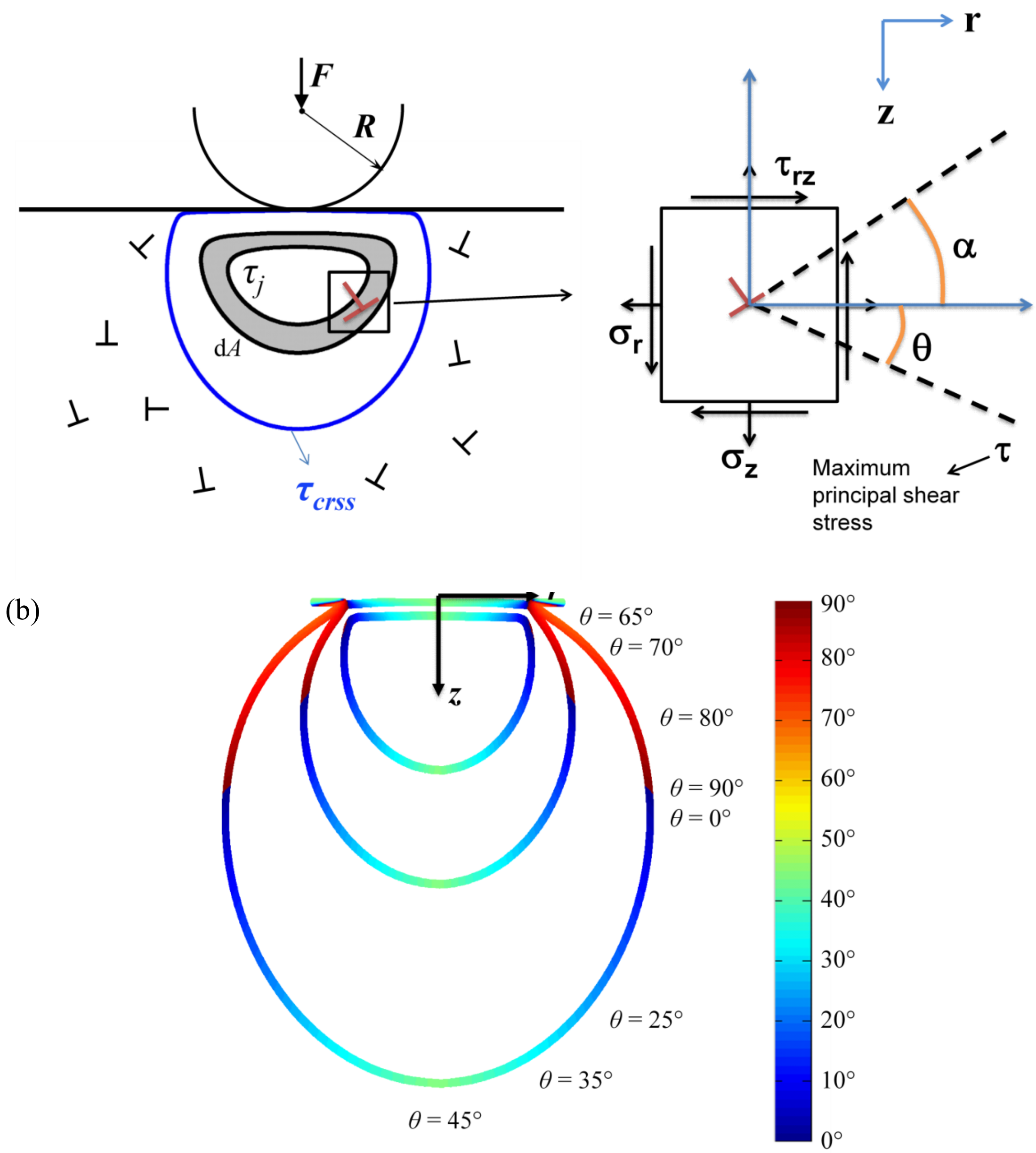

Figure 3.9. (a) Schematic of a random orientation of dislocations relative to the direction of maximum principal shear stress; and (b) the distribution of the angle of the maximum principal shear stress (θ) relative to the r-axis along contours of maximum principal shear stress.

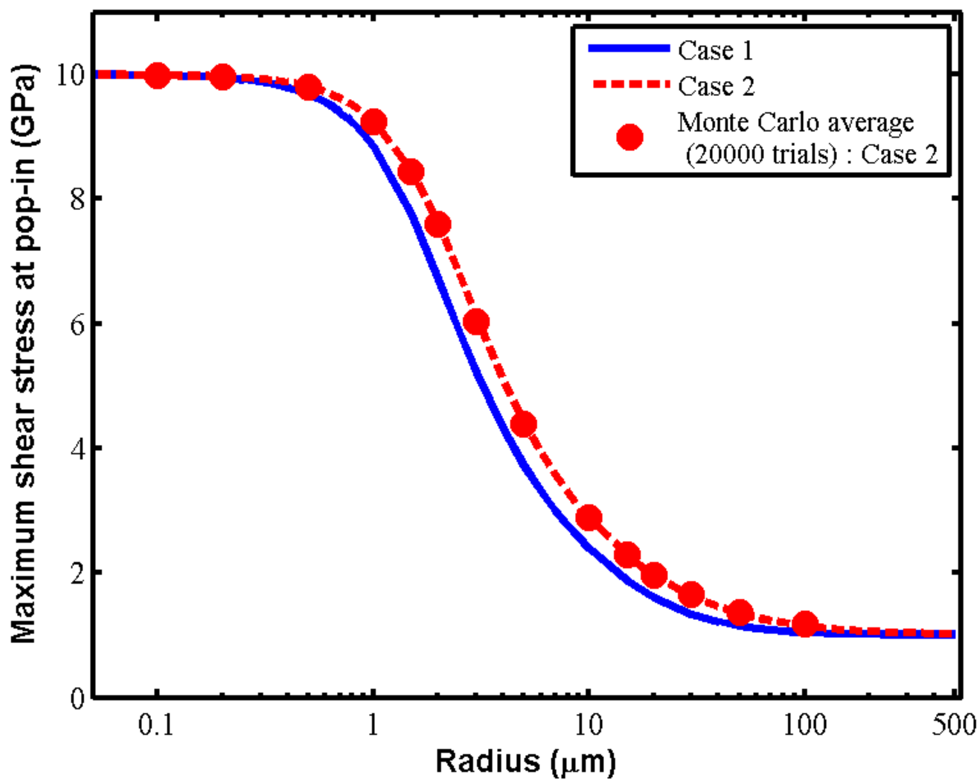

Figure 3.10. Comparison of model predictions for cases 1 & 2 and Monte Carlo results for case 2.

(a)

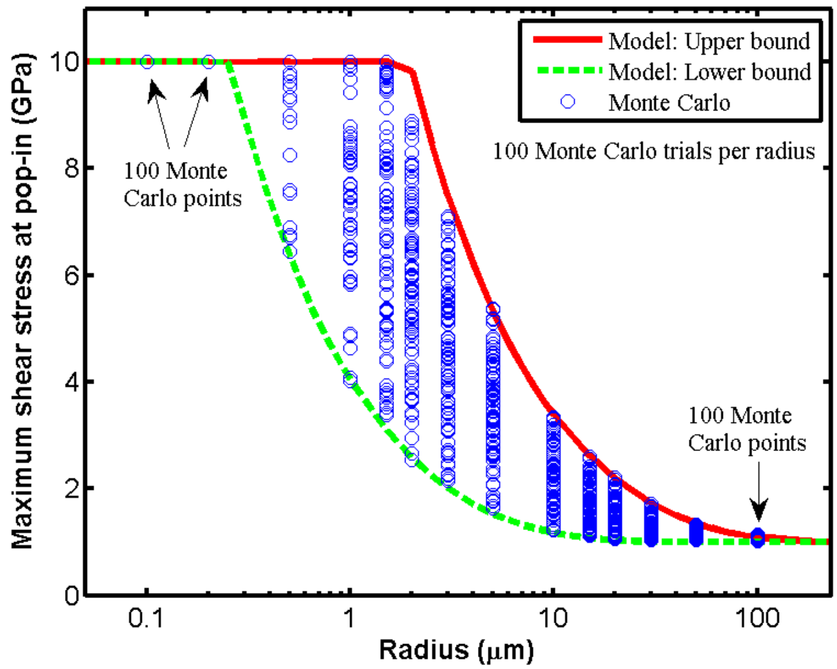

(b)

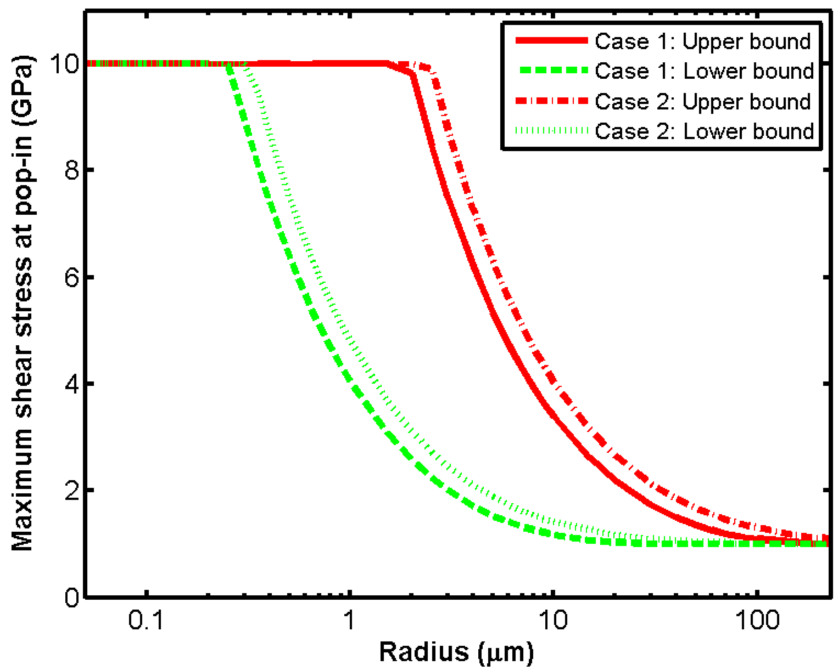

Figure 3.11. (a) Comparison of the model predictions for 90% scatter bounds with Monte Carlo results for the maximum shear stress at pop-in in case 1, and (2) comparison of the model predictions for 90% scatter bounds for case 1 and case 2.

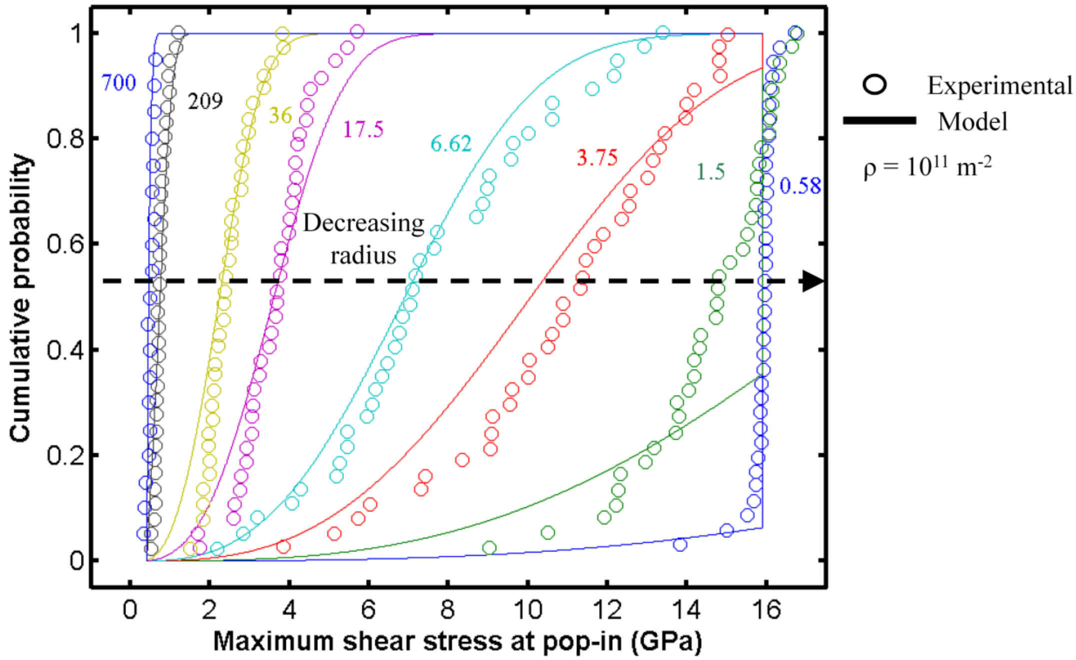

Figure 3.12. Comparison of experimental data (open circles) for the cumulative probability of maximum shear stress at pop-in in Mo (Morris *et al.*, 2011) with model predictions for case 1 (solid lines). The indenter radius (in μm) is shown beside the corresponding curve.

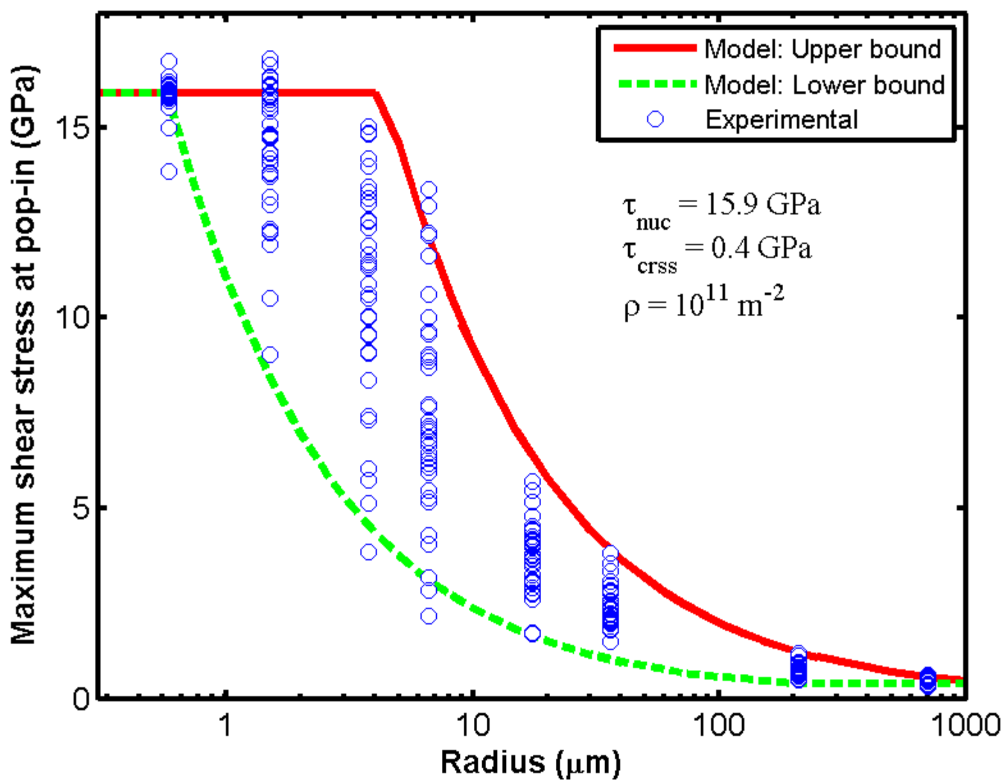

Figure 3.13. Comparison of experimental data for the maximum shear stress at pop-in in single crystal Mo (Morris *et al.*, 2011) with model predictions for 90% scatter bounds.

SUMMARY AND CONCLUSIONS

A simple weak link statistical model has been developed to explain recent experimental results of the strength of small specimens containing a limited number of dislocations. The framework developed in the model has been applied to micro-pillar compression / tension and indentation pop-in using dislocation densities measured by TEM or micro-focus x-ray techniques. The model predictions match the experimental results, giving credence to the notion that "smaller is stronger" from a purely statistical point of view.

Micro-pillar compression testing on single crystal Mo-alloy fibers by Bei et al. (Bei *et al.*, 2008) reported that as-grown pillars exhibit theoretical strengths (~9.2 GPa) in compression. In contrast, when the Mo-alloy fibers are pre-strained in the matrix, before the Mo-alloy pillars were exposed and compressed, which presumably introduces dislocations, dramatically lower strengths were observed. In addition, there appeared to be a transition from stochastic to deterministic behavior with increasing pre-strain for a given pillar size. In order to provide microstructural insights to reconcile the experimental results, an aberration corrected STEM has been used to investigate the defect structures of as-grown and pre-strained single-crystal Mo-alloy fibers. At one extreme, the as-grown fibers were practically defect-free and hence exhibited yield strengths close to the theoretical strength during micro-pillar compression testing. At the other extreme, the 16% pre-strained fibers showed high dislocation densities without any significant inhomogeneities, resulting in bulk-like, deterministic behavior. At an intermediate pre-strain (4%), the fibers exhibited inhomogeneous dislocation distributions resulting in stochastic behavior.

Subsequently, Johanns et al. reported results of in-situ micro-tensile tests on 10-30 µm long Mo-alloy fibers. A large scatter in yield strength of as-grown fibers was observed with strengths ranging all the way from the theoretical strength of ~9.2 GPa to the bulk strength of ~1 GPa. This was in contrast to the micro-pillar compression tests on ~1 µm long specimens of the same material (Bei *et al.*, 2008), where specimens yielded deterministically at the theoretical strength of ~9.2 GPa. This apparent discrepancy, points towards the interrelationship between specimen size, strength and scatter in strength and forms the basis for developing a stochastic model.

The current weak link model explores how statistics can be used to provide a framework to model the yield strength of small specimens containing limited number of dislocations, based on the initial dislocation structure. The model neglects interactions between dislocations and any thermal effects in dislocation nucleation. The dislocation distribution in the specimen is considered to be comprised of two types of randomness, viz., randomness in the spatial distribution of dislocations and randomness in the strength of the dislocations, i.e., stress needed to activate them. While the randomness in the spatial distributions of dislocations is modeled using a Poisson distribution, the randomness in the stress needed to activate the dislocations is modeled by assigning a random Schmid factor to the dislocations. Monte Carlo simulations were carried out not only to validate the analytical model but also to help visualize the results of a limited number of tests. The model not only predicts the yield strength in the presence of dislocations but also in their absence in a closed form. The average yield strength for a given dislocation density transitions from a higher strength level (theoretical strength) to a lower strength level (bulk strength), exponentially with specimen size. In addition to predicting the average yield strength, the scatter in yield strength is also predicted in closed form. The scatter in the yield strength is high at intermediate specimen sizes, while it is minimal at small and large specimen sizes. Thus, with increasing specimen size the yield strength transitions from a higher strength level to a lower strength level with significant scatter in the intermediate regime. Applying the model using the dislocation densities and arrangements measured by TEM, we can explain the discrepancy in the average yield strength and scatter in yield strength between micro-compression and micro-tensile tests of as-grown Mo-alloy fibers, wherein 1 μm long pillars in compression show high strengths (~ 9.2 GPa) without much scatter while the same fibers having 10-30 μm length show significant scatter in strength (1 - 9.2 GPa) in tension. The model also correctly predicts the average strength and scatter in strength of the pre-strained Mo-alloy fibers using the corresponding dislocation densities measured by TEM.

Similarly, the scatter in yield strength of metallic whiskers during tensile testing (Brenner, 1956) can also be qualitatively explained by assuming a reasonable dislocation density.

After explaining the experimental results of uniaxial compression/tension, the modeling framework was extended to the more complex case of indentation pop-in. Recent experimental results of spherical indentation on single crystal molybdenum (Morris *et al.*, 2011) have shown a “size effect” in that the maximum shear stress at pop-in transitions with increasing indenter radius from a high strength level corresponding to the theoretical strength of the material to a lower strength level corresponding to the bulk strength. Also, significant scatter in the shear stress is observed at intermediate radii. This behavior is analogous to the yield strength of Mo-alloy fibers under compression / tension except for the fact the length scale associated with the size effect is the indenter radius instead of fiber size. Hence, the stochastic model developed for uniaxial compression / tension has been extended to spherical indentation where the stress state is more complex. The model predicts the pop-in loads and maximum shear stress at pop-in as a function of indenter radius. The model considers pop-in not only due to nucleation of dislocations but also due to activation of pre-existing ones. The model predicts a transition in the maximum shear stress at pop-in from a higher strength level (τ_{nuc}) to a lower strength level (τ_{crss}) with increasing indenter radius, which is one of the length scales associated with size effect in spherical indentation. In addition, the model precisely captures the scatter in the maximum shear stress at pop-in observed in the experimental results on single crystal Mo using the dislocation densities estimated by micro-focus x-ray techniques. All these small scale tests (micro-compression / tension and spherical indentation pop-in) clearly point towards the fact that the statistics of defects play a vital role in determining the mechanical behavior of materials at small length scales.

VITA

Sudharshan Phani was born in Hyderabad, India in 1982. He obtained his Bachelor's degree in Mechanical Engineering from the Indian Institute of Technology, Madras in 2003. He was a scientist at the International Advanced Research Center for Powder Metallurgy and New Materials (ARCI), Hyderabad from 2004 to 2008. He started working on his PhD at the University of Tennessee from the Fall of 2008 under the guidance of Prof. George Pharr.